The Structural and Mechanical Properties of the Pt-Ti and Ir-Ti Systems

by

Miguel Cavero

Submitted in partial fulfilment of the academic requirements
for the degree of Doctor of Philosophy in the
School of Physics,
University of KwaZulu-Natal
Pietermaritzburg

August 2011

As the candidate's supervisor I have/have not approved this thesis for submission.

Signed: ..... Name: ..... Date: .....

Abstract

Ab initio plane wave based density functional calculations within the generalised gradient approximation (GGA) have been carried out on a wide range of phases and stoichiometries for the platinum-titanium (Pt-Ti) and iridium-titanium (Ir-Ti) alloy systems, using the Vienna Ab Initio Simulation Package (VASP) with projector augmented wave (PAW) potentials.

For all of the phases in this work, the equilibrium structures were found by performing a full relaxation of the atoms. There were 20 different phases considered for varying atomic percentage compositions for each alloy system. Energy-volume calculations and heats of formations were used to determined the equilibrium structures at each atomice percentage composition and to determine if there were high temperature phases at that composition. The elastic constants and elastic moduli are calculated and the electronic structure and density of states (DOS) were considered to understand the hardness and stability properties of the alloys.

For the Pt-Ti system, the low and high temperature phases at different compositions agreed with previously published results in the literature. Intermediate phases at 50% were also determined, in agreement with previous results. Alloying Pt with Ti resulted in a decrease in the bulk modulus, i.e. not adding strength to the metal. However, the shear modulus increased for most of the alloys compared to bulk Pt and it was found that in general, alloying may increase the resistance to shear. PtTi alloys were found to be ductile in nature, as with both constituent metals in their bulk form.

In the Ir-Ti system, bulk Ir was found to have the highest bulk, shear and Young's modulus with each of these values decreasing with increasing percentage Ti in the alloy. IrTi

alloys with 66.7% Ir composition or higher were found to be brittle in nature, similar in behaviour to bulk Ir; alloys with a higher percentage concentration of Ti were found to be ductile.

DECLARATION

I ..... declare that

(i) The research reported in this thesis, except where otherwise indicated, is my original work.

(ii) This thesis has not been submitted for any degree or examination at any other university.

(iii) This thesis does not contain other persons' data, pictures, graphs or other information, unless specifically acknowledged as being sourced from other persons.

(iv) This thesis does not contain other persons' writing, unless specifically acknowledged as being sourced from other researchers. Where other written sources have been quoted, then:

  (a) their words have been re-written but the general information attributed to them has been referenced;

  (b) where their exact words have been used, their writing has been placed inside quotation marks, and referenced.

(v) Where I have reproduced a publication of which I am an author, co-author or editor, I have indicated in detail which part of the publications was actually written by myself alone and have fully referenced such publications.

(vi) This thesis does not contain text, graphics or tables copied and pasted from the internet, unless specifically acknowledged, and the source being detailed in the thesis and in the References sections.

Signed: .....

Acknowledgements

I would like to thank Professor Nithaya Chetty for all of his support and assistance throughout this long road. I am so grateful to him for sticking by me during some very difficult times and for believing in me when I didn't believe in myself. I would also like to thank Dr Robert Lindebaum for his support and guidance, as well as his encouragement at every step of the way. I would like to thank Dr John Pierrus as well, for stepping in for the final admin side of things.

I am extremely grateful to Professor John Lowther for use of the VASO code at Wits University and for his assistance, as well as the Centre of Excellence in Strong Materials for their financial support.

To my friends and family, I would like to thank them for their prayers and support. This is a journey that I haven't walked on my own and I am thankful for those who have accompanied during testing times.

I would like to give a special thanks to my wife and best friend, Belinda. You have always been and always will be with me, and I dedicate this work to you and to our delightful Arwen.

Finally, but certainly not least, to my Lord and Saviour Jesus Christ, who gave me the opportunity and strength and ability and grace. It is He who makes me more than a conqueror and it is He who gives me victory over my most formidable opponents. Thank You, Lord!

Contents

List of Tables

List of Figures

Chapter 1

Introduction and Survey of Hard Materials

The aim of this thesis is to investigate and discuss the mechanical properties of the platinum-titanium (Pt-Ti) and iridium-titanium (Ir-Ti) alloy systems, by performing *ab initio* density functional calculations on a wide range of phases and stoichiometries within each system and to compute properties related to hardness and stability. Beginning with a discussion on hard materials and their applications, the Pt-Ti and Ir-Ti systems will be introduced.

Superhard materials have a wide range of applications from sharp cutting and grinding tools [1, 2], as body armour, in nuclear reactors [3] and also in the medical industry [4]. Apart from industrial applications, superhard materials are also of scientific interest since hardness itself is not properly understood or defined explicitly [5, 6]. There are different scales of measuring hardness and different values that relate to different aspects of deformation of a material.

In this study the focus was on the elastic constants and elastic moduli for various structures in these two binary alloy systems, where the energetics and electronic structure were considered in an attempt to understand the strength and stabilities of each structure.

1.1 Hardness

Hardness was first defined by looking at how one mineral was able to scratch another [7], and minerals were ordered with a higher hardness value meaning the mineral would scratch another with a lower value [8]. Numerical values for hardness can now be obtained by measuring the indentation on a material by a diamond indentor under a known load. Different methods to measure hardness give rise to different hardness numbers, such as Knoop and Vickers [7, 8]. Vickers hardness, for example, is related to yield stress. A material is deemed 'superhard' if it has a Vickers hardness that is greater than 40 GPa [1]. Carbon in the diamond structure and cubic boron nitride (c-BN) have the highest Vickers hardness values (70 GPa - 100 GPa for diamond and about 48 GPa for c-BN, see Table 1.1).

However, the hardness of a material is not simply given by only one numerical value. A material must satisfy certain conditions to be considered hard. These are the resistance to different types of deformation. A high resistance to volume compression or to linear compression means a material is difficult to compress elastically [5] and so it is called stiff. Materials with these high resistances have a large bulk modulus and/or Young's modulus. The bulk modulus is the inverse of the compressibility. A material that can withstand elastic deformation in a direction different to that of the stress will have a high shear modulus [1, 5]. For a material to be hard, it must also resist plastic deformation. This involves the irreversible motion of atoms with respect to one another in a lattice. Covalent bonding provides resistance to both elastic and plastic deformations. Diamond and c-BN are both covalent materials and have the highest bulk and shear moduli. Therefore, both the bulk and shear moduli are useful to understand and measure hardness. However, the shear modulus is believed to be more correlated to the hardness of a material than the bulk modulus [9]. Generally, a material that has a high shear modulus is considered hard [10].

For a bulk crystalline material, hardness depends on the elastic properties. A material with a high value of hardness generally has high values when it comes to elastic moduli and constants [11]. Both the bulk modulus B and the shear modulus G can be expressed in terms of the elastic constants. The elastic constants are a measure of the response of a crystal when an external strain is applied. They also give information about the bonding

characteristics for atomic planes adjacent to one another, as well as structural stability information [12]. For a given crystal structure, mechanical stability requires certain sets of conditions on the elastic constants. The exact details of these conditions are given in the next chapter.

In this thesis the elastic constants and moduli as an indication of the hardness of a material, are calculated for different phases of the Pt-Ti and Ir-Ti alloy systems to determine their mechanical properties and to determine their relative hardness compared with other transition-metal alloys.

1.2 Diamond and c-BN

Diamond is the hardest substance known to humans. Table 1.1 shows the Vickers hardness, bulk, shear and Young's moduli and Poisson ratio for diamond. The values for other hard materials is given as a comparison. There is much effort that has gone into developing materials that exceed its hardness properties [5]. To be able to develop new superhard materials, one must first understand what it is about diamond that gives it its hardness properties, as well as its other special properties such as high thermal conductivity and wear resistance [2].

Diamond is made up of tetrahedrally bonded atoms that form three dimensional fully covalent bonds [5, 28]. The bond lengths are also short, although the C-C bond length is not the shortest; C-O, C-N and B-O bond lengths are shorter though they occur in isolated molecules [7]. New superhard materials can then be composed of light elements that form short covalent bonds [5, 28, 7]. Alternatively, a different class of superhard materials has been proposed by combining light elements with heavy transition metals that have a high valence electron density [28, 29].

Cubic BN (c-BN) has a cubic structure (space group $F\bar{4}3m$) [30] similar to diamond, and is the second hardest material. However, it is expensive to use as it must be synthesized [5]. It does also have a low chemical reactivity as well as high thermal stability [29]. Together with diamond, c-BN can be synthesized under high pressure and temperature or by chemical vapour deposition (CVD) [1].

	H_V	B	G	E	ν
C (diamond)	70-100[a]	443[b]	535[c]	1050[d]	0.20[e]
c-BN	48[a]	400[f]	405[g]	847[h]	
SiC	29[c]	248[c]	*170-200*[i]	*400-470*[i]	
WC		329[j]	*295*[k]	*703*[k]	*0.194*[k]
SiO_2	33[c]	316[l]	220[l]		
TiO_2[m]		*348*	*203*	*525*	*0.293*
OsB_2		365-395[n]	*174*[o]	*444*[o]	*0.277*[o]
RuB_2[o]		*290*	*184*	*455*	*0.238*
Si_3N_4	30-35[p]	300-308[q]			

Table 1.1:
The Vickers hardness H_V, bulk modulus B, shear modulus G, Young's modulus E and the Poisson ratio ν of selected hard materials. All values are in GPa, except ν which is unitless. Values in italic are theoretical. [a]Reference [1], [b]Reference [13], [c]Reference [6], [d][14], [e]Reference [15], [f]Reference [16], [g]Reference [17], [h]Reference [18], [i]Reference [19], [j]Reference [20], [k]Reference [21], [l]Reference [22]. All values for TiO_2 are for the cotunnite structure, [m]Reference [23]. [n]Reference [24]. All theoretical values for OsB_2 and RuB_2 are for the orthorhombic structure, [o]Reference [25]. Values for Si_3N_4 are for the spinel structure, [p]Reference [26], [q]Reference [27].

BN has the second shortest bond length, the B-N bond at 1.57 Å is roughly 2% longer than the C-C bond in diamond [7]. c-BN shares several other physical properties with diamond, including phase diagrams and atomic sizes [31].

1.3 Carbides

Transition metal carbides are widely used industrially due to the desirable properties they possess, such as high melting points and good corrosion resistance as well as a certain amount of plasticity [20, 32]. WC has a high melting point and so is used in cemented carbides such as tungsten carbide cobalt (WC-Co). Apart from being a material with a high hardness value, WC-Co also has a high fracture toughness due to the contributions of the metal and carbide phases [33]. Co binds well with WC; the good densification leads to better mechanical properties. However, the high cost of Co means a cheaper alternative metal is needed [32]. The hexagonal phase of WC is semimetallic. Charge density plots show charge accumulation between nearest neighbour W and C site. The bonding

in transition metal carbides such as WC is similar to bonding in pure transition metals. The C atoms add stiffness to the lattice [20].

There is a large number of structures (as many as 75) identified for SiC [34]. Due to its chemical and physical properties, the wide band gap semiconductor SiC has applications in high temperature electronics [35]. SiC also has excellent refractory properties, and can be used at high temperatures for nuclear applications [36]. Si atoms form strong σ-bonds; when combined with C,B and N (e.g. in SiC and Si_3N_4) the bonds play a role in the formation of superhard materials [37]. Hard materials tend to be composed of atoms that are linked with short bonds [7]. The Si-C bond has a length of 1.88 Å, compared to 1.54 Å for the C-C bond length in diamond and 1.57 Å for the B-N bond in c-BN. It is known that compounds from third period elements, such as Si, combined with second period elements (B, C and N) are hard [38]; they form tetrahedral structures which are light, covalent structures.

1.4 Oxides

Oxides are readily available in nature as minerals. There are several different phases for various oxide minerals, including minerals such as SiO_2. One phase of SiO_2 is the stishovite phase which has been claimed to be the third hardest material [39]. Stishovite is a high-temperature phase which has a very dense packing of octahedra. There are more O atoms surrounding Si compared to the quartz phase, causing an increase in the bond length (1.61 Å for a typical Si-O bond) but also adding more bonds [7]. The smaller atomic volume and the formation of partial covalent bonds gives rise to the the increased hardness of stishovite: its Vickers hardness and bulk modulus is among the highest for hard material oxides.

TiO_2 exists in different phases (under various temperature and pressure conditions, for example, rutile, anatase, fluorite, pyrite and columbite [23]) which are thought to possess superhard properties comparable to diamond. TiO_2 has many industrial applications because of the properties it possesses: high refractive index, high dielectric constant and excellent optical transmittance. It is reported that ZrO_2 and HfO_2 have very high bulk moduli (444 GPa and 340 GPa respectively, [40]), therefore TiO_2 in the same structure

could potentially be very hard [6]. It is highly likely in the case of metal dioxides that the bulk modulus increases with the metal coordination [41]. The cotunnite structure has the highest coordination, whereby the metal is coordinated by nine O atoms. It is in this phase that ZrO_2, HfO_2 and TiO_2 have had the highest bulk modulus observed. The hardness of TiO_2 can be attributed to a high valence electron density which counteracts volume compression, short bond lengths of about 2 Å and also the high coordination which resists dislocation motion [23]. There is also a high covalency that contributes to the hardness of cotunnite TiO_2.

A new class of superhard materials are heavy element transition metal dioxides. RuO_2 (in the cubic fluorite-type $Pa\overline{3}$ structure) has been found to have a very high bulk modulus, even though the bond lengths between metal and O are longer than those which are thought to be essential for a large bulk modulus [42].

1.5 Borides

Another area of development of hard materials is combining light elements such as B with hard $5d$ metals, of which several have been synthesized [43]. OsB_2 has been found to have a low compressibility and to be hard, especially in the c-direction [3]. It has also been found that transition metal borides are harder than carbides and nitrides as well as less brittle [44]. Transition metal diborides have strong B-B and M-B bonds (where M is the metal) which resist either elastic or plastic deformations, resulting in a high shear modulus and strength [43]. It has also been proposed that by coupling B with transition metals that have high shear modulus values (such as Rh and Ir) the resulting borides would also exhibit high hardness. The results have been inconclusive, though [45]. OsB_2 has been shown to be metallic. This is rare among hard materials [24].

The elastic constants and moduli for both OsB_2 and RuB_2 have been calculated to be high [25]. The shear modulus suggests more pronounced directional bonding between the metals and the B atoms. The result of this bonding is a low Poisson's ratio. These directional bonds form a barrier to the nucleation and motion of dislocations, thereby increasing the shear strength and the hardness.

1.6 Advanced Nitrides

A group of materials that is becoming increasingly popular for refractory applications is the advanced nitrides group [46]. Recently silicon nitride in the high pressure cubic spinel phase was synthesized. Another high pressure phase is the cubic Th_3P_4 structure [39]. Spinel nitrides such as γ-Si_3N_4 combines hardness and a high thermal stability while c-Zr_3N_4 has good wear resistance. Si_3N_4 has excellent mechanical properties at high temperatures making it useful in engines, whilst having a high dielectric constant and large electronic gap for use in microelectronic devices [47]. It was shown that a wide band gap for γ-Si_3N_4 could lead to applications similar to those of the semiconducter GaN. Zr_3N_4 is predicted to be an insulator with a small indirect band gap and could well be formed under high temperature and pressure conditions [48]. The short bond length in Zr_3N_4 and the strong bonds in the γ-Si_3N_4 allow both structures to be considered as strong materials [48, 27]. Combining elements such as Si and N results in compounds that have partial tetrahedral bonding, and these are light, covalent hard materials [38].

1.7 Transition Metal Alloys

Transition metals with large values for the bulk modulus have have been combined with light, covalently bonded atoms (e.g. B, C and N) [5]. This has been done in order to find materials that maintain both volume and shape. Transition metals can have high incompressibility, such as Ir [49] and hence be used in high-pressure applications. Due to other properties such as high melting point and strength at high temperature, Ir-based alloys have been studied to see if they are able to replace the state-of-the-art Ni-based superalloys [50]. Platinum group metals have wide industrial use because of their physical and chemical properties [51].

1.7.1 The Pt-Ti System

Platinum group metals have been the source of interest for some time for various industrial applications as well as for further scientific research. Alloys of platinum group metals such as Pt and Ir with transition metals such as Ti have been shown to be very stable [52] at high temperatures. Pt and Ir can be used in ultra-high temperature alloys as the base elements [53]. The aim is to use these alloys in airplane turbines and rocket engines ahead

of Ni-based superalloys since they will be able to operate at higher temperatures before the decrease of their strength due to the high temperatures. Pt-based alloys have high melting points and good thermal shock resistance, as well as having good electrical and thermal conductivity, which is ideal for aerospace applications [54]. They are also known to have exceptional environmental resistance [55], for example resistance to corrosion, oxidation or plasma erosion [56].

Together with their stabilities, transition metal alloys (metals on the left-hand side combined with right-hand side metals of the transition series, for example transition metals such as Ti, Zr and Hf and Ni, Pd and Pt respectively) are also known to be unreactive and have high heats of formation. These alloys also form a variety of ordered phases [57].

Various studies have been made on ordered phases of the Pt-Ti alloy system [58, 59, 60, 61, 62, 63, 64]. Most transition metal alloys have shown to have maximum heats of formation at, or very close to, 50%-50% concentration, since this allows the number of pairs of unlike atom neighbours to be maximized [59]. This causes binding to be enhanced. Pt (together with $3d$ and $4d$ metal) alloys have maximum heats that are skewed off the 50%-50% concentration as shown by Watson *et al* and Fernando *et al* [59, 60] (although this is not so pronounced in the work of Wolverton *et al* [62] using the linear muffin-tin orbitals (LMTO) [65] method).

There are more deviations from Vegard's law [66] for Pt-rich (as well as for Pd- and Ni-rich) alloys than for Pt-poor alloys. This skewing from the 50%-50% concentration is even more pronounced for these alloys than for alloys of their neighbours, namely Co, Rh and Ir. This may be due to filling of the d bands thereby moving them away from the Fermi level. In alloys of other transition metals, the Fermi level is found to be somewhere within the d bands [59].

As stated before, the skewing favouring Pt-rich alloys is due to band filling effects. This is shown in the density of states (DOS) plots for different Pt-Ti alloys [60]. It can be seen from the DOS and site DOS plots that the lower part (states below the Fermi level) are mainly due to contributions of the transition metal Pt and the upper part are due to

states from Ti, above the Fermi level (also in Chen *et al* [63] and Ye *et al* [64]). In both the pure metal and the alloy, the d states dominate the DOS for the different sites. This shows the valence electrons should partly be transferred from the Ti site to the Pt site [63].

The pure metal Pt has partially occupied d bands. In the case of Pt-Ti alloys (except for the Pt_8Ti phase), the Pt bands are completely occupied. Hybridization of Ti wavefunction character into the Pt subbands accounts for the band fillings [60]. The filling of the bands is, therefore, not just due to charge transfer (of Ti electrons into the empty Pt levels) but also because of a compensation reduction in the total Pt d count.

The mechanical stability of the Pt-Ti alloys can also be found by calculating the elastic moduli and elastic constants for the different phases. The bulk modulus for Pt has been measured experimentally and calculated using different methods. The bulk modulus for Pt has been found to be 276 - 278 GPa [67, 68]. The elastic constants C_{ij} are generally obtained by applying certain strains on the lattice and calculating the energy as a function of the strain imposed. In a cubic system there are three independent elastic constants C_{ij}, and their experimental values are as follows: $C_{11} = 347$ GPa, $C_{12} = 251$ GPa and $C_{44} = 76$ GPa [69].

For a crystal to be stable, the elastic constants are bound by certain restrictions. Mechanical stability requires the strain energy to be positive [13]. In the case of a cubic crystal, for example, the restrictions are [67]:

$$C_{11} > |C_{12}|, \quad C_{11} + 2C_{12} > 0 \quad \text{and} \quad C_{44} > 0.$$

The bulk modulus and the elastic constants will be calculated for all the Pt-Ti alloy phases and compared to available experimental and theoretical values and used to determine stability and strength for each phase.

The bulk modulus is also related to the elastic constants, for example for a cubic system, by $B = (C_{11} + 2C_{12})/3$ [13]. The elastic constants can also be used to calculate the elastic moduli - that is, the shear modulus G, the Young's modulus E and the Poisson ratio ν - using a set of relations as follows:

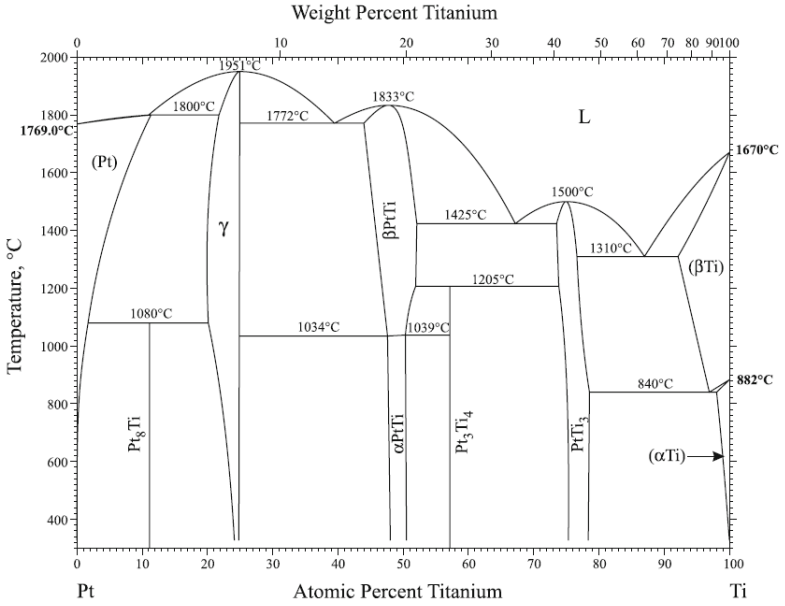

Figure 1.1:
The phase diagram for the Pt-Ti alloy system [70].

$$
\begin{aligned}
G &= \frac{3C_{44} + C_{11} - C_{12}}{5}, \\
E &= \frac{9BG}{3B + G}, \\
\nu &= \frac{1}{2}\left(1 - \frac{E}{3B}\right).
\end{aligned}
$$

This is the case for a cubic system [50]. The values of the elastic moduli will be compared with those of other known hard materials to determine whether they can be classified as such or not.

The phase diagram for the Pt-Ti system is shown in Figure 1.1. It shows the different phases that have been observed. Figure 1.1 also shows the low and high temperature phases at 50-50% composition. There are also low and high temperature phases for 25% to 50% Ti composition, corresponding to Pt_3Ti and Pt_2Ti considered in this study. In this study, the phases that were considered were those as given in References [58, 60, 71]. The structures are Pt_8Ti ($D1_a$-type tetragonal), Pt_3Ti (cubic $L1_2$, the Cu_3Au structure), Pt_5Ti_3 (a Ge_3Rh_5-type orthorhombic [72]), PtTi (both the low temperature $B19$ AuCd

and the high temperature $B2$ CsCl and also the $L1_0$ CuAu) and $PtTi_3$ ($A15$ cubic Cr_3Si). Other structures in consideration were Pt_2Ti in four different phases (one example is the $C11_b$ structure [59]) and $I4/m$ Pt_4Ti [73]. The Pt_5Ti ($W8$ Ga_2Zr) [62] structure was considered but the equilibrium was not found. Electronic structure calculations for Ti-rich phases of the alloy system in this study were restricted to Pt_4Ti_5, one phase of $PtTi_2$ ($MoSi_2$ $C11_b$) and $PtTi_3$. From Figure 1.1, it can be seen that there are low and high temperature phases for the 50% to 75% Ti composition region, including a Pt_3Ti_4 phase. These low and high temperature phases may be found from among the three structures used for Pt_2Ti (namely the $MoPt_2$, $ZrSi_2$ $C49$ and Co_2Si $C37$ structures) or the Pt_3Ti_4 structure, which was not considered in this work.

1.7.2 The Ir-Ti System

Naturally occuring Ir is found with Pt and other platinum group metals. Alloys of Ir that occur naturally are alloys in combination with Os (previously known as iridosmine and osmiridium [74]). It is the most resistant to corrosion of all the metals [75] but it is also difficult to process due to the very properties that make it useful [76].

The phase diagram for the Ir-Ti system is shown in Figure 1.2. The Ir-Ti alloy system is very similar to the Pt-Ti in that the same phases exist for the similar concentrations of the two elements [77]. This is mainly due to the fact that Ir lies next to Pt in the periodic table, and also has the face-centred cubic (FCC) structure as its equilibrium phase. The one notable difference is that the αIrTi phase, which is the equilibrium, low temperature structure at 50-50% composition is different for IrTi compared to PtTi. From Figure 1.2 it can be seen that there are also low and high temperature phases in the 25-43% and 60-75% Ti composition regions, as seen in the PtTi system.

The equilibrium lattice constant a_0 for Ir is 3.84 Å compared to 3.92 Å for Pt. The bulk modulus, however, is much higher for Ir than it is for Pt: 355 GPa compared to 278 GPa [69]. On the other side of the periodic table, Os, which crystallises in the hexagonal close-packed (HCP) structure, has been reported to have a lower compressibility than diamond [78]. Os and Ir are among the most dense elements, with a reported density of almost twice that of lead [8]. Theoretical studies of Os in FCC also report a high bulk

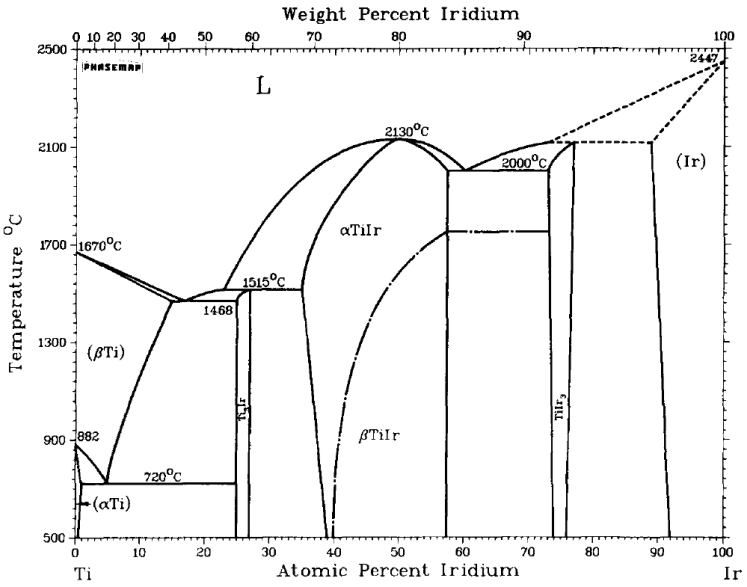

Figure 1.2:
The phase diagram for the Ir-Ti alloy system [70].

modulus of 419 GPa [13]. The elastic constants for Ir are also much higher than those of FCC Pt, except for C_{12} which is almost equal to that for Pt. The experimental values for the elastic constants for bulk Ir (and for Pt in parentheses) are: C_{11} = 590 (347) GPa, C_{12} = 249 (251) GPa and C_{44} = 262 (76) GPa [69]. Ir has comparable elastic constant values to the theoretical values of FCC Os [13]. Given these values, as well as the elastic moduli, Ir makes a good candidate as a base for the formation of hard metal alloys.

The comparison of the elastic moduli for FCC Ir with FCC Pt as well as diamond, is shown in Table 1.2. It can be seen that C in the diamond structure has elastic moduli far greater than the transition metals Pt and Ir. However, the Young's modulus of Ir is 59%-66% that of c-BN, which has a reported value between 800 and 900 GPa [79]. In comparison, the Young's modulus for Pt is only between 21%-24% of c-BN. Since it has a moderate value for the bulk modulus (which is a measure of its resistance to volume compression) as well as for the Young's modulus (which measures resistance to linear compression) bulk Ir can be considered as a stiff material [5]. It has a higher Young's modulus value than OsB_2 (410 GPa [43]) and SiC (418 GPa [80]).

	B (GPa)[a]	G (GPa)	E (GPa)	ν
C (diamond)	443	533[b]	1050[c]	0.20[e]
Pt (FCC)	278	63.7[d]	190[d]	0.396[f]
Ir (FCC)	355	221[d]	528[d]	0.26[g]
Os (FCC)[h]	419	259	644	0.25

Table 1.2:
The bulk modulus B, shear modulus G, Young's modulus E for diamond, FCC Pt and FCC Ir. The values of the bulk modulus are taken from [a]Reference [69]. The shear and Young's modulus for diamond is taken from [b]References [9] and [c][14] respectively. The shear and Young's modulus for both Pt and Ir are from [d]Reference [81]. The Poisson's ratio values are from [e]References [15], [f][51] and [g][75] respectively. The values for FCC Os are theoretical values from [h]Reference [13].

From the work of Chen *et al* [50], the calculated elastic constants were used to show the brittle nature of Ir and the Ir_3X compounds in the study. They showed that Ir_3Ti and Ir are brittle materials, with Ir being less brittle. The relative bond strengths were also compared, showing that pure FCC Ir has a larger bond strength than Ir_3Ti.

While the Pt-Ti system has been extensively investigated, the Ir-Ti system has not. To this end, all of the structures that have been considered for the Pt-Ti system will also be studied here.

1.8 Thesis Outline

The remainder of this thesis is outlined as follows. In the next chapter, density functional theory (DFT) will be introduced as the theoretical framework for the numerical calculations that have been carried out for this work. The VASP code, which was used to perform the calculations will be reviewed. Elastic theory which is the basis for the computations of the elastic constants and elastic moduli will also be presented in the next chapter. In Chapter 3, the results of the calculations for the various phases of the Pt-Ti alloy systems are presented: structure optimization to obtain the equilibrium lattice parameters, elastic constants and elastic moduli calculations and energy bands, DOS, site DOS and charge density calculations. The results for the corresponding Ir-Ti alloy systems are given in Chapter 4. The conclusions are given in Chapter 5.

Chapter 2

Background Theory

2.1 Hartree-Fock Approximation

Calculation of the electronic properties of a metal begins with the time-independent non-relativistic Schrodinger equation for a system of N electrons, $H\Psi = E\Psi$, where the Hamiltonian is given by

$$H = \sum_{i=1}^{N} \left(-\frac{\hbar^2}{2m}\nabla_i^2 - \sum_{\mathbf{R}} \frac{Ze^2}{|\mathbf{r}_i - \mathbf{R}|} \right) - \sum_{\mathbf{R}} \frac{\hbar^2}{2M_{\mathbf{R}}}\nabla^2 + \frac{1}{2}\sum_{\mathbf{R}\neq\mathbf{R}'} \frac{ZZ'e^2}{|\mathbf{R} - \mathbf{R}'|} + \frac{1}{2}\sum_{i\neq j} \frac{1}{|\mathbf{r}_i - \mathbf{r}_j|}. \tag{2.1}$$

Here, the first and third terms are the kinetic energy terms for the electrons and ions respectively. The second term represents the interaction between the electrons and the ions, the fourth term the ion-ion interaction and the last term is the interaction of the electrons with each other. The electronic coordinates are $\mathbf{r}_1, \mathbf{r}_2, ..., \mathbf{r}_N$ and the ionic coordinates are given by $\mathbf{R}$ and their masses are m and $M_{\mathbf{R}}$ respectively. The Hamiltonian can be simplified by a separation of the electronic and ionic coordinates. Since the mass of the ions is far greater than that of the electrons and since the forces that act on them are the same [82], the electrons will be in the ground state for any instantaneous configuration of the ionic coordinates since their velocities are much greater than that of the ions [83]. The electrons follow the ions adiabatically. They are then treated in a "frozen" nuclei configuration; the ionic kinetic energy is zero and the ion-ion interaction is treated as a constant.

As the Schrodinger equation cannot be solved exactly but for the simplest systems, for example the H atom, additional approximations need to be made. Hartree began by writing the ground state wavefunction in terms of one-electron orbitals which are orthonormal to

one another

$$\Psi(\mathbf{r}_1, \mathbf{r}_2, \ldots, \mathbf{r}_N) = \psi_1(\mathbf{r}_1)\psi_2(\mathbf{r}_2)\ldots\psi_N(\mathbf{r}_N), \tag{2.2}$$

where Ψ is a many-electron wavefunction which is a function of space and spin variables, which are both denoted by $\mathbf{r}_i$ for simplicity. By expressing the ground state wavefunction by Equation 2.2, a set of one-electron Schrodinger equations result having the form

$$-\frac{\hbar^2}{2m}\nabla^2\psi_i(\mathbf{r}) + V_{\text{ext}}(\mathbf{r})\psi_i(\mathbf{r}) + V_{\text{Hartree}}(\mathbf{r})\psi_i(\mathbf{r}) = \epsilon_i\psi_i(\mathbf{r}). \tag{2.3}$$

The first two terms are the kinetic energy and external potential, as given by the first two terms of Equation 2.1. The Hartree potential $V_{\text{Hartree}}(\mathbf{r})$ can be written as

$$V_{\text{Hartree}}(\mathbf{r}) = -e\int d\mathbf{r}'\frac{n(\mathbf{r}')}{|\mathbf{r}-\mathbf{r}'|}, \tag{2.4}$$

where $n(\mathbf{r})$ is the electronic charge density

$$n(\mathbf{r}) = -e\sum_{i=1}^{N}|\psi_i(\mathbf{r})|^2, \tag{2.5}$$

is a summation over the occupied electronic states. The Hartree potential (Equation 2.4) depends only on the time-averaged electronic distribution in the system. Although the Hartree approximation does provide some good results, there are drawbacks, for example not allowing antisymmetry of the wavefunction.

The Hartree-Fock approximation has been used to obtain solutions for the Schrodinger equation as well as being a platform for other methods. In the Hartree-Fock approximation the wavefunction is written as a Slater determinant [84] of one-electron wavefunctions

$$\Psi(\mathbf{r}_1, \mathbf{r}_2, \ldots, \mathbf{r}_N) = \begin{vmatrix} \psi_1(\mathbf{r}_1) & \psi_1(\mathbf{r}_2) & \ldots & \psi_1(\mathbf{r}_N) \\ \psi_2(\mathbf{r}_1) & \psi_2(\mathbf{r}_2) & \ldots & \psi_2(\mathbf{r}_N) \\ \vdots & \vdots & & \vdots \\ \psi_N(\mathbf{r}_1) & \psi_N(\mathbf{r}_2) & \ldots & \psi_N(\mathbf{r}_N) \end{vmatrix}. \tag{2.6}$$

The determinant is anti-symmetric when coordinates are exchanged, thereby being compatible with the Pauli exculsion principle. The expectation value of the Hamiltonian can be found by

$$\langle H\rangle_\Psi = \frac{(\Psi, H\Psi)}{(\Psi, \Psi)}, \tag{2.7}$$

where

$$(\psi, \phi) = \int d\mathbf{r}_1 \dots d\mathbf{r}_N \psi^*(\mathbf{r}_1, \dots, \mathbf{r}_N)\phi(\mathbf{r}_1, \dots, \mathbf{r}_N). \tag{2.8}$$

Using the Slater determinant (Equation 2.6) in Equation 2.7 gives rise to

$$\begin{aligned} \langle H \rangle_\Psi = & \sum_i \int d\mathbf{r}\ \psi_i^*(\mathbf{r}) \left(-\frac{\hbar^2}{2m}\nabla^2 + V_{\text{ext}}(\mathbf{r}) \right) \psi_i(\mathbf{r}) \\ & + \frac{1}{2}\sum_{i,j} \int d\mathbf{r} d\mathbf{r}' \frac{e^2}{|\mathbf{r} - \mathbf{r}'|} |\psi_i(\mathbf{r})|^2 |\psi_j(\mathbf{r})|^2 \\ & - \frac{1}{2}\sum_{i,j} \int d\mathbf{r} d\mathbf{r}' \frac{e^2}{|\mathbf{r} - \mathbf{r}'|} \delta_{s_i s_j} \psi_i^*(\mathbf{r}) \psi_i(\mathbf{r}') \psi_j^*(\mathbf{r}') \psi_j(\mathbf{r}), \end{aligned} \tag{2.9}$$

where the external potential $V_{\text{ext}}(\mathbf{r})$ is

$$V_{\text{ext}}(\mathbf{r}) = -\sum_{\mathbf{R}} \frac{Ze^2}{|\mathbf{r}_i - \mathbf{R}|}. \tag{2.10}$$

which leads to the Hartree-Fock equations by minimising this equation with respect to ψ_i^*:

$$-\frac{\hbar^2}{2m}\nabla^2\psi_i(\mathbf{r}) + V_{\text{ext}}(\mathbf{r})\psi_i(\mathbf{r}) + V_{\text{el}}(\mathbf{r})\psi_i(\mathbf{r}) - \sum_j \int d\mathbf{r}' \frac{e^2}{|\mathbf{r} - \mathbf{r}'|} \psi_j^*(\mathbf{r}')\psi_i(\mathbf{r}')\psi_j(\mathbf{r})\delta_{s_i s_j} = \epsilon_i \psi_i(\mathbf{r}). \tag{2.11}$$

The last term in the above equation is known as the exchange term. It is nonlinear is ψ_i and an integral operator, acting only between electrons of same spin. This exchange term represents the Pauli exclusion effect as well as the so called self-term which must be subtracted from the self term included in the Coulomb energy. This results in lowering the energy, as if each electron interacts with a positive "exchange hole" around it.

Although the Hartree-Fock approximation has been used extensively by chemists, it does not yield good results for the problem of the homogeneous electron gas. Properties of electrons near the Fermi level, as well as the density of states function are incorrect leading to an inadequate theory for metals.

2.2 Density Functional Theory

Density functional theory has its foundations in the work of Hohenberg and Kohn in 1964 [85]. It has helped to develop independent-particle methods that take into account the particles' correlations and interactions. Because of this, density functional theory is the

primary electronic structure calculation method for condensed matter physics [86].

Density functional theory was designed to be an exact theory for many-body systems. Hohenberg and Kohn presented two theorems in their work of 1964 [85]:
Theorem 1: Any many-electron system interacting in an external potential $V_{\text{ext}}(\mathbf{r})$ has a ground state charge density $n(\mathbf{r})$ that uniquely determines the external potential (to within a constant).
Theorem 2: The total energy of the system $E[n]$ can be defined as a functional of the density $n(\mathbf{r})$. For any given external potential $V_{\text{ext}}(\mathbf{r})$, the density that minimizes the functional gives rise to the exact ground state energy, and this density is the exact ground state density $n_0(\mathbf{r})$.

There are corollaries to each of the two theorems:
Corollary to Theorem 1: The ground state density $n_0(\mathbf{r})$ determines the Hamiltonian (save for a constant shift in energy) which in turn determines the many-body wavefunction. This results in all the system properties being determined completely from the ground state density.
Corollary to Theorem 2: The energy functional $E[n]$ sufficiently determines the ground state energy and density. Other methods need to be applied to obtain the excited states.

If the density $n(\mathbf{r})$ is specified, then all of the system properties can be defined as functionals of the density $n(\mathbf{r})$. The total energy functional can be written as

$$E_{\text{HK}} = T[n] + E_{\text{int}}[n] + \int d\mathbf{r}\ V_{\text{ext}}(\mathbf{r})n(\mathbf{r}) + E_{\text{II}}. \tag{2.12}$$

Here, E_{II} is the nuclei interaction energy, T and E_{int} are the electronic kinetic and interaction energies and $V_{\text{ext}}(\mathbf{r})$ is the external potential.

Despite these theorems and their proofs, there is no way of knowing what form the energy functional takes. In addition, the theory was not able to show how to obtain this functional.

To proceed, the Hohenberg-Kohn theory was extended with an *ansatz* by Kohn and Sham [87] in 1965 where the original many-electron problem is replaced by an independent-electron problem that can be solved. This resulted in a set of independent-electron equa-

tions similar to the Hartree-Fock equations.

Firstly, the exact ground state density $n_0(\mathbf{r})$ is made to be the same as the ground state density of the auxiliary non-interacting particle system:

$$n_0(\mathbf{r}) = \sum_{i=1}^{N} |\psi_i(\mathbf{r})|^2 . \tag{2.13}$$

From Hohenberg and Kohn the ground state energy is a functional of the density $E_0[n]$. The non-interacting kinetic energy has the usual form (in atomic units)

$$T_0 = -\frac{1}{2} \sum_{i=1}^{N} \left\langle \psi_i \left| \nabla^2 \right| \psi_i \right\rangle , \tag{2.14}$$

and the Hartree term as

$$E_{\text{Hartree}}[n] = \frac{1}{2} \int d\mathbf{r} d\mathbf{r}' \frac{n(\mathbf{r}) n(\mathbf{r}')}{|\mathbf{r} - \mathbf{r}'|}. \tag{2.15}$$

The Kohn-Sham ground state energy now replaces the Hohenberg Kohn ground state energy (Equation 2.12)

$$E_{\text{KS}} = T_0[n] + E_{\text{Hartree}}[n] + \int d\mathbf{r}\ V_{\text{ext}}(\mathbf{r}) n(\mathbf{r}) + E_{\text{II}} + E_{\text{XC}}, \tag{2.16}$$

where E_{XC} is the exchange-correlation energy. The kinetic energy T_0 is a functional of the orbitals $\psi_i(\mathbf{r})$ and $V_{\text{ext}}(\mathbf{r})$, $E_{\text{Hartree}}[n]$ and E_{II} are well defined. The exchange-correlation energy can be given by comparing the Hohenberg-Kohn (Equation 2.12) and Kohn-Sham (Equation 2.16) total energies

$$E_{\text{XC}}[n] = \langle T \rangle - T_0[n] + \langle V_{\text{int}} \rangle - E_{\text{Hartree}}[n]. \tag{2.17}$$

This shows that the exchange-correlation energy is the difference of the electronic kinetic and interaction energies of an interacting system and the independent-particle system [86].

The Kohn-Sham energy functional (Equation 2.16) is solved by minimizing it with respect to the orbital $\psi_i^*(\mathbf{r})$ and subject to the constraint of orthonormalization

$$\langle \psi_i | \psi_j \rangle = \delta_{i,j}, \tag{2.18}$$

which is required by the exclusion principle, and that total number of particles remians the same for any variation in the charge density

$$\int d\mathbf{r}\ \delta n(\mathbf{r}) = 0. \tag{2.19}$$

The chain rule is used to derive the equation

$$\frac{\delta E_{\mathrm{KS}}}{\delta \psi_i^*(\mathbf{r})} = \frac{\delta T_0}{\delta \psi_i^*(\mathbf{r})} + \left[\frac{\delta E_{\mathrm{ext}}}{\delta n(\mathbf{r})} + \frac{\delta E_{\mathrm{Hartree}}}{\delta n(\mathbf{r})} + \frac{\delta E_{\mathrm{XC}}}{\delta n(\mathbf{r})}\right] \frac{\delta n(\mathbf{r})}{\delta \psi_i^*(\mathbf{r})} - \epsilon_i = 0. \tag{2.20}$$

The Lagrange multiplier ϵ satisfies the requirement of Equation 2.19. Using atomic units, Equation 2.20 becomes

$$\left(-\frac{1}{2}\nabla^2 + \int d\mathbf{r}' \frac{n(\mathbf{r}')}{|\mathbf{r}-\mathbf{r}'|} + V_{\mathrm{ext}}(\mathbf{r}) + V_{\mathrm{XC}}(\mathbf{r}) - \epsilon_i\right) \psi_i(\mathbf{r}) = 0. \tag{2.21}$$

The result is the Kohn-Sham equations which is a set of single-particle Schrodinger-like equations

$$\left(H_{\mathrm{KS}} - \epsilon_i\right) \psi_i(\mathbf{r}) = 0, \tag{2.22}$$

where

$$H_{\mathrm{KS}} = -\frac{1}{2}\nabla^2 + V_{\mathrm{ext}}(\mathbf{r}) + V_{\mathrm{Hartree}}(\mathbf{r}) + V_{\mathrm{XC}}(\mathbf{r}), \tag{2.23}$$

and the external potential $V_{\mathrm{ext}}(\mathbf{r})$ is defined in Equation 2.10 and the Hartree and exchange-correlation potentials are given by

$$V_{\mathrm{Hartree}}(\mathbf{r}) = \int d\mathbf{r}' \frac{n(\mathbf{r}')}{|\mathbf{r}-\mathbf{r}'|},\ V_{\mathrm{XC}}(\mathbf{r}) = \frac{\delta E_{\mathrm{XC}}[n(\mathbf{r})]}{\delta n(\mathbf{r})}. \tag{2.24}$$

2.3 Exchange and Correlation

The Kohn-Sham equations (Equation 2.21,2.22,2.23) are single-particle equations that need to be solved self-consistently. The Kohn-Sham equations are independent of any approximations to the exchange-correlation energy functional $E_{\mathrm{XC}}[n]$, and would lead to the true ground state density were the exact exchange-correlation functional known.

In the local density approximation (LDA) the exchange-correlation energy at a point $\mathbf{r}$ is equal to that of a homogeneous electron gas with the same density. It assumes that the effects of exchange and correlation arise primarily from the immediate vicinity of $\mathbf{r}$ but do not depend strongly on the density variations around that point. The exchange-correlation functional is then given by

$$E_{\mathrm{XC}}^{\mathrm{LDA}}[n(\mathbf{r})] = \int \epsilon_{\mathrm{XC}}[n(\mathbf{r})] n(\mathbf{r}) d\mathbf{r}, \tag{2.25}$$

where ϵ_{XC} is the exchange-correlation energy per particle of a homogeneous electron gas with an electron density n at the point $\mathbf{r}$. The exchange-correlation energy ϵ_{XC} is given as

a sum of the exchange energy of the homogeneous electron gas and the correlation part. The former can be found analytically with Hartree-Fock, while the correlation part can be found with high accuracy using the Quantum Monte Carlo (QMC) method of Ceperley and Alder [88].

Despite its simplicity the LDA has proved very succesful. The sum-rule for the exchange-correlation hole is correct [89]. Also, the errors in the approximation of the exchange and energies energy get cancelled out. LDA does have some limitations, and these have led to the development of improved exchange-correlation functionals.

The generalised gradient approximation (GGA) involves a dependence of the exchange-correlation functional energy on the gradient of the charge density. The functional for the exchange-correlation term can then be defined as [90]

$$E_{\mathrm{XC}}^{\mathrm{GGA}}[n(\mathbf{r})] = \int \epsilon_{\mathrm{XC}}^{\mathrm{GGA}}[n(\mathbf{r}), \nabla n(\mathbf{r})] n(\mathbf{r}) d\mathbf{r}. \tag{2.26}$$

Some widely used forms of GGA exchange-correlation functionals are those by Becke [91], Perdew and Wang [92] and Perdew, Burke and Ernzerhof [93], which have proved very succesful.

2.4 Electronic Structure Methods

There are three main types of electronic structure methods, each with their own advantages, in their range of applications, and disadvantages [86]. In the localized atomic orbital methods the wavefunction is given as an expansion of energy-independent orbitals. The simple Slater and Koster approach [94] leads a good understanding of electronic states. Other more accurate methods that use local orbitals include the all-electron, full-potential scheme by Koepernik and Eschrig [95] (using a linear combination of overlapping orbitals which are nonorthogonal), as well as the self-consistent density functional method by Soler *et al* [96] that uses pseudopotentials, upon which the SIESTA code is based.

The second type of electronic structure scheme is the atomic sphere method. Basis functions describe the rapidly-varying parts of the wavefunction near the nucleus as radial functions times spherical harmonics in spherical regions around the nuclei. In 1937 Slater

[97] suggested an atomic potential that is spherically symmetric in spherical regions around the atoms and zero outside of these regions. The plane wave solution is augmented with the solutions to the atomic problem, and this is known as the augmented plane wave (APW) method. In the KKR method (by Korringa [98] and Kohn and Rostocker [99]), the problem is formulated within the muffin-tin approximation (MTA), using Green's functions. The wavefunction inside the sphere inscribed into the Wigner-Seitz cell is a linear combination of the atomic problem solutions, and subject to the appropriate boundary conditions. The potential outside of this sphere is not spherically symmetric [100]. Using the KKR method allows separation of the atomic structure and the scattering, and it has become the method most widely used for liquids, disordered systems and metallic/non-metallic impurity system calculations [86]. Linear methods use the augmented wavefunction and its energy derivative around a chosen reference energy to write the augmented method in terms of the familiar energy equation involving a Hamiltonian as well as an overlap matrix. In the linear APW (LAPW) method [101], inside the augmentation spheres there is a linear combination of the solution of the radial Schrodinger equation at a certain energy and the energy derivative of this solution evaluated at the same energy. A plane wave expansion is used in the interstitial region. The basis set in the LAPW method can be much smaller compared to using plane waves, and the calculation time can be as much as three times faster than plane waves (as it is determined mainly by the matrix diagonalisation) [102]. The linear muffin-tin orbitals (LMTO) method [101, 103] uses a linear combination of the wavefunction and energy derivative in a central sphere. This combination continues smoothly into the interstitial region where it then joins the energy derivative function smoothly in each adjacent sphere. This all-electron method is popular because it is very fast [100], due to a small number of basis needed to accurately describe a system.

The third type of electronic structure is the plane wave and grid methods, used to effectively represent smooth functions. With plane waves and Fourier transforms, the Bloch theorem can be derived simply. Pseudopotential calculations can be done with a reasonable number of plane waves. Plane waves have also been used in new *ab initio* methods [86] (for example, Car-Parinello [104] and iterative methods such as the Lanczos [105] and Davidson [106] methods as well as the "residual minimisation method by direct inversion in the iterative subspace" RMM-DIIS [107]).

2.5 Plane Waves

A plane wave basis set can lead to a simple formulation of the Kohn-Sham equations within density functional theory [108] and are particularly appropriate for periodic crystals [86]. An advantage of using a plane wave basis set is that it completely spans the Hilbert space. Another is that all space is covered equally, without bias to any region in particular. One disadvantage, though, is that regions of both high or very low electron density have the same coverage, causing inefficiency as the system size increases [109].

The problem of dealing with an extremely large number of electrons in a solid/crystal and the infinite basis set to expand each wavefunction is alleviated using the periodicity of a system and Bloch's theorem. The number of wavefunctions can be dramatically reduced to the order of the number of electrons in the crystal unit cell. Bloch's theorem states that the electronic wavefunctions in a periodic potential can be written as a product of a plane wave and a function that has the periodicity of the lattice [110]:

$$\psi_{\mathbf{k}}(\mathbf{r}) = e^{i\mathbf{k}\cdot\mathbf{r}} u_{\mathbf{k}}(\mathbf{r}). \tag{2.27}$$

The periodic term of the wavefunction can be expressed as an expansion of plane waves in terms of wave vectors that are the reciprocal lattice vectors of the crystal [82]:

$$u_{\mathbf{k}}(\mathbf{r}) = \sum_{\mathbf{G}} c_{\mathbf{k}}(\mathbf{G}) e^{i\mathbf{G}\cdot\mathbf{r}}, \tag{2.28}$$

where $\mathbf{G}$ (defined by $\mathbf{G}\cdot\mathbf{R} = 2\pi n$, $n = 1, 2, 3, \ldots$) is the reciprocal vector for the Bravais lattice given by $\mathbf{R}$. The electronic wavefunctions are therefore given as a sum of plane waves

$$\psi_{\mathbf{k}}(\mathbf{r}) = \sum_{\mathbf{G}} c_{\mathbf{k}}(\mathbf{G}) e^{i(\mathbf{k}+\mathbf{G})\cdot\mathbf{r}}. \tag{2.29}$$

Substituting Equation 2.28 into the Kohn-Sham equations (Equation 2.22) and then integrating over $\mathbf{r}$ leads to the Kohn-Sham equations in reciprocal space

$$\sum_{\mathbf{G}'} \left[\frac{1}{2}|\mathbf{k}+\mathbf{G}|^2 \delta_{\mathbf{G},\mathbf{G}'} + V_{\text{ext}}(\mathbf{G}-\mathbf{G}') + V_{\text{Hartree}}(\mathbf{G}-\mathbf{G}') + V_{\text{XC}}(\mathbf{G}-\mathbf{G}') \right] c_{\mathbf{k}}(\mathbf{G}') = \epsilon_{\mathbf{k}} c_{\mathbf{k}}(\mathbf{G}). \tag{2.30}$$

This reciprocal space representation of the Kohn-Sham equations is a matrix eigenvalue problem, which is solved by diagonalizing the Hamiltonian matrix. The kinetic energy terms are on the diagonal. The potentials are expressed in their Fourier components. The

higher Fourier components rapidly decay to zero for smooth potentials, so that the plane wave basis set may be given a finite size by a cut-off energy E_{CUT}. Ths cut-off energy determines the size of the matrix by

$$E_{\mathrm{CUT}} = \frac{1}{2} |\mathbf{k} + \mathbf{G}|^2 . \tag{2.31}$$

2.6 k-point Sampling

The Wigner-Seitz cell of the reciprocal lattice is known as the (first) Brillouin zone (BZ). To find quantities such as the density and energy, integration over the BZ is required. The integration needs to be accurate, over a discrete set of points in the BZ. Insulators need only a few points to be integrated when considering their filled bands. Metals, though, have bands that cross the Fermi level and for these the integration method must be chosen carefully. Symmetry is also used to decrease the number of calculations by using integrals over the irreducible BZ (IBZ) [86].

The BZ can be mapped by a set of **k**-points for a given set of boundary conditions in the bulk solid [111]. For an infinite number of electrons in a solid, there are an infinite number of **k**-points in the BZ. Using the Bloch theorem, though, the problem is reduced to a finite number of wavefunctions at an infinite number of **k**-points within the BZ. For **k**-points that are very close to each other, the wavefunctions are nearly identical so the electronic wavefunctions can be represented over a region of reciprocal space at a single **k**-point. The electronic states are then calculated at a finite number of **k**-points, and hence the electronic potential and the total energy of the solid. A denser set of **k**-points can be used to reduce errors in the total energy calculations.

The special **k**-point technique is well suited with the plane waves method, which makes the calculations simple but accurate. A discrete set of **k**-points are selected within the irreducible part of the BZ. The selected points are determined according to the shape of the reciprocal space cell. Some **k**-points are mapped onto others due to group symmetry operations of a crystal, reducing the number of calculations for related points. The **k**-points method by Monkhorst and Pack [112] uses symmetry properties when generating the special **k**-points set.

2.7 Pseudopotentials

The idea behind the concept of pseudopotentials is essentially replacing one problem with another, with the latter being simplified. The use of a plane wave basis set to describe electronic wavefunctions via Bloch's Theorem leads to a problem of high computational cost. The tightly bound core orbitals require a large number of plane waves and the rapid oscillations of valence electron wavefunctions in the core region also requires many plane waves. These oscillations arise from the fact that the core and valence electrons must be orthogonal, due to the Pauli exclusion principle. For plane waves that have short wavelengths to be included, the cut-off energy must be set to a high value. However, the orbitals that exhibit rapid oscillations only occur in a small space of the cell, wasting a large amount of computational time. The size of the plane wave basis set to perform an all-electron calculation would make the problem computationally expensive.

Hellmann [113] introduced the idea of replacing the chemically inert core electrons with a weaker potential where only the valence electrons are treated explicitly. This is due to most physical properties of solids being more dependent on the valence electrons than the core. The pseudopotential is a weaker potential acting on pseudo wavefunctions instead of the true valence wavefunctions, but constructed so as to reproduce the effects the valence electronic wavefunctions due to the core electrons [82]. Coupled with the method of plane waves, the pseudopotential approximation largely reduces the number of plane waves needed in a total energy calculation [114, 115].

Since the aim is the solve the Kohn-Sham Hamiltonian (Equation 2.23) the number of orbitals is reduced (having removed the core electrons) and hence less memory is used. The less oscillations near the core region means the cut-off energy can be lowered with the use of pseudopotentials. This results in decreased memory requirements whilst increasing computational speed.

The psuedopotential is constructed in such a way that the scattering properties for the pseudo wavefunctions are the same for the valence wavefunctions. There must be no radial nodes inside the core region for the pseudo wavefunctions and outside of the core region the pseudopotential and the total potential must be identical.

The first pseudopotentials were based on parameters obtained by fitting the pseudopotential with experimental data. In *ab initio* calculations the pseudopotentials are generated without the use of experimental parameters, but these need to adhere to certain requirements for accurate representation.

As mentioned previously the pseudo wavefunction should contain no radial nodes in the core region, thereby making the pseudo wavefunction smooth which allows for a sufficiently small plane wave basis set. The pseudo wavefunction and the valence wavefunction must be identical outside of the core region. This also holds for the pseudopotential and the original potential. Thirdly, the eigenvalues from a pseudopotential must be the same for an all-electron atomic calculation. The charge in the core region is the same for a pseudo and atomic wavefunction:

$$\int_0^{r_c} \Psi^{AE*}(\mathbf{r})\Psi^{AE}(\mathbf{r})d\mathbf{r} = \int_0^{r_c} \Psi^{PP*}(\mathbf{r})\Psi^{PP}(\mathbf{r})d\mathbf{r}, \tag{2.32}$$

where $\Psi^{AE}(\mathbf{r})$ and $\Psi^{PP}(\mathbf{r})$ are the all-electron and pseudo wavefunctions respectively. This property of the pseudopotential is called norm-conservation, ensuring the correct total charge inside the core region. Finally the first and second derivatives of the pseudo wavefunctions at the boundary of the core region must be the same as the real values at the boundary.

The basic form of a non-local pseudopotential acts on an orbital in the following way

$$V_{\mathrm{SL}} = \sum_{lm} |Y_{ml}\rangle \, V_l(r) \, \langle Y_{ml}| \,, \tag{2.33}$$

where V_l is the pseudopotential for angular momentum l and the Y_{ml} are the spherical harmonics. The pseudopotential operator V_{SL} is called semi-local because of its dependence on l being non-local but its radial dependence being local.

Kleinman and Bylander [116] showed that the angular momentum component of the pseudopotential can be written as the sum of a local (independent of l) and non-local components

$$V_l(r) = V_{\mathrm{LOCAL}}(r) + \delta V_l(r). \tag{2.34}$$

The potential V_l is equal to the local all-electron potential outside of the cut-off radius and tends to $-Z_{\mathrm{ION}}/r$ as $r \to 0$. The Coulomb long range effects are included in the local potential V_{LOCAL}. The semi-local operator can now be written as

$$V_{\mathrm{SL}} = V_{\mathrm{LOCAL}}(r) + \sum_{lm} |Y_{ml}\rangle \, \delta V_l(r) \, \langle Y_{ml}| \, . \tag{2.35}$$

The non-local component $V_l(r)$ can be approximated by a non-local δV_{NL} which has the form

$$\delta V_{\mathrm{NL}} = \frac{|\phi_{lm}\delta V_l\rangle \, \langle \delta V_l \phi_{lm}|}{\langle \phi_{lm} \, |\delta V_l| \, \phi_{lm}\rangle}, \tag{2.36}$$

where the ϕ_{lm} are pseudo orbitals. δV_{NL} is separable and non-local, and this form requires only products of the projector functions

$$\langle \psi_i \, |\delta V_{\mathrm{NL}}| \, \psi_j\rangle = \sum_{lm} \langle \psi_i \, |\phi_{lm}\delta V_l\rangle \, \frac{1}{\langle \phi_{lm} \, |\delta V_l| \, \phi_{lm}\rangle} \, \langle \phi_{lm}\delta V_l \, |\psi_i\rangle \, , \tag{2.37}$$

where $\langle \delta V_l \phi_{lm}|$ are the projectors. These products reduce computation, although "ghost states" may be introduced (when operating on different energy states) and so care must be taken [86].

There are some considerations when using pseudopotentials. Firstly the cut-off radius is often chosen to give results that are agreement with experimental or other theoretical reference results. However a pseudopotential can only be made more transferable by reducing the cut-off radius. Ultrasoft pseudopotentials are in general more transferable than norm-conserving ones. Other considerations are, for example, whether to include relativistic effects and which electrons should be core and valence.

2.8 Ultrasoft Pseudopotentials

When trying to solve the problem of a large number of plane waves to expand electronic wavefunctions, two methods were derived. The first is the augmented plane wave (APW) [97] which is constructed to match the original plane wave outside of some sphere of radius R. It is written as

$$\phi_{\mathbf{k}} = e^{i\mathbf{k}\cdot\mathbf{r}}, r > R. \tag{2.38}$$

The potential inside of the sphere (of radius R) is spherically symmetric. The augmented plane wave is made to exactly satisfy the Schrodinger equation inside the sphere and be

continuous with the original wave at R. However the gradient of the two parts of the APW are not continuous. In addition, the portion outside of the sphere will not satisfy the Schrodinger equation. This requires a superposition of APWs, and the expansion is then give by

$$\psi_{\mathbf{k}}(\mathbf{r}) = \sum_{\mathbf{G}} c_{\mathbf{G}} \phi_{\mathbf{k}+\mathbf{G}}. \tag{2.39}$$

The sum is over all reciprocal lattice vectors.

The second method is the orthogonalised plane wave (OPW) [117, 118]. Here the contributions of core states are added to a plane wave in order to mimic the original wavefunction as much as possible. The OPW is given by

$$\phi_{\mathbf{k}} = e^{i\mathbf{k}\cdot\mathbf{r}} + \sum_{c} b_c \phi^c_{\mathbf{k}}, \tag{2.40}$$

summing over the core levels given by the wavevector $\mathbf{k}$. The OPW must be orthogonal to the each core level, and this is used to determine the coefficients b_c

$$b_c = -\int \phi^{c*}_{\mathbf{k}} \psi_{\mathbf{k}} e^{i\mathbf{k}\cdot\mathbf{r}} d\mathbf{r}. \tag{2.41}$$

The wavefunction is then given as a series of OPWs. The energy values in the OPW method, however, are not as accurate as those of the APW method. The OPW method is important since it led to the development of modern psuedopotential methods as well as the projector augmented wave (PAW) method.

Pseudopotentials are generated to be as smooth as possible, whilst conserving accuracy. The norm-conserving pseudopotentials described previously are designed to be accurate but tend not to always be smooth [86]. Ultrasoft pseudopotentials were introduced to express the problem in terms of two functions: a smooth part and an auxiliary function that represents the rapidly varying core. This is similar to OPW method and the transformation by Phillips and Kleinman [119] and Antoncik [120]. Ultrasoft potentials by Vanderbilt [121] result from the condition of norm-conservation being relaxed. This leads to a non-local overlap operator S and a non-local potential of the form

$$V^{\mathrm{US}}_{\mathrm{NL}} = \sum_{s,s'} (B_{s,s'} + \epsilon_s Q_{s,s'}) \left|\beta_s\right\rangle \left\langle\beta_{s'}\right|, \tag{2.42}$$

where Q is the difference in the integrated charge of the all-electron and pseudo wavefunctions ($Q_{s,s'} = \langle \psi_s | \psi_{s'} \rangle - \langle \phi_s | \phi_{s'} \rangle$), β_s are projector functions and $B_{s,s'}$ are matrix elements given by

$$B_{s,s'} = \langle \phi_s | \chi_{s'} \rangle \,, \tag{2.43}$$

where the function χ_s is defined from the pseudo function ϕ_s and a local potential $V_{\mathrm{LOCAL}}(\mathbf{r})$ as

$$|\chi_s\rangle = \left(\epsilon_s - \left[-\frac{1}{2}\nabla^2 + V_{\mathrm{LOCAL}}(\mathbf{r})\right]\right)|\phi_s\rangle \,. \tag{2.44}$$

The smooth functions ϕ_s solutions to the generalised eigenvalue problem

$$[H - \epsilon_s S]\,\phi_s = 0. \tag{2.45}$$

Here, the overlap operator S is given by

$$S = 1 + \sum_{s,s'} Q_{s,s'} \,|\beta_s\rangle \,\langle \beta_s| \,, \tag{2.46}$$

and Equation 2.45 is subject to the orthonormality condition that

$$\langle \phi_s \,|S|\, \phi_{s'} \rangle = \delta_{s,s'}. \tag{2.47}$$

The advantage of ultrasoft pseudopotentials is in relaxing the norm-conserving condition. The resulting wavefunctions are smoother and this gives rise to lower cut-off energies. The smooth wavefunctions ϕ_s can be made independently, subject only to it matching the original wavefunction at the chosen cut-off radius. This allows for a larger cut-off radius while still maintaining the desired accuracy.

2.9 Projector Augmented Wave

Ultrasoft pseudopotentials make use of localized spherical functions together with a smooth wavefunction that are solutions of a generalised eigenvalue problem. In the projector augmented wave (PAW) method [122, 123], the approach is similar to the orthogonalized plane wave (OPW) scheme by having wavefunctions that have contributions of smooth functions and core functions. The PAW method, though, keeps the all-electron core functions and the smooth valence wavefunctions. The localized contribution, integrated over a augmentation sphere is similar to the augmented plane wave (APW) method.

The first step is to find a linear transformation that relates the smooth pseudo wavefunctions $\phi(\mathbf{r})$ and the all-electron wavefunctions $\psi(\mathbf{r})$ such that

$$|\psi\rangle = T\,|\phi\rangle\,, \tag{2.48}$$

where the operator T is defined by

$$T = 1 + \sum_m \{|\psi_m\rangle - |\phi_m\rangle\}\,\langle p_m|\,, \tag{2.49}$$

where each smooth wavefunction is expanded in partial waves m inside each sphere. The p_m are projection operators which are localized inside the (augmentation) spheres ($p_m(\mathbf{r}) = 0, r > R_a$, where R_a is the radius of the augmentation sphere) and are orthogonal to the pseudo wavefunctions

$$\langle p_m\,|\phi_{m'}\rangle\, = \delta_{m,m'}. \tag{2.50}$$

The all-electron and pseudo wavefunctions are equal outside of the augmentation spheres

$$\psi_m(\mathbf{r}) = \phi_m(\mathbf{r}), r > R_a. \tag{2.51}$$

Now, any operator can be transformed to operate on the smooth part of the wavefunctions

$$A = \sum_i f_i\,\langle\psi_i\,|A|\,\psi_i\rangle = \sum_i f_i\,\left\langle\phi_i\left|T^+AT\right|\,\phi_i\right\rangle. \tag{2.52}$$

The summation is over the occupations f_i. The density, as well as other physical quantities of the system, can be given by the transformation operator T (Equation 2.49) and the above equation (Equation 2.52)

$$n(\mathbf{r}) = \tilde{n}(\mathbf{r}) + n^1(\mathbf{r}) - \tilde{n}^1(\mathbf{r}), \tag{2.53}$$

where

$$\tilde{n}(\mathbf{r}) = \sum_i f_i\,|\phi_i(\mathbf{r})|^2\,, \tag{2.54}$$

is the smooth part that can be evaluated on a plane wave grid, and

$$n^1(\mathbf{r}) = \sum_i f_i \sum_{m,m'} \langle\phi_i\,|\phi_m\rangle\;\psi_m^*(\mathbf{r})\psi_{m'}(\mathbf{r})\,\langle\phi_{m'}\,|\phi_i\rangle\;, \tag{2.55}$$

$$\tilde{n}^1(\mathbf{r}) = \sum_i f_i \sum_{m,m'} \langle\phi_i\,|\phi_m\rangle\;\phi_m^*(\mathbf{r})\phi_{m'}(\mathbf{r})\,\langle\phi_{m'}\,|\phi_i\rangle\;, \tag{2.56}$$

are contributions localized around each atom. These can be evaluated on a radial grid.

The total energy can also be written in the same manner as the density

$$E_{\mathrm{TOTAL}} = \tilde{E}_{\mathrm{TOTAL}} + E^1_{\mathrm{TOTAL}} + \tilde{E}^1_{\mathrm{TOTAL}}, \tag{2.57}$$

where $\tilde{E}$ is the smooth functions' energy contribution, E^1 is the energy term of the functions evaluated inside the spheres and $\tilde{E}^1$ is the energy in the spheres given by the full wavefunctions. Calculating total energies using ultrasoft pseudopotentials and PAW is very similar, the main difference being the choice of auxiliary functions. Forces and stresses are also similar, so that they can be calculated easily as with pseudopotentials.

Thus the PAW method maintains the advantages of all-electron and pseudopotential methods. There is access to the "true" wavefunction and hence the density, and so there are no problems with transferability. The size of the plane wave basis set is similar to ultrasoft pseudopotentials which makes PAW efficient as well as accurate.

2.10 VASP Simulation Code

The total energy calculations for this work were done using the Vienna *ab initio* Simulation Package (VASP) code [124, 125], written by George Kresse and Jurgen Furthmüller. The VASP code makes use of efficient iterative diagonalisation schemes for a fast evaluation of the Kohn-Sham functional. The efficient Broyden/Pulay mixing [107, 126] is used for the charge density mixing. Electron-ion interaction is described using ultra-soft Vanderbilt pseudopotentials [121] and more recently the PAW method [122, 123]. The VASP-PAW code has been shown to give lattice constants and bulk moduli results which are in excellent agreement with all-electron full-potential linearised augmented plane wave plus local orbital (FP-LAPW + lo) calculations, in the WIEN2k code [127], for a wide range of materials [128].

The code essentially consists of two main loops. An outer loop optimises the charge density, while the wavefunctions are optimised inside the inner loop [129]. Figure 2.1 shows the VASP flowchart for the self-consistent calculation of the Kohn-Sham ground state energy.

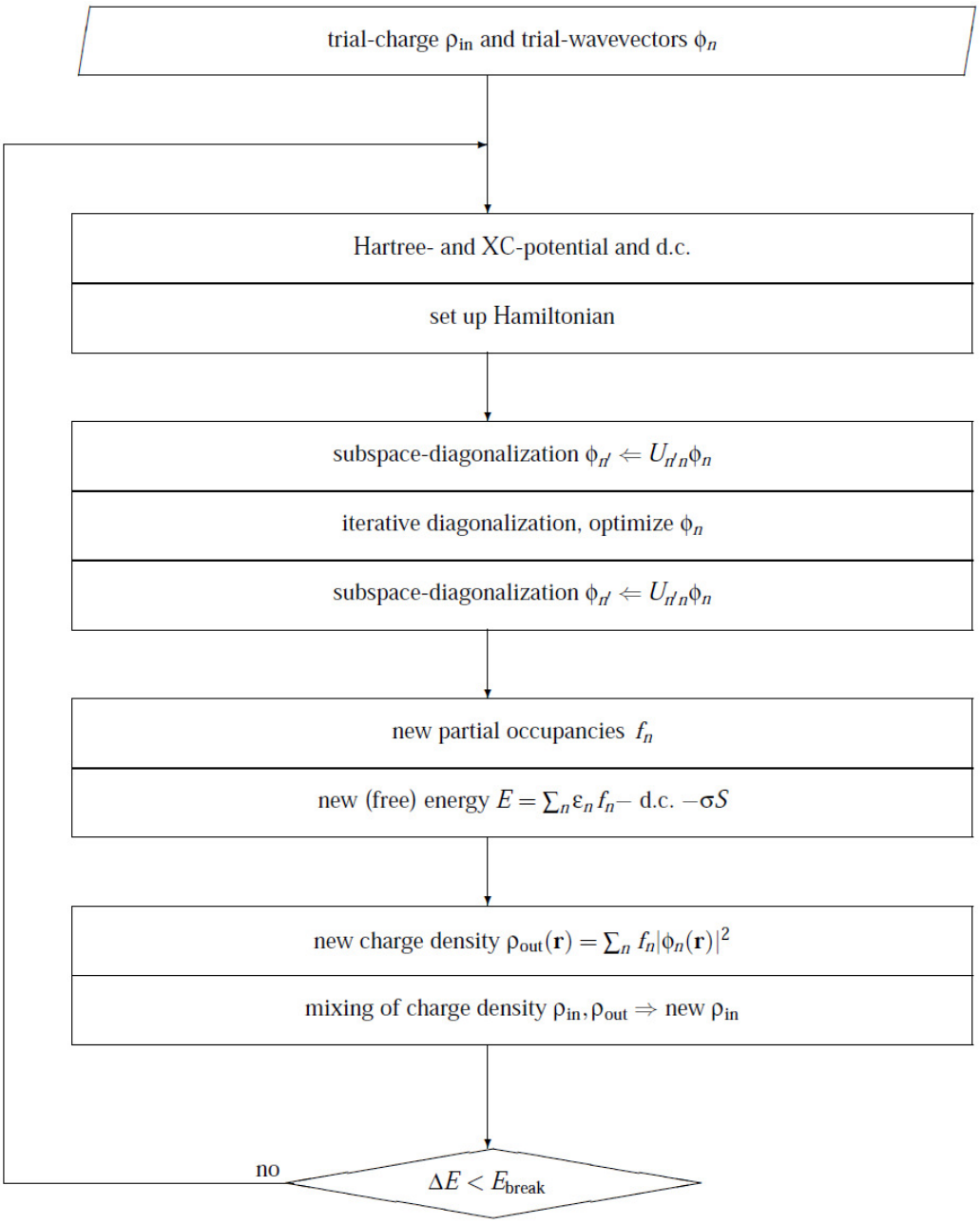

Figure 2.1:
A flowchart to show the self-consistent calculation of the Kohn-Sham groundstate in VASP.

An input charge density is used to set up the initial Hamiltonian. The wavefunctions are then diagonalised iteratively using a combination of the conjugate-gradient (CG) [130, 131] with block-Davidson [132] scheme and the RMM-DIIS scheme. The exact Kohn-Sham

eigenfunctions are not recalculated but only a linear combination of the lowest eigenfunctions (specified by the number of bands in the calculation). The Hamiltonian, therefore, needs to be diagonalised in the subspace spanned by the trial wavefunctions and the wavefunctions then transformed accordingly (for the Hamiltonian to be diagonal in the subspace spanned by the transformed wavefunctions). This is known as the subspace diagonalisation, which can be done either before or after the CG or residual minimisation scheme [129].

The new (free) energy is then calculated using different partial occupancies methods. Partial occupancies reduce the number of **k**-points needed to accurately calculate band-structure energies [129]. Linear tetrahedron methods interpolate bands within BZ cells. Smearing methods involve a convolution between each energy eigenvalue and a smearing distribution, enhancing convergence properties [133]. The linear tetrahedron method [134, 135] is simple for the VASP user. However, forces calculated when using the linear tetrahedron method may be inaccurate [129]. Fermi [136] or Gaussian [137, 138] smearing methods are used in solid state calculations. Since the total energy is not minimal in a smearing method, the generalised free energy replaces the total energy. This energy can be thought of the free energy of the electrons at a finite temperature (using a temperature parameter). Using an extrapolation, the zero-temperature energy (as the temperature parameter goes to zero) can be obtained from the finite-temperature calculation. The forces are derivatives of the free energy. The method by Methfessel and Paxton [138] improves the smearing methods, since these require careful choice of the temperature parameter, as well as being unable to use the calculated forces to obtain the equilibrium groundstate.

After the free energy is calculated, a new charge density is calculated from the optimised wavefunctions (from the subspace diagonalisation) and the partial occupancies. This charge density is mixed with the (old) input charge density using the Broyden/Pullay mixing scheme. The self-consistent procedure continues until the change in the total energy is less than a chosen convergence energy.

VASP implements a wide range of exchange-correlation functionals. These include LDA (for example the functional by Perdew and Zunger [139]) and GGA (for example the functional by Perdew *et al* in 1991 (PW91) [140, 141]), as well as meta- and hyper-GGA

functionals (PKZB by Perdew *et al* [142, 143] for meta-GGA) and hybrid functionals (B3LYP by Becke [144, 145], PBE0 by Perdew *et al* in 1996 [146, 147] and HSE03 by Heyd *et al* [148, 149]). All of the functionals included in VASP have spin-degenerate and spin-polarised versions [150].

VASP calculates the forces on atoms (and the full stress tensor), which are then used to optimise the atomic configuration (relaxing the atoms and minimising the energy).

For all of the structures considered in this work, the equilibrium lattice constants were calculated by a full relaxation of the atoms. The elastic constants were calculated at the groundstate structure, as well as the energy band structures, density of states (DOS) and partial DOS.

The VASP code [151, 152, 124, 125] using the PAW potentials [122, 123] was used for all of the electronic structure calculations in this work. The exchange-correlation functional implemented was within the GGA approximation, using the functional by Perdew *et al* (PBE) in 1996 [146, 147]. A $12 \times 12 \times 12$ Monkhorst Pack **k**-point mesh was used for all of the calculations for the integration of the BZ. The cutoff energy was 500 eV, also for all of the calculations. It was found that this choice of cutoff energy and **k**-point mesh, as a standard for all the phases considered, provided accurate values for the equilibrium lattice constants and hence the elastic constants and moduli, the energy band structure and the DOS calculations. The electronic iterations convergence for the calculations was 1×10^{-7} eV, using the normal (blocked Davidson) algorithm. Fermi smearing was used, with a width of 0.2 eV.

2.11 Equilibrium Lattice for Pt, Ir and Ti

The first part of the compuations involves finding the equilibrium lattices for Pt, Ir and Ti. This is done by calculating the energy of a structure with respect to its volume and fitting the data to obtain the equilibrium energy and volume, from which the equilibrium lattice constant(s) can then be found. The bulk modulus B is also calculated using the fit.

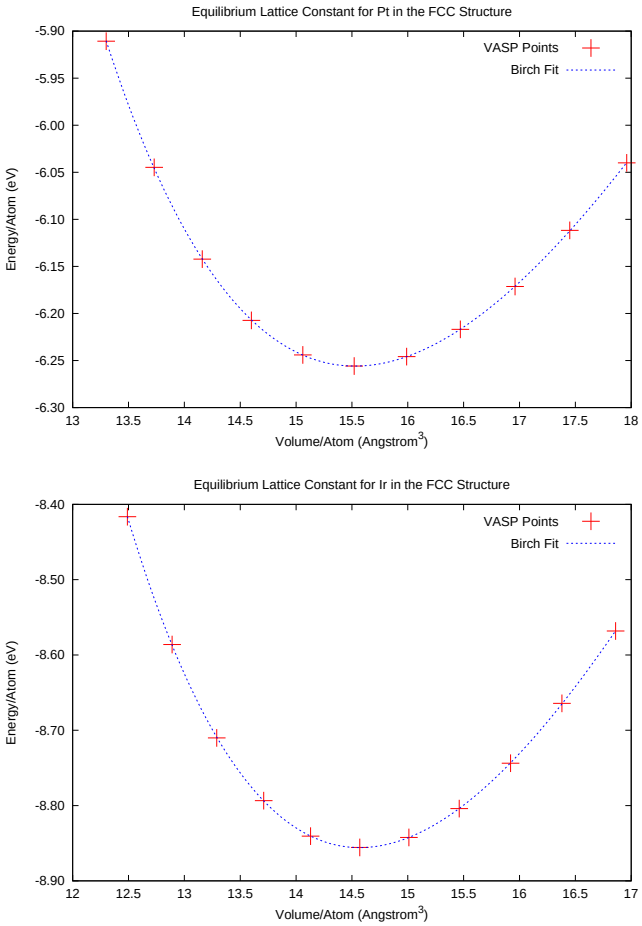

Figure 2.2:
The equation of state for Pt and Ir in the FCC structure. The equilibrium energy and lattice constant, as well as the bulk modulus, is then found by a least squares fit by Birch (1978) [153].

For cubic structures, there is only one parameter needed to specify the system. This can be the lattice constant a or the volume. In this case, the lattice constant is varied up to 5% of the expected equilibrium value and the total energy is calculated as a function of the volume corresponding to the lattice constant. The plots of energy versus volume for FCC Pt and Ti are given in Figure 2.2.

The energy-volume data is used with a least squares fit given by Birch (1978) [153] to find the equilibrium energy and volume. The form of the Birch fit is given by

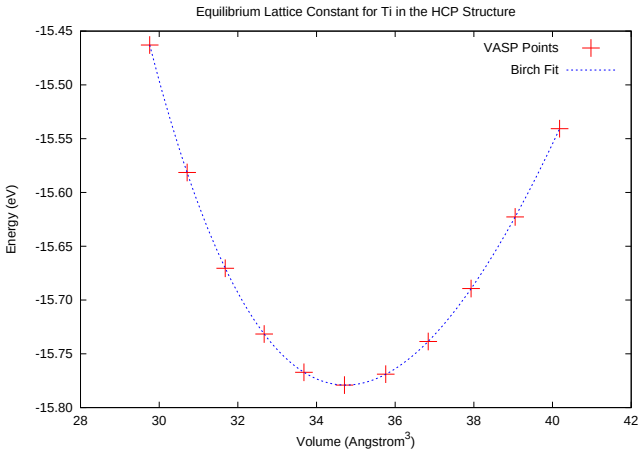

Figure 2.3:
The equation of state for Ti in the HCP structure, where the volume is varied keeping the c/a ratio fixed. The equilibrium energy and lattice constant, as well as the bulk modulus, is then found by a least squares fit by Birch (1978) [153].

$$E_{\text{BIRCH}} = E_0 + \frac{9}{8} B_0 V_0 \left[(V_0/V)^{2/3} - 1) \right]^2 + \frac{9}{16} B_0 V_0 (B_0' - 4) \left[(V_0/V)^{2/3} - 1) \right]^3 + \sum_{n=4}^{N} \gamma_n \left[(V_0/V)^{2/3} - 1) \right]^n . \tag{2.58}$$

In Equation 2.58 E_0 is the equilibrium energy, V_0 the equilibrium volume, B the bulk modulus, B_0' is the pressure derivative of the bulk modulus and N is the order of the fit. The fit used here is chosen to be a second order fit, so B_0' is set to 4. The pressure derivative B_0' is generally found to be between 3 and 5 [154].

For Ti in the HCP structure, the system is defined by the lattice constant a and the ratio of with the lattice constant c. Finding the equilibrium structure is done in two steps. In the first step, the ratio c/a which minimises the energy is found first. Then the volume of the cell is varied while keeping $(c/a)_0$, the ratio which gives the minimum, fixed. The data is fitted once more with the Birch fit (Equation 2.58) to obtain the equilibrium constants and bulk modulus. The graph of energy versus volume while keeping $(c/a)_0$ fixed is shown in Figure 2.3.

The calculated equilibrium values for FCC Pt and Ir, and HCP Ti are given in Table 2.1. It can be seen that the lattice constants for Pt and Ir are about 1% different from the

	a_0 (Å)						B (GPa)					
	This	Mehl *et al*[a]					This	Mehl *et al*[a]				
	work	TB	LAPW	Exp			work	TB	LAPW	Exp		
Pt	3.960	3.90	3.90	3.92	3.99[b]	3.924[c]	248.51	318	305	278	257.9[b]	356.3[c]
Ir	3.877	3.86	3.82	3.84	3.82[d]	3.961[e]	345.82	389	401	355	402[d]	381.3[e]
Ti	2,938	2.97	2.87	2.95		2.951[f]	112.25	122	120	105		
	c_0 (Å)											
Ti	4.648	4.80	4.55	4.68		4.684[f]						

Table 2.1:
The elastic constants of FCC Pt and Ir, and HCP Ti. [a]Ref [69]. [b]Ref [13]. [c]Ref [155]. [d]Ref [154]. [e]Ref [50]. [f]Ref [156].

experimental values, while a_0 and c_0 for Ti are about 0.5% different. The lattice constants are also in good agreement with other theoretical results shown. The bulk moduli show a percentage difference of 10% for Pt and less than that for Ir and Ti.

From Table 2.1 it is seen that the equilibrium constants and bulk moduli for the bulk systems are in good agreement with both experimental and other theoretical values. The equilibrium constants for both Pt-Ti and Ir-T alloys, for different phases and stoichiometries, can then be found with confidence that these values will also correspond to available data in the literature.

2.12 Determining Elastic Constants

2.12.1 Elasticity

The relationship between stress and strain is most generally written mathematically as

$$\sigma_{ij} = C_{ijkl}\epsilon_{kl}. \tag{2.59}$$

Hooke's Law states that the strain (the amount of deformation of a material) on a material is directly proportional to the stress (the force that causes the deformation). In three dimensions, the stress tensor σ_{ij} in Equation 2.59 is related to the strain tensor ϵ_{ij} via the fourth-rank tensor C_{ijkl}. The C_{ijkl} are the elastic constants, of which there are 81.

The number of actual independent elastic constants is 21; this number is further reduced depending on the symmetry of the system.

Written in matrix notation, the stress and strain tensors can be written as six-dimensional vectors by using the tensors' symmetry:

$$[\sigma] = \begin{bmatrix} \sigma_{11} \\ \sigma_{22} \\ \sigma_{33} \\ \sigma_{23} \\ \sigma_{31} \\ \sigma_{12} \end{bmatrix} = \begin{bmatrix} \sigma_1 \\ \sigma_2 \\ \sigma_3 \\ \sigma_4 \\ \sigma_5 \\ \sigma_6 \end{bmatrix}, \tag{2.60}$$

and

$$[\epsilon] = \begin{bmatrix} \epsilon_{11} \\ \epsilon_{22} \\ \epsilon_{33} \\ 2\epsilon_{23} \\ 2\epsilon_{31} \\ 2\epsilon_{12} \end{bmatrix} = \begin{bmatrix} \epsilon_1 \\ \epsilon_2 \\ \epsilon_3 \\ \epsilon_4 \\ \epsilon_5 \\ \epsilon_6 \end{bmatrix}. \tag{2.61}$$

The elastic constants are then given as

$$[C] = \begin{bmatrix} C_{1111} & C_{1122} & C_{1133} & C_{1123} & C_{1131} & C_{1112} \\ C_{2211} & C_{2222} & C_{2233} & C_{2223} & C_{2231} & C_{2212} \\ C_{3311} & C_{3322} & C_{3333} & C_{3323} & C_{3331} & C_{3312} \\ C_{2311} & C_{2322} & C_{2333} & C_{2323} & C_{2331} & C_{2312} \\ C_{3111} & C_{3122} & C_{3133} & C_{3132} & C_{3131} & C_{3112} \\ C_{1211} & C_{1222} & C_{1233} & C_{1232} & C_{1231} & C_{1212} \end{bmatrix} = \begin{bmatrix} C_{11} & C_{12} & C_{13} & C_{14} & C_{15} & C_{16} \\ C_{12} & C_{22} & C_{23} & C_{24} & C_{25} & C_{26} \\ C_{13} & C_{23} & C_{33} & C_{34} & C_{35} & C_{36} \\ C_{14} & C_{24} & C_{34} & C_{44} & C_{45} & C_{46} \\ C_{15} & C_{25} & C_{35} & C_{45} & C_{55} & C_{56} \\ C_{16} & C_{26} & C_{36} & C_{46} & C_{56} & C_{66} \end{bmatrix}. \tag{2.62}$$

This is done using the Voigt notation, taking a symmetric tensor and reducing its order, so that the stress-strain relation can be written as

$$\sigma_i = C_{ij}\epsilon_j. \tag{2.63}$$

This comes about from the symmetry of the stress tensor ($\sigma_{ij} = \sigma_{ji}$), which implies that $C_{ijkl} = C_{jikl}$. Since the strain tensor is also symmetric, this implies that $C_{ijkl} = C_{ijlk}$.

Hence the number of independent elastic constants is drastically reduced.

The work done dE by the stress components σ_{ij} on a material so that the strain components increase by an amount $d\epsilon_{ij}$ is given by

$$dE = \sigma_{ij} d\epsilon_{ij}. \tag{2.64}$$

Here, E is called the strain energy density (per unit volume), from which the following relation arises

$$\sigma_{ij} = \frac{\partial E}{\partial \epsilon_{ij}}. \tag{2.65}$$

Equation 2.59 is given from the definition of the elastic constants,

$$C_{ijkl} = \frac{\partial \sigma_{ij}}{\partial \epsilon_{kl}}. \tag{2.66}$$

By combining Equations 2.65 and 2.66, one arrives at

$$C_{ijkl} = \frac{\partial^2 E}{\partial \epsilon_{ij} \partial \epsilon_{kl}}. \tag{2.67}$$

Using the Voigt notation once more, the elastic constants can be written as

$$C_{ij} = \frac{\partial^2 E}{\partial \epsilon_i \partial \epsilon_j}. \tag{2.68}$$

By writing the symmetric strain tensor ϵ as

$$\epsilon = \begin{pmatrix} \epsilon_1 & \epsilon_6/2 & \epsilon_5/2 \\ \epsilon_6/2 & \epsilon_2 & \epsilon_4/2 \\ \epsilon_5/2 & \epsilon_4/2 & \epsilon_6 \end{pmatrix}, \tag{2.69}$$

a lattice may be strained so that the primitive vectors defining the lattice are transformed into new vectors by

$$\begin{pmatrix} \mathbf{a'} \\ \mathbf{b'} \\ \mathbf{c'} \end{pmatrix} = \begin{pmatrix} \mathbf{a} \\ \mathbf{b} \\ \mathbf{c} \end{pmatrix} \cdot (I + \epsilon), \tag{2.70}$$

where I is the identity matrix [154]∗. If the strains ϵ_i are small, the change in energy in the lattice can be written as a Taylor expansion to second-order of the strain components as

$$E(\epsilon_i) = E(0) + \sum_i^6 \frac{\partial E}{\partial \epsilon_i} \epsilon_i + \frac{1}{2} \sum_{i,j}^6 \frac{\partial^2 E}{\partial \epsilon_i \partial \epsilon_j} \epsilon_i \epsilon_j + O[\epsilon_i^3]. \tag{2.71}$$

When $E(0)$ is the equilibrium energy at the unstrained lattice of volume V, or when the strain is volume-conserving, the linear term vanishes and the energy versus strain relation becomes

$$E(\epsilon_i) = E(0) + \frac{1}{2}\sum_{i,j}^{6} \frac{\partial^2 E}{\partial \epsilon_i \partial \epsilon_j}\epsilon_i \epsilon_j + O[\epsilon_i^3] = E(0) + \frac{1}{2}\sum_{i,j}^{6} C_{ij}\epsilon_i \epsilon_j + O[\epsilon_i^3]. \tag{2.72}$$

All of the elastic constants may be obtained by straining a lattice using the transformation in Equation 2.70, and allowing the relaxing of the internal parameters [154]. As stated before, there are 21 independent elastic constants. The symmetry of a system may reduce this number, except in the case of a triclinic crystal system, which does have 21 independent elastic constants.

In monoclinic systems, symmetry is exhibited with respect to one plane. There is invariance under z-axis inversion. Let $\mathbf{Q}_1$ be an orthogonal matrix that has components c_{ij}. The transformation that corresponds to symmetry with respect to the one plane is

$$\mathbf{Q}_1 = [c_{ij}] = \begin{bmatrix} 1 & 0 & 0 \\ 0 & 1 & 0 \\ 0 & 0 & -1 \end{bmatrix}. \tag{2.73}$$

Given that the generalised Hooke's Law has the form of Equation 2.59 in set of Cartesian coordinates, in another coordinate system

$$\sigma_{kl}^* = C_{klst}^* \epsilon_{st}^*, \tag{2.74}$$

then for coordinate indifference, whereby Equation 2.59 holds in all Cartesian coordinate systems

$$C_{klst}^* = C_{mnpr} c_{km} c_{ln} c_{sp} c_{tr}. \tag{2.75}$$

Given the transformation $\mathbf{Q}_1$, the condition $C_{ijkl}^* = C_{ijkl}$ must still hold. Using the transformation in Equation 2.75 gives $C_{1111}^* = C_{1111}$. However, using another example, $C_{1123}^* = -C_{1123}$, which implies that

$$C_{1123} = 0. \tag{2.76}$$

It can be shown that there are eight elastic constants in total that are zero, so that there are 13 remaining independent elastic constants for a monoclinic system. Therefore

$$[C] = \begin{bmatrix} C_{1111} & C_{1122} & C_{1133} & 0 & 0 & C_{1112} \\ C_{1122} & C_{2222} & C_{2233} & 0 & 0 & C_{2212} \\ C_{1133} & C_{2233} & C_{3333} & 0 & 0 & C_{3312} \\ 0 & 0 & 0 & C_{2323} & C_{2331} & 0 \\ 0 & 0 & 0 & C_{2331} & C_{3131} & 0 \\ C_{1112} & C_{2212} & C_{3312} & 0 & 0 & C_{1212} \end{bmatrix} = \begin{bmatrix} C_{11} & C_{12} & C_{13} & 0 & 0 & C_{16} \\ C_{12} & C_{22} & C_{23} & 0 & 0 & C_{26} \\ C_{13} & C_{23} & C_{33} & 0 & 0 & C_{36} \\ 0 & 0 & 0 & C_{44} & C_{45} & 0 \\ 0 & 0 & 0 & C_{45} & C_{55} & 0 \\ C_{16} & C_{26} & C_{36} & 0 & 0 & C_{66} \end{bmatrix}. \tag{2.77}$$

For orthorhombic systems, the elastic constants are symmetrical with respect to two orthogonal planes. This means there is invariance under the inversion of any two of its axes, leading to nine independent elastic constants. In such a system there is symmetry given by the transformation matrix $\mathbf{Q}_1$ (Equation2.73) as well by a second transformation matrix

$$\mathbf{Q}_2 = [c_{ij}] = \begin{bmatrix} -1 & 0 & 0 \\ 0 & 1 & 0 \\ 0 & 0 & 1 \end{bmatrix}. \tag{2.78}$$

The number of elastic constants is reduced as $C_{1112} = C_{2212} = C_{3312} = C_{2331} = 0$. The elastic constant matrix for an orthorhombic material then becomes

$$[C] = \begin{bmatrix} C_{1111} & C_{1122} & C_{1133} & 0 & 0 & 0 \\ C_{1122} & C_{2222} & C_{2233} & 0 & 0 & 0 \\ C_{1133} & C_{2233} & C_{3333} & 0 & 0 & 0 \\ 0 & 0 & 0 & C_{2323} & 0 & 0 \\ 0 & 0 & 0 & 0 & C_{3131} & 0 \\ 0 & 0 & 0 & 0 & 0 & C_{1212} \end{bmatrix} = \begin{bmatrix} C_{11} & C_{12} & C_{13} & 0 & 0 & 0 \\ C_{12} & C_{22} & C_{23} & 0 & 0 & 0 \\ C_{13} & C_{23} & C_{33} & 0 & 0 & 0 \\ 0 & 0 & 0 & C_{44} & 0 & 0 \\ 0 & 0 & 0 & 0 & C_{55} & 0 \\ 0 & 0 & 0 & 0 & 0 & C_{66} \end{bmatrix}. \tag{2.79}$$

A system that shows symmetry with respect to two planes is called orthotropic.

Tetragonal systems are orthotropic, where properties are the same with respect to two planes and different along the third axis. With a transformation matrix similar to those in Equations 2.73 and 2.78, it can be shown that the elastic constants for a tetragonal matrix are

$$[C] = \begin{bmatrix} C_{1111} & C_{1122} & C_{1133} & 0 & 0 & 0 \\ C_{1122} & C_{1111} & C_{1133} & 0 & 0 & 0 \\ C_{1133} & C_{1133} & C_{3333} & 0 & 0 & 0 \\ 0 & 0 & 0 & C_{2323} & 0 & 0 \\ 0 & 0 & 0 & 0 & C_{2323} & 0 \\ 0 & 0 & 0 & 0 & 0 & C_{1212} \end{bmatrix} = \begin{bmatrix} C_{11} & C_{12} & C_{13} & 0 & 0 & 0 \\ C_{12} & C_{11} & C_{13} & 0 & 0 & 0 \\ C_{13} & C_{13} & C_{33} & 0 & 0 & 0 \\ 0 & 0 & 0 & C_{44} & 0 & 0 \\ 0 & 0 & 0 & 0 & C_{44} & 0 \\ 0 & 0 & 0 & 0 & 0 & C_{66} \end{bmatrix}, \tag{2.80}$$

of which there are seven independent elastic constants. Ashcroft and Mermin [83] state that the maximum number of independent elastic constants for a tetragonal system depends on the point groups of the system, in which case some have only six independent elastic constants. Equation 2.80 shows six independent elastic constants.

Hexagonal systems as well as systems where there is plane isotropy show invariance under rotations of 60° about the z-axis. Such systems have five independent elastic constants:

$$[C] = \begin{bmatrix} C_{1111} & C_{1122} & C_{1133} & 0 & 0 & 0 \\ C_{1122} & C_{1111} & C_{1133} & 0 & 0 & 0 \\ C_{1133} & C_{1133} & C_{3333} & 0 & 0 & 0 \\ 0 & 0 & 0 & C_{2323} & 0 & 0 \\ 0 & 0 & 0 & 0 & C_{2323} & 0 \\ 0 & 0 & 0 & 0 & 0 & C_{1212} \end{bmatrix} = \begin{bmatrix} C_{11} & C_{12} & C_{13} & 0 & 0 & 0 \\ C_{12} & C_{11} & C_{13} & 0 & 0 & 0 \\ C_{13} & C_{13} & C_{33} & 0 & 0 & 0 \\ 0 & 0 & 0 & C_{44} & 0 & 0 \\ 0 & 0 & 0 & 0 & C_{44} & 0 \\ 0 & 0 & 0 & 0 & 0 & C_{66} \end{bmatrix}, \tag{2.81}$$

where the elastic constant C_{66} is given by $\frac{1}{2}(C_{11} - C_{12})$.

A cubic system shows invariance under 90° rotations about all three axes, resulting in three independent elastic constants:

$$[C] = \begin{bmatrix} C_{1111} & C_{1122} & C_{1122} & 0 & 0 & 0 \\ C_{1122} & C_{1111} & C_{1122} & 0 & 0 & 0 \\ C_{1122} & C_{1122} & C_{1111} & 0 & 0 & 0 \\ 0 & 0 & 0 & C_{2323} & 0 & 0 \\ 0 & 0 & 0 & 0 & C_{2323} & 0 \\ 0 & 0 & 0 & 0 & 0 & C_{2323} \end{bmatrix} = \begin{bmatrix} C_{11} & C_{12} & C_{12} & 0 & 0 & 0 \\ C_{12} & C_{11} & C_{12} & 0 & 0 & 0 \\ C_{12} & C_{12} & C_{11} & 0 & 0 & 0 \\ 0 & 0 & 0 & C_{44} & 0 & 0 \\ 0 & 0 & 0 & 0 & C_{44} & 0 \\ 0 & 0 & 0 & 0 & 0 & C_{44} \end{bmatrix}. \tag{2.82}$$

Finally, a system that is fully isotropic is one where there is invariance under any rotation or any inversion about any axis:

$$[C] = \begin{bmatrix} C_{1111} & C_{1122} & C_{1122} & 0 & 0 & 0 \\ C_{1122} & C_{1111} & C_{1122} & 0 & 0 & 0 \\ C_{1122} & C_{1122} & C_{1111} & 0 & 0 & 0 \\ 0 & 0 & 0 & C_{2323} & 0 & 0 \\ 0 & 0 & 0 & 0 & C_{2323} & 0 \\ 0 & 0 & 0 & 0 & 0 & C_{2323} \end{bmatrix} = \begin{bmatrix} C_{11} & C_{12} & C_{12} & 0 & 0 & 0 \\ C_{12} & C_{11} & C_{12} & 0 & 0 & 0 \\ C_{12} & C_{12} & C_{11} & 0 & 0 & 0 \\ 0 & 0 & 0 & C_{44} & 0 & 0 \\ 0 & 0 & 0 & 0 & C_{44} & 0 \\ 0 & 0 & 0 & 0 & 0 & C_{44} \end{bmatrix}. \tag{2.83}$$

Isotropic materials have only two independent elastic constants, since C_{11} and C_{12} are related to C_{44} by

$$C_{44} = \frac{1}{2}(C_{11} - C_{12}). \tag{2.84}$$

The elastic constants can now be obtained by applying appropriate deformations to the unit cell. The changes in energy due to the deformations are then fitted to a polynomial, which is used to extract the elastic constants [157].

2.12.2 Elastic Constants for Pt and Ir

For cubic materials, the bulk modulus B is related to the elastic constants by [154]

$$B = \frac{1}{3}(C_{11} + 2C_{12}). \tag{2.85}$$

Having found the bulk modulus for both Pt and Ir in the FCC structure using energy versus volume calculations and using the Birch fit, at least two sets of strains need to be applied to the structures to obtain all of the elastic constants. Two sets of strains are used to calculate $C_{11},\ C_{12}$ and C_{44} for both Pt and Ir.

The first set is by Mehl *et al* [154]. Volume-conserving orthorhombic and monoclinic strains are used to compute $C_{11} - C_{12}$ and C_{44} respectively. The applied strains are as follows: for $C_{11} - C_{12}$

$$\epsilon_1 = x,\ \epsilon_2 = -x$$
$$\epsilon_3 = x^2/(1 - x^2) \tag{2.86}$$

$$\epsilon_4 = \epsilon_5 = \epsilon_6 = 0,$$

and for C_{44}

$$\begin{aligned} \epsilon_6 &= x \\ \epsilon_3 &= x^2/(4-x^2) \\ \epsilon_1 &= \epsilon_2 = \epsilon_4 = \epsilon_5 = 0. \end{aligned} \tag{2.87}$$

These choices for straining the cubic lattice have the advantage of being an even function in x, so that the energy change has the following property: $\Delta E(x) = \Delta E(-x)$. This allows for fewer computations to calculate the elastic constants. By using the strains in Equations 2.86 and 2.87 and Equation 2.72, the change in the total energy is calculated as follows:

$$\begin{aligned} C_{11} - C_{12}: \quad \Delta E(x) &= \frac{1}{2} V \left[C_{11}x^2 - C_{12}x^2 - C_{12}x^2 + C_{11}x^2 \right] + O[x^4] \\ &= \frac{1}{2} V \left[C_{11} - C_{12} \right] x^2 + O[x^4]. \end{aligned} \tag{2.88}$$

$$\begin{aligned} C_{44}: \quad \Delta E(x) &= \frac{1}{2} V \left[C_{11} \left(x^4/(4-x^2)^2 \right) + C_{44}x^2 \right] + O[x^4] \\ &= \frac{1}{2} V C_{44} x^2 + O[x^4]. \end{aligned} \tag{2.89}$$

The value of the strain x is chosen to be no larger than 0.10. The energy is calculated for different values of x and Gnuplot is used to fit the data to a polynomial. The graphs of the energy versus strain is given in Figure 2.4. As can be seen from the graphs, the energy is close to a linear function of the squared strain x^2 as expected. As the energy increases with strain, the FCC phase is seen to be the ground state.

Using the fit, $C_{11} - C_{12}$ is found to be 90.1 GPa, and C_{44} is 46.6 GPa. The values of the elastic constants for Pt are shown in Table 2.2.

To further verify the value of the elastic constants another set of strains is used. According to Chen *et al* [50] a tetragonal distortion may be represented in the form

$$\epsilon = \begin{pmatrix} \frac{1}{2}\delta & 0 & 0 \\ 0 & \frac{1}{2}\delta & 0 \\ 0 & 0 & \delta \end{pmatrix}, \tag{2.90}$$

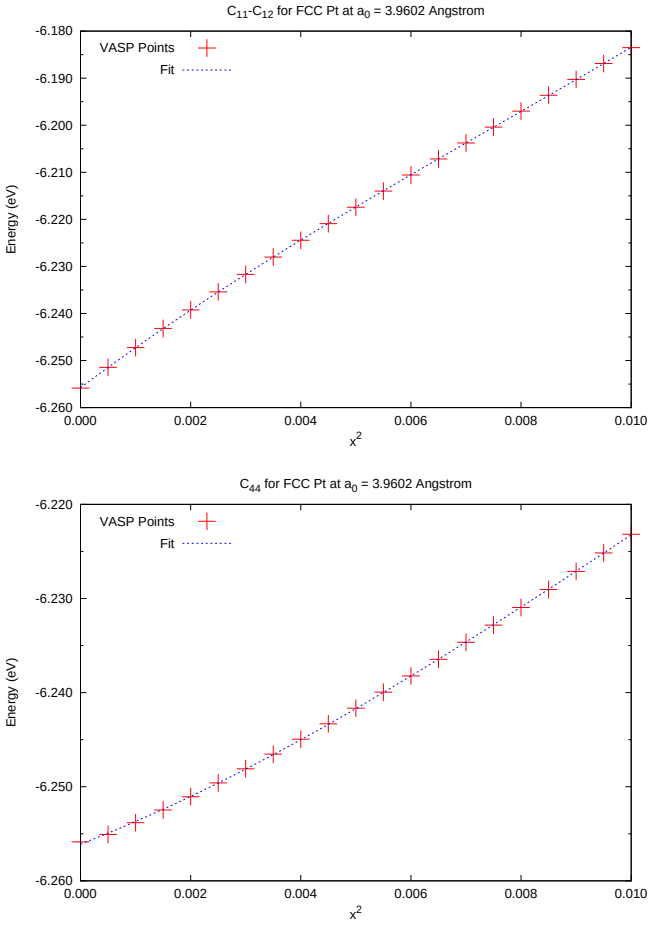

Figure 2.4:
The graphs of energy versus (strain)^2 to calculate $C_{11} - C_{12}$ and C_{44} as defined by Mehl *et al* [154].

where ϵ is the strain tensor that is used in Equation 2.70. Equation 2.72 then becomes

$$\Delta E(\delta) = \frac{3}{4} V(C_{11} - C_{12})\delta^2. \tag{2.91}$$

A trigonal distortion is used to calculate C_{44}. The strain tensor is given by

$$\epsilon = \begin{pmatrix} 0 & \delta & 0 \\ \delta & 0 & 0 \\ 0 & 0 & 0 \end{pmatrix}, \tag{2.92}$$

so that the energy change is given by

$$\Delta E(\delta) = 2VC_{44}\delta^2. \tag{2.93}$$

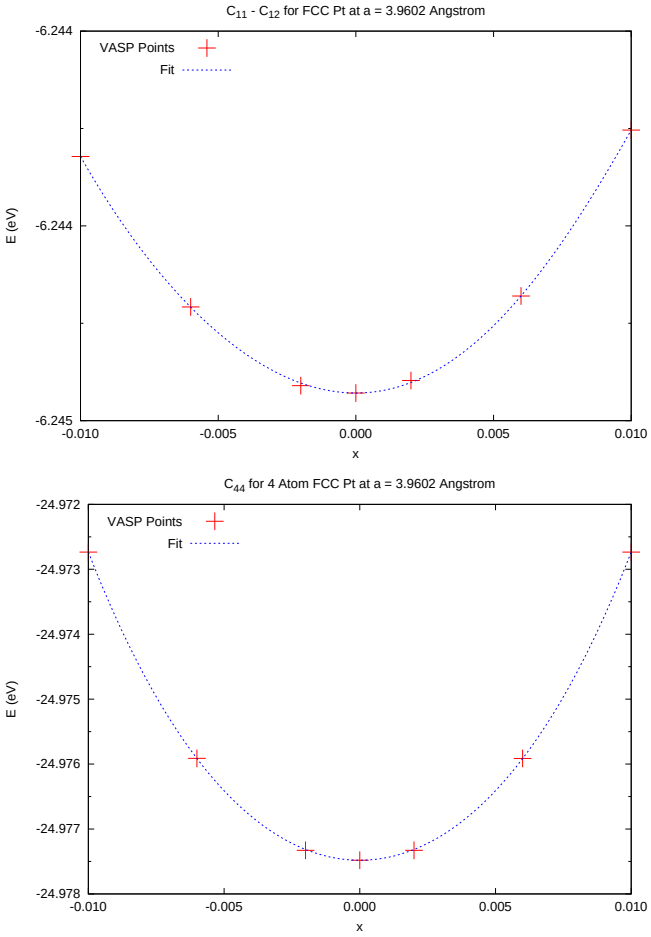

Figure 2.5:
The graphs of energy versus strain to calculate $C_{11} - C_{12}$ and C_{44} as defined by Chen *et al* [50].

The values of the elastic constants for Pt using this second set of strains is given in Table 2.2, showing good agreement with the first set of strains by Mehl *et al* [154]. The graphs of the energy change due to Chen *et al* [50] strains are shown in Figure 2.5. It can be seen from the graphs that these strains are not even functions of δ as before.

An additional strain is used to calculate the bulk modulus B. The strains as given by Lowther (2006) (Reference [157]) show that for a cubic system, a strain of the form

$$\epsilon = \begin{pmatrix} x & 0 & 0 \\ 0 & x & 0 \\ 0 & 0 & x \end{pmatrix}, \tag{2.94}$$

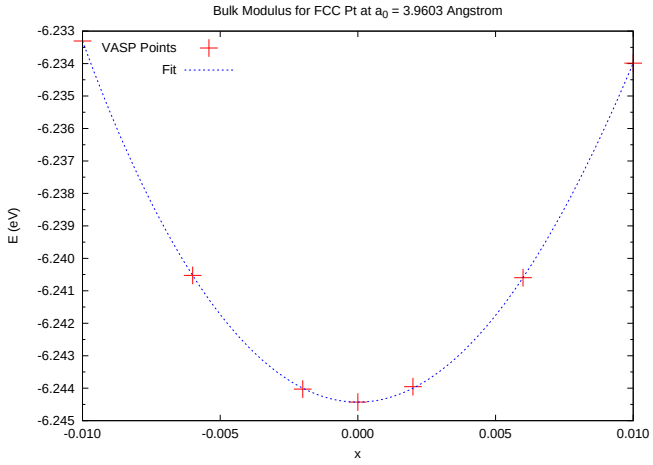

Figure 2.6:
The graph of energy versus strain to calculate the bulk modulus B using the strain by Lowther (2006) [157].

gives an energy change of the form

$$\begin{aligned} \Delta E(x) &= \frac{3}{2}V[C_{11}+2C_{12}]x^2 \\ &= \frac{9}{2}V[(C_{11}+2C_{12})/3]x^2, \end{aligned} \tag{2.95}$$

which then leads to the bulk modulus B via Equation 2.85. In this case the energy change is similar to the energy versus volume calculations that were used to calculate the equilibrium lattice constant and the bulk modulus. However, the bulk modulus is not calculated using the Birch fit, but rather by fitting the energy to a poynomial similar to the ones used in the Chen *et al* [50] strains.

The strains 2.86, 2.87, 2.91, 2.93 and 2.95 are also used to calculate the elastic constants for FCC Ir. These are shown in Table 2.2, together with the elastic constants of Pt. The bulk modulus B calculated with the strain 2.95 was used to calculate C_{11}, C_{12} and C_{44} for Pt and Ir: 246.0 GPa and 344.7 GPa respectively. These bulk moduli represent a 0.9% and 0.3% difference, respectively, to the bulk moduli calculated for the metals using the Birch fit.

Comparing the elastic constants in this work with other results, the values for Ir fare better than those for Pt. The percentage differences between the Pt calculated and experimental

	C_{11} (GPa)					C_{12} (GPa)					C_{44} (GPa)				
	This	Mehl[a]				This	Mehl[a]				This	Mehl[a]			
	work	TB	LAPW	Exp		work	TB	LAPW	Exp		work	TB	LAPW	Exp	
Pt	306.1	380	381	347	308[b]	216.0	257	189	251	233[b]	46.6	71	83	76	66[b]
	306.4					215.8					53.2				
Ir	578.5	694	621	590	635[c]	227.8	260	256	249	255[c]	240.6	348	260	262	269[c]
	575.4					229.3					247.5				

Table 2.2:
The elastic constants of FCC Pt and Ir. [a]Ref [69], [b]Ref [13], [c]Ref [50].

elastic values are 11.7% for C_{11}, 13.9% for C_{12} and 36.1% for C_{44}. For Ir, the percentage differences are 2.5% for C_{11}, 8.5% for C_{12} and 8.1% for C_{44}.

The larger difference between the experimental and calculated elastic constants for Pt may be due to the lattice constant a_0 of bulk Pt in the FCC structure. Mehl and Papaconstantopoulos [69] state an experimental bulk modulus of 278 GPa for Pt, at an equilibrium structure with $a_0 = 3.92$ Å. The Pt elastic constants given in Table 2.2 are calculated at a lattice constant of 3.96 Å. The difference in the energy-strain calculated bulk modulus and the experimental value is 11.5%. In contrast, this difference is only 2.9% in Ir, where the calculated and experimental lattice constants are 3.88 Å and 3.84 Å respectively.

2.12.3 Elastic Constants for Ti

To calculate the elastic constants for Ti in HCP, five different strains are used. The first three strains will calculate the diagonal terms of the elastic constant matrix. Using these values in the strain tensor (Equation 2.69)

$$\epsilon_1 = x,\ \epsilon_2 = \epsilon_3 = \epsilon_4 = \epsilon_5 = \epsilon_6 = 0, \tag{2.96}$$

gives the change in energy equation

$$\Delta E(x) = \frac{1}{2} V C_{11} x^2. \tag{2.97}$$

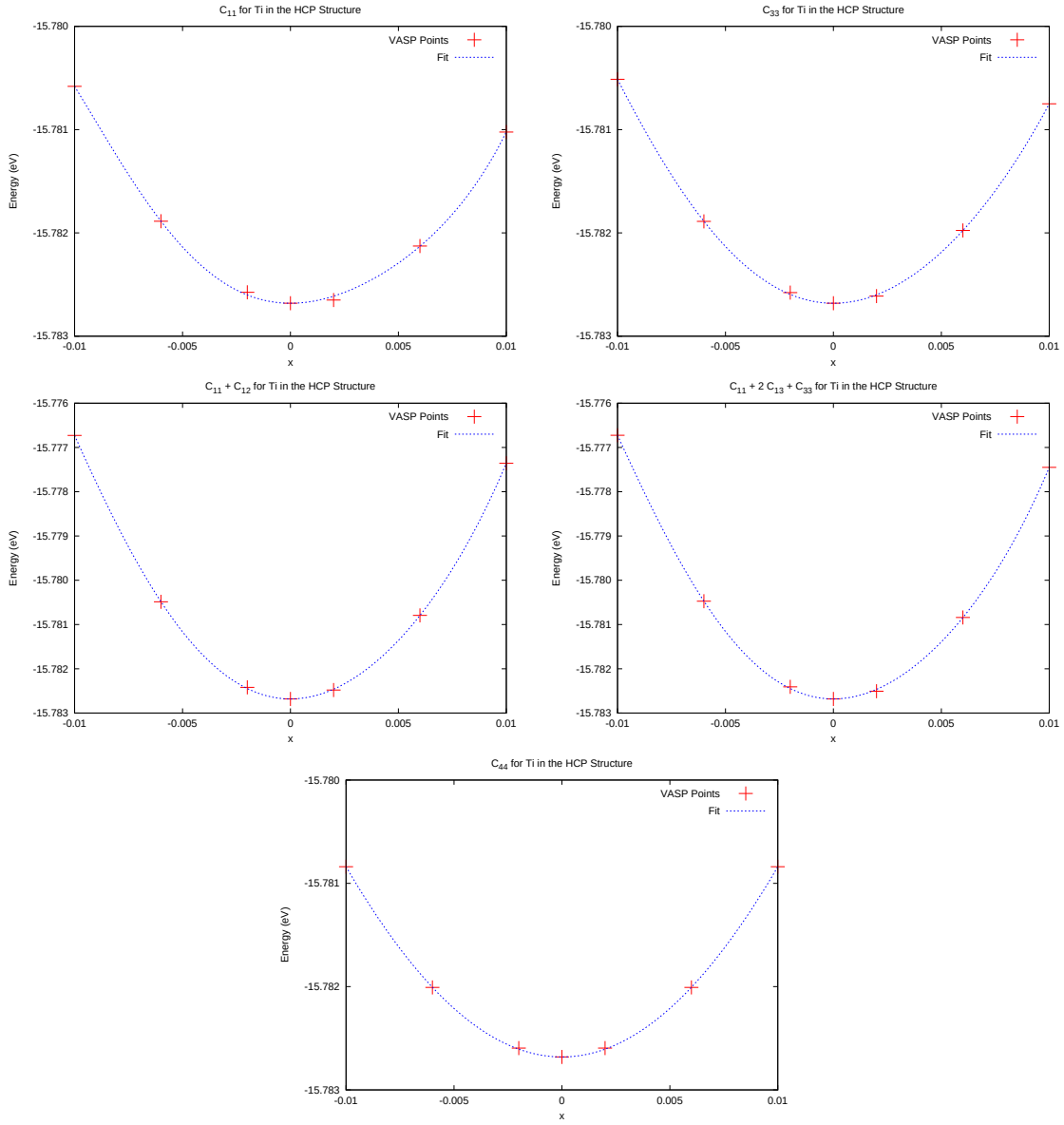

Figure 2.7:
The graphs showing the five strains used to calculate the elastic constants of Ti in the HCP structure.

To calculate C_{33}, the strain tensor is given by

$$\epsilon_3 = x, \ \epsilon_1 = \epsilon_2 = \epsilon_4 = \epsilon_5 = \epsilon_6 = 0, \tag{2.98}$$

so that

$$\Delta E(x) = \frac{1}{2} V C_{33} x^2. \tag{2.99}$$

Finally, to calculate C_{44}, the strain tensor is

$$\epsilon_4 = 2x, \ \epsilon_1 = \epsilon_2 = \epsilon_3 = \epsilon_5 = \epsilon_6 = 0. \tag{2.100}$$

C_{11} (GPa)			C_{12} (GPa)			C_{13} (GPa)			C_{33} (GPa)			C_{44} (GPa)		
	TB	Exp		TB	Exp		TB	Exp		TB	Exp		TB	Exp
171.9	171	160	90.5	58	90	77.3	46	60	193.7	203	181	43.6	64	47

Table 2.3:
The elastic constants of HCP Ti. The tight-binding (TB) parametrization and experimental values are from Ref [69].

The change in energy for this strain then becomes

$$\Delta E(x) = 2VC_{44}x^2. \tag{2.101}$$

The off-diagonal elastic constants are calculated using the following strains. Firstly C_{12} can be calculated using

$$\epsilon_1 = \epsilon_2 = x,\ \epsilon_3 = \epsilon_4 = \epsilon_5 = \epsilon_6 = 0. \tag{2.102}$$

C_{12} is then found using C_{11} from above. The last strain to complete the set is

$$\epsilon_1 = \epsilon_3 = x,\ \epsilon_2 = \epsilon_4 = \epsilon_5 = \epsilon_6 = 0. \tag{2.103}$$

These two strains result in the change in energy equations

$$\Delta E(x) = V(C_{11} + C_{44})x^2, \tag{2.104}$$

and

$$\Delta E(x) = \frac{1}{2}V(C_{11} + 2C_{13} + C_{33})x^2. \tag{2.105}$$

The final elastic constant C_{66} is found using C_{11} and C_{12} and

$$C_{66} = \frac{1}{2}(C_{11} - C_{12}), \tag{2.106}$$

which is calculated to be 40.7 GPa.

The energy versus strain graphs for the five strains to calculate the elastic constants are given in Figure 2.7 and the value of the elastic constants is given in Table 2.3. The percentage difference between experimental and calculated elastic constants is about 7% for C_{11}, C_{33} and C_{44}. C_{12} only has a 0.6% difference, whereas for C_{13} the percentage

difference is 28.8%.

For a hexagonal lattice, the bulk modulus B is given by the elastic constants by

$$B = \frac{(C_{11} + C_{12})C_{33} - 2C_{13}^2}{C_{11} + C_{12} + 2C_{33} - 4C_{13}}. \tag{2.107}$$

Using set of elastic constants listed in Table 2.3, the bulk modulus is calculated to be 114.1 GPa, compared to the value given by the energy-volume curve of 112.25 GPa (Table 2.1).

Chapter 3

The Pt-Ti System

3.1 Equilibrium Phases in the Pt-Ti System

The various phases of the Pt-Ti system and the crystal structure data are shown in Table 3.1. The phases that are reported in Fernando *et al* [60] are explored here, as well as others from different authors. The equilibrium structures for each percentage composition are determined. Different phases at the same composition are also explored.

It can be seen that Pt-rich alloys are favoured. There is so far only one phase that has a higher percentage concentration of Ti, that is the $PtTi_3$ phase which forms in the Cr_3Si ($A15$) structure. The 50-50% composition shows the highest values of heats of formation; this will be presented in the following section.

Pt-rich phases include Pt_3Ti, which crystallizes in the cubic Cu_3Au ($L1_2$) structure. Pt_8Ti is a tetragonal structure reported by Pietrokowsky (1965) [158], while Curtarolo *et al* [71] reports a phase at 33% composition of Ti although in a different high-temperature phase. The Pt_5Ti_3 phase is given by Okamoto (2009) [58] and may well be the phase referred to by Fernando *et al* [60] as a phase with a 16-atom unit cell which was not included in their study.

At 50-50% composition, there are three phases that have been reported [60, 64, 61] with the AuCd ($B19$) being a low temperature phase for PtTi and CsCl ($B2$) the high temperature phase when undergoing a martensitic transformation. A martensitic transformation

	% Ti	Space Group	Prototype	a_0	b_0	c_0	a_0	b_0	c_0
Pt	0	$Fm\bar{3}m$	Cu	3.984	a_0	a_0	3.92 [a]	-	-
Pt_8Ti	11.1	$I4/mmm$	V_4Zn_5	8.383	a_0	3.929	8.31		3.89 [b]
Pt_4Ti	20.0	$I4/m$	Ni_4Mo	6.265	a_0	3.947			
Pt_3Ti	25.0	$Pm\bar{3}m$	Cu_3Au	3.954	a_0	a_0	3.904 [c]	-	-
	25.0	$I4/mmm$	Al_3Ti	3.935	a_0	8.013			
	25.0	$Pm\bar{3}n$	Cr_3Si	5.054	a_0	a_0			
Pt_2Ti	33.3	$Immm$	$MoPt_2$	2.848	8.667	3.795			
	33.3	$Cmcm$	$ZrSi_2$	3.803	12.518	3.885			
	33.3	$Pnma$	Co_2Si	5.489	4.011	8.211			
	33.3	$I4/mmm$	$MoSi_2$	3.315	a_0	8.711			
Pt_5Ti_3	37.5	$Ibam$	-	5.481	11.036	8.201			
Pt_3Ti_2	40.0	$P\bar{3}m1$	Al_3Ni_2	4.302	a_0	5.399			
PtTi	50.0	$Pmma$	AuCd	4.620	2.798	4.875	4.59	2.76	4.84 [d]
	50.0	$P4/mmm$	CuAu	2.825	a_0	3.898	2.772	-	3.842 [e]
	50.0	$Pm\bar{3}m$	CsCl	3.180	a_0	a_0	3.192 [e]	-	-
	50.0	$Fm\bar{3}m$	NaCl	5.228	a_0	a_0			
	50.0	$F\bar{4}3m$	ZnS	5.717	a_0	a_0			
	50.0	$Cmcm$	CrB	2.869	10.082	4.467			
	50.0	$P4/nmm$	γCuTi	3.380	a_0	5.750			
Pt_4Ti_5	55.6	$I4/mmm$	V_4Zn_5	8.406	a_0	4.001			
$PtTi_2$	66.7	$I4/mmm$	$MoSi_2$	3.188	a_0	9.553			
$PtTi_3$	75.0	$Pm\bar{3}n$	Cr_3Si	5.055	a_0	a_0	5.03 [f]	-	-
	75.0	$Pm\bar{3}m$	Cu_3Au	4.035	a_0	a_0			
	75.0	$I4/mmm$	Al_3Ti	3.840	a_0	8.894			
Ti	100.0	$P6_3/mmc$	Mg	2.941	a_0	4.674	2.95	-	4.68 [a]

Table 3.1:
The crystal structure data for the Pt-Ti system. Experimental or other theoretical lattice constants are shown where available. [a]Reference [69], [b]Reference [158], [c]Reference [159], [d]Reference [64], [e]Reference [61], [f]Reference [160].

is a diffusionless transition, from one solid phase to another, which have been observed in metals as well as alloys [161]. This type of transformation can either be irreversible or reversible, as in the case of shape memory alloys (SMA) of which some Pt-based alloys are candidates [162]. The third structure at 50-50% composition is the CuAu ($L1_0$) structure. Equilibrium phase calculations are carried out for PtTi in the NaCl ($B1$) and zincblende ($B3$) structures as well.

As can be seen from Table 3.1, the calculated lattice constants for the expected equilibrium structures at each percentage composition are in agreement with experimental values (or the theoretical values in the case of the CuAu ($L1_0$) phase).

3.2 Heats of Formation

The heats of formation ΔH of compounds can be used to understand the stability of observed phases and to construct phase diagrams. Heats of formation may be calculated using the following equation [60]

$$\Delta H = E_{\mathrm{C}} - \sum_i x_i E_i, \tag{3.1}$$

where E_{C} is the total energy calculated for the compound, x_i is the concentration of element i which has total energy E_i in its bulk elemental phase. Equation 3.1 is used to calculate ΔH for the different phases of the Pt-Ti system.

The heats of formation for the Pt-Ti system are show in Figure 3.1. Increased binding (a higher magnitude of ΔH), and hence stability, is plotted downwards. The heats of formation show that for low temperatures phases of different composition can coexist. For instance, the $PtTi_3$ (Cr_3Si) phase is found to be stable to a mix of pure Ti and PtTi (AuCd) [60]. It can also be seen that the other equilibrium phases (Pt_3Ti, Pt_8Ti, Pt_2Ti) are also stable relative to other phases at different composition.

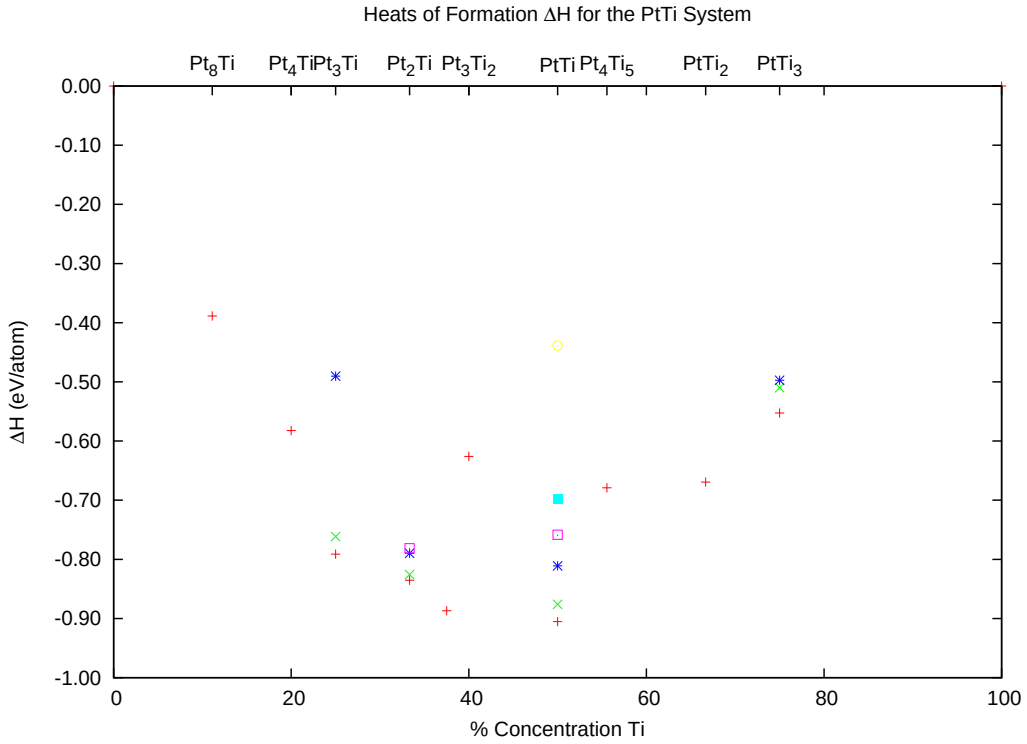

Figure 3.1:
The calculated heats of formation for the Pt-Ti system as a function of the atomic concentration of Ti, with increased binding plotted downwards.

3.3 50-50% Composition

The Pt-Ti system is like most other alloy systems in that the highest (magnitude) heats of formation occur at 50-50% concentration [59] (see Figure 3.1). Seven different structures were considered at this composition. The structures are listed in Table 3.1.

The PtTi phase with the highest (magnitude) heat of formation is the orthorhombic $B19$ phase (prototype AuCd), which is the low-temperature structure at this composition and which is stable for other Ti alloys, for example PdTi [60, 64]. A martensitic transformation leads to the high-temperature cubic $B2$ (CsCl) phase. Three other structures have heats of formation that lie in between the $B19$ and $B2$ structures: the orthorhombic $B33$ (prototype CrB) structure and the two tetragonal $L1_0$ CuAu and $B11$ γ-CuTi structures.

The two remaining structures are the cubic NaCl ($B1$) and zincblende ($B3$) phases which

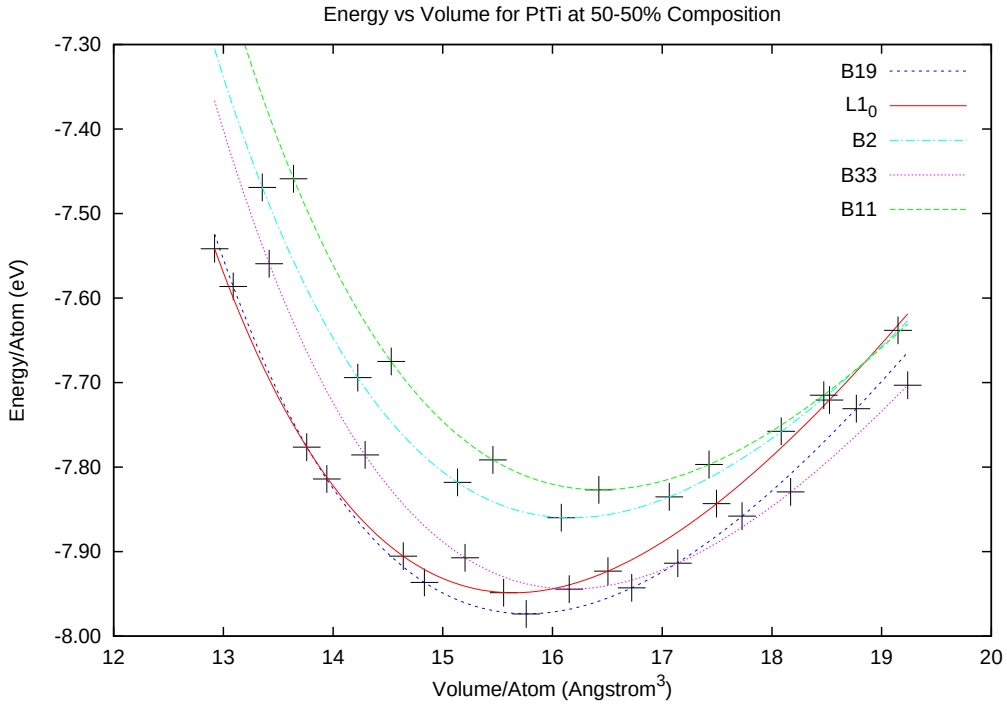

Figure 3.2:
Energy (per atom) versus volume (per atom) for the five phases of PtTi: $B19$ (prototype AuCd), $L1_0$ (prototype CuAu), $B2$ (prototype CsCl), $B33$ (prototype CrB) and $B11$ (prototype γCuTi).

are not studied in as much detail. Both phases are found to not be stable, with the $B3$ phase having a positive heat of formation.

Figure 3.2 shows the energy (per atom) versus volume (per atom) for the five most stable phases of PtTi: $B19$, $L1_0$, $B2$, $B11$ and $B33$. The energy-volume curves for $B1$ and $B3$ are not shown as their minimum energies are much higher when compared to the above five phases, while the equilibrium volumes are also larger.

From Figure 3.2, it can be seen that the most stable phase is $B19$, as it has the lowest minimum energy of the five phases. The phases are arranged from lowest minimum energy (and hence stability) as follows: $B19 < L1_0 < B33 < B2 < B11$. This was also shown by Ye *et al* [64] and Huang *et al* [61]. Using the heats of formation, the phases are ordered as $B19 < B33 < L1_0 < B11 < B2$. Fernando *et al* [60] also showed from heats of formation calculations that the low-temperature $B19$ phase shows greater binding than

the high-temperature $B2$ phase.

The energy-volume curves in Figure 3.2 show that the $L1_0$ phase is accessible from the low-temperature $B19$ under pressure. However, it is not possible to have a phase transition from $B19$ to $B2$ via pressure only. (The energy-volume curves of $B19$ and $B2$ only intersect at a higher volume, about 21.5 Å^3/atom, and at a higher energy of approximately -7.27 eV/atom. The curves do not intersect at lower volumes and one is unable to construct a common tangent to these curves.)

The energy band structures along high symmetry lines are shown in Figure 3.3. The band structures show that all the phases are metallic, as there are no band gaps present.

The total density of states (DOS) are shown in Figure 3.4, and the partial DOS are shown in Figures 3.5 (Ti site) and 3.6 (Pt site). The total DOS plots of Figure 3.4 reveal somewhat of a similarity between $B19$ and $B2$, while the remaining phases have a total DOS that is different to $B2$. The total DOS for the $B2$ shows that it is a BCC-like metal, with two sets of peaks separated by a small dip, [64]. The $B2$ peaks are narrower than the $B19$ since the latter is a structure with lower symmetry [64]. The total DOS is lower at the Fermi level E_{F} for $B19$ than it is for $B2$ ($B19$ is a four-atom unit cell structure while $B2$ has two atoms in its unit cell). The total DOS is also lower at E_{F} for the $L1_0$ and $B33$ phases.

The partial DOS (given in Figures 3.5 and 3.6) show that the d-bands dominate the band structure for all the phases being considered here. The Pt d-bands lie mainly below E_{F} and are mostly occupied while the Ti d-bands lie mainly above E_{F}[61]. The Ti s- and p-bands are broader than the d-bands, however they play a small role in the bonding, other than donating electrons to the d-bands. The gap that separates the lower energy Pt d-states from the higher energy Ti d-states becomes narrower when going from the $B2$ phase to the other four ($B19$, $B33$, $L1_0$ and $B11$) showing that there is a stronger binding between Pt and Ti [64].

The elastic constants for the various PtTi alloys are given in Table 3.2, including those

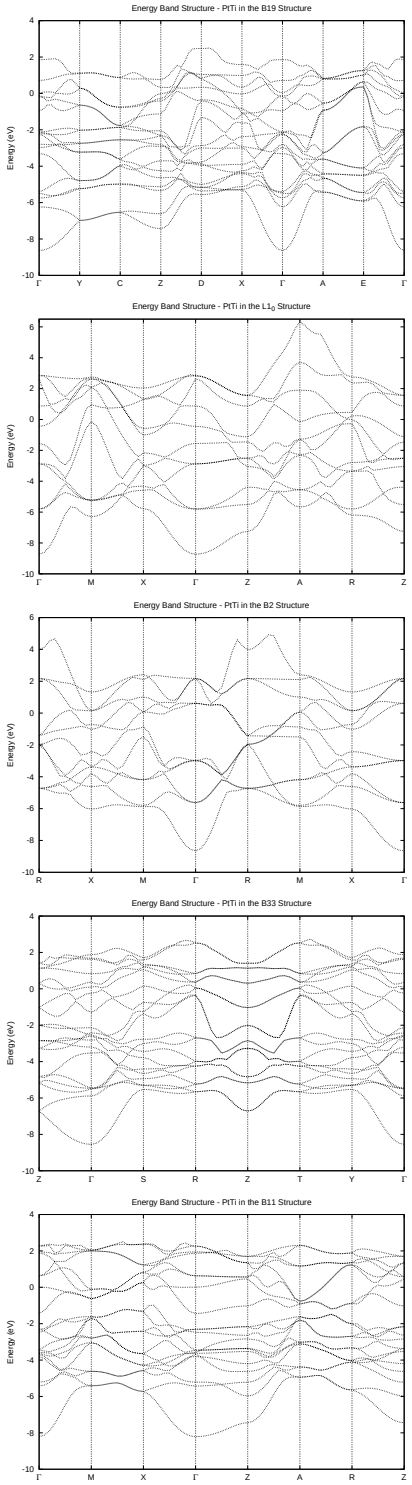

Figure 3.3:
The energy band structures along high symmetry lines for PtTi at 50-50% composition, from top to bottom: $B19$ (prototype AuCd), $L1_0$ (prototype CuAu), $B2$ (prototype CsCl), $B33$ (prototype CrB) and $B11$ (prototype γCuTi). The Fermi level E_{F} is set at 0 eV.

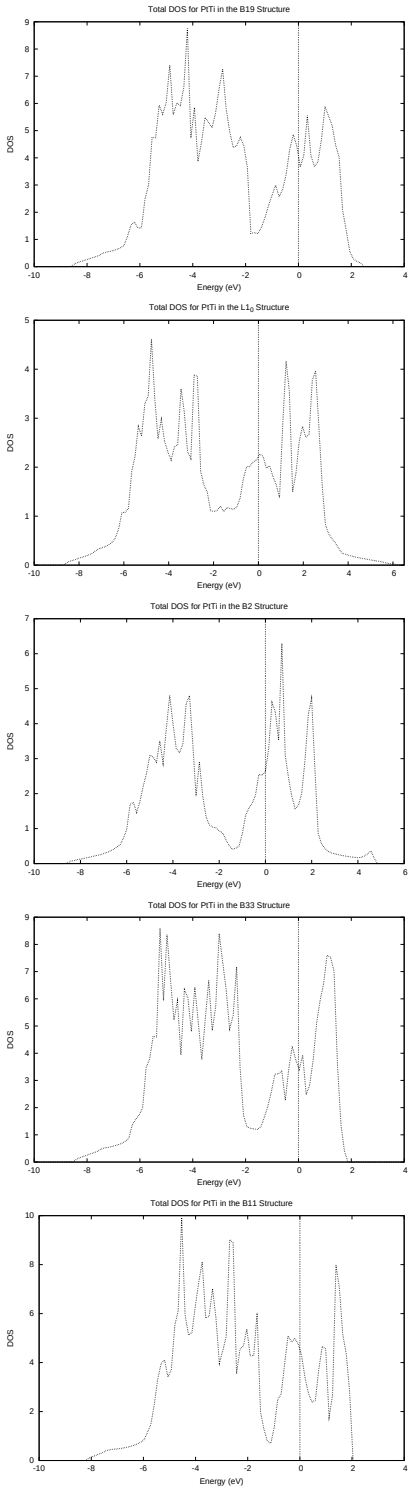

Figure 3.4:
The total density of states (DOS) PtTi at 50-50% composition, from top to bottom: $B19$, $L1_0$, $B2$, $B33$ and $B11$. E_{F} is set at 0 eV.

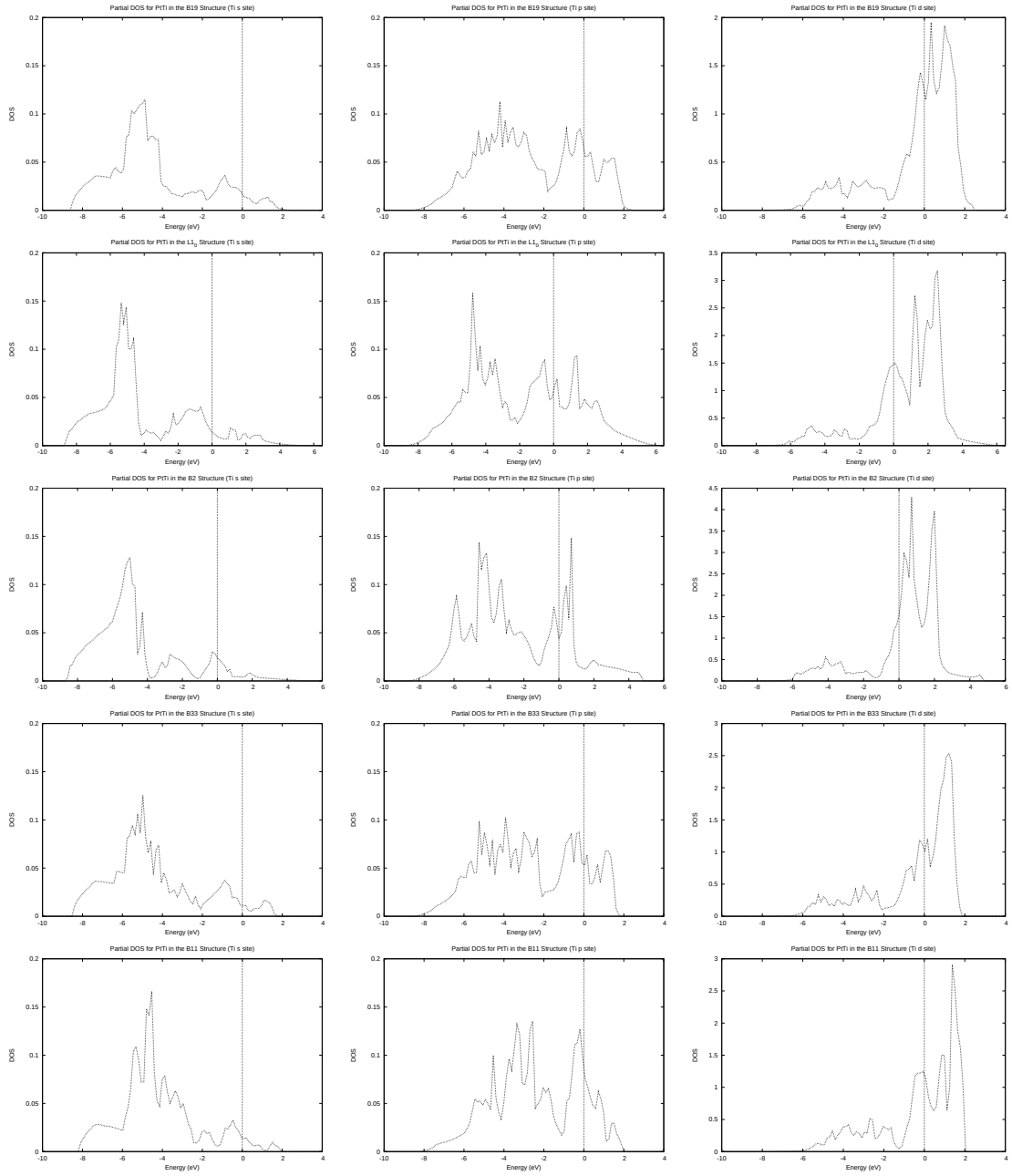

Figure 3.5:
Partial density of states for the Ti site at 50-50% composition. The left column is the partial density of states for the s states, the middle column the p states and the right column the d sites. The scale for the s and p sites is the same, but different for the d site. From top to bottom: $B19$, $L1_0$, $B2$, $B33$ and $B11$ structures. E_F is set at 0 eV.

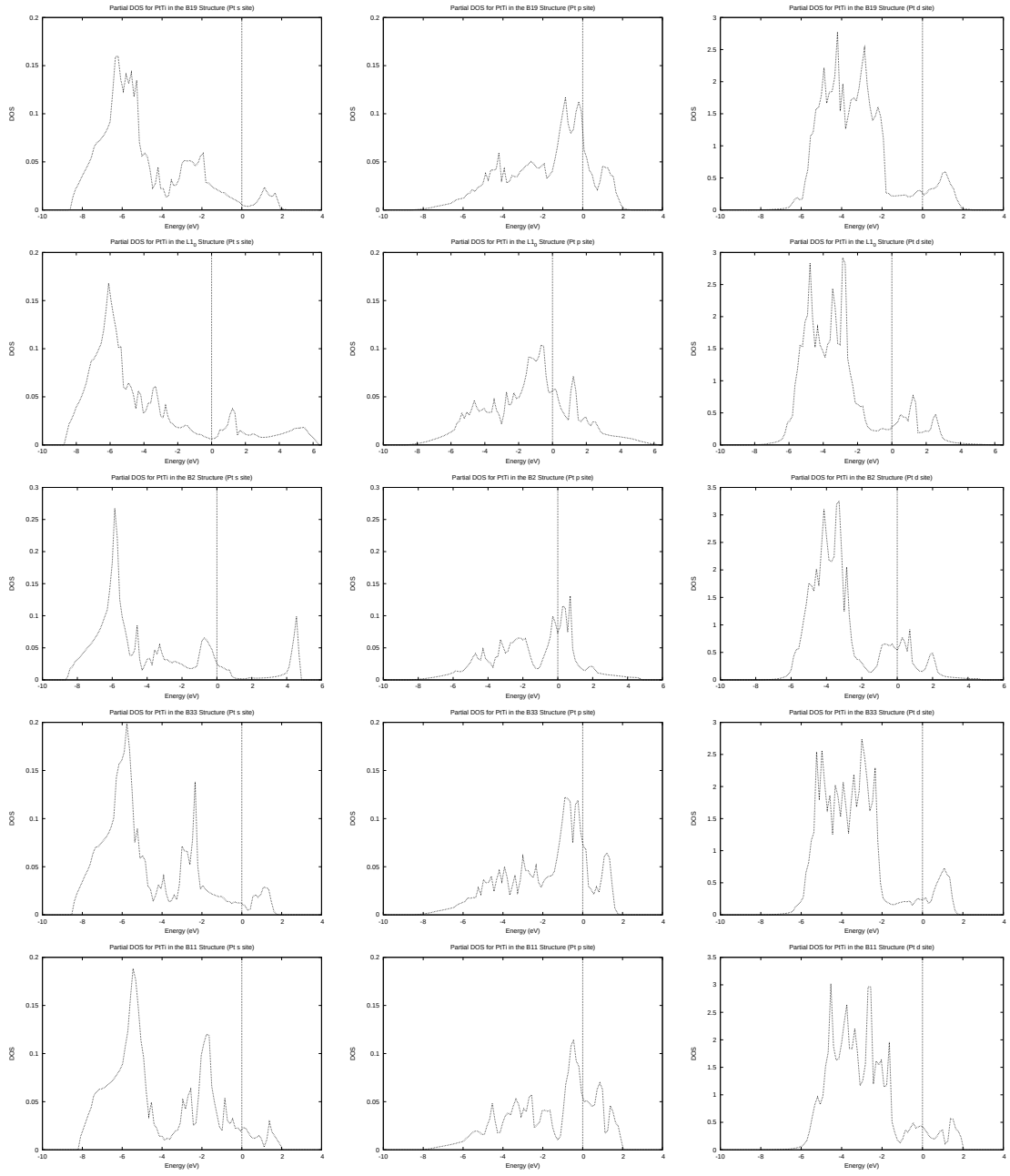

Figure 3.6:
Partial density of states for the Pt site at 50-50% composition. The left column is the partial density of states for the s states, the middle column the p states and the right column the d sites. The scale for the s and p sites is the same, but different for the d site. From top to bottom: $B19$, $L1_0$, $B2$, $B33$ and $B11$ structures. E_F is set at 0 eV.

	C_{11}	C_{12}	C_{13}	C_{22}	C_{23}	C_{33}	C_{44}	C_{55}	C_{66}
$B19$	311.3	124.6	142.5	344.8	106.1	310.0	46.9	59.1	65.0
$L1_0$	317.6	113.6	144.3			336.9	98.3		35.1
$B2$	171.4	192.2					32.7		
$B11$	194.6	157.9	135.3			250.6	71.7		105.9
$B33$	232.0	106.0	157.2	318.8	142.8	308.8	73.9	91.6	24.8
$B1$	259.8	92.4					2.2		
$B3$	93.1	101.9					-21.0		

Table 3.2:
The elastic constants for PtTi alloys at the 50-50% composition. All elastic constant values are in GPa. The $B1$ and $B3$ phases have also been included here.

for $B1$ and $B3$. For a cubic material to be mechanically stable, the elastic constants have to obey certain restrictions [154], two of which are

$$C_{11} - C_{12} > 0, \tag{3.2}$$

$$C_{44} > 0. \tag{3.3}$$

Table 3.2 shows that, for $B2$ and $B3$, $C_{11} < C_{12}$. For $B3$, $C_{44} < 0$. These two phases then are mechanically unstable. For both phases, the shear modulus is also negative.

Tetragonal crystals also have conditions required for mechanical stability. Equation 3.2 must also hold for a tetragonal crystal. An additional requirement is [12]

$$C_{11} + C_{33} - 2C_{13} > 0. \tag{3.4}$$

The elastic constants for the tetragonal $B11$ therefore hold, indicating the crystal to be mechanically stable. For an orthorhombic crystal, three of the various mechanical stability restrictions are [12]

$$C_{11} + C_{22} - 2C_{12} > 0, \tag{3.5}$$

$$C_{22} + C_{33} - 2C_{23} > 0, \tag{3.6}$$

and the third is Equation 3.4. Equations 3.4, 3.5 and 3.6 (as well as the remaining restrictions by Mattesini and Matar [12]) hold for $B19$ and $B33$, indicating that they are

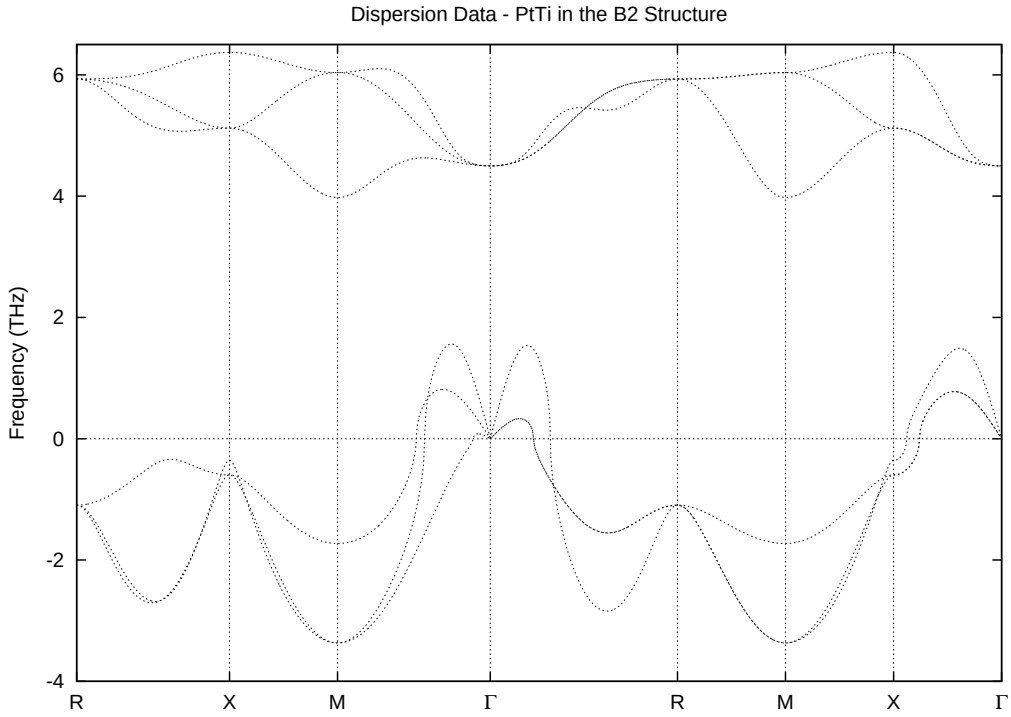

Figure 3.7:
The phonon dispersion for PtTi $B2$ along high symmetry lines. Imaginary frequencies are plotted as negative values.

mechanically stable.

For the 50-50% composition, the only two structures that are not stable due to elastic constant restrictions for mechanical stability, are the $B2$ and the $B3$ phases.

Huang *et al* showed that the $B2$ phase is statically unstable due to negative elastic moduli [61]. The phonon dispersion along the same high symmetry lines as for the energy band calculations, is shown in Figure 3.7, which is in agreement with the work of Huang *et al*. The unstable modes could be related to (molecular dynamics/neutron scattering) soft modes at a high temperature. Stable modes can also change as a function of temperature, due to anharmonic effects. The high-temperature $B2$ phase is stabilized dynamically by anharmonic phonons [61].

Phonon dispersion relations for the $B3$ phase also show unstable modes with negative

	Bulk Modulus	Shear Modulus	Young's Modulus	Poisson's Ratio	
	B	G	Y	ν	$R_{G/B}$
$B19$	190.3	73.7	195.9	0.33	0.39
$L1_0$	197.4	84.4	221.5	0.31	0.43
$B2$	185.2	15.5	45.2	0.46	0.08
$B11$	166.3	63.9	170.0	0.33	0.38
$B33$	185.7	68.3	182.5	0.34	0.37
$B1$	148.2	34.8	96.9	0.39	0.23
$B3$	98.9	-14.3	-45.1	0.58	-0.14

Table 3.3:
Elastic moduli for PtTi alloys at the 50-50% composition. The elastic moduli given here are the Voight moduli and the units are in GPa, except for the Poisson ratio ν and the ratio $R_{G/B}$ which are unitless.

frequencies. The fact that $B3$ also has a negative elastic constant (C_{44}) which leads to a negative shear modulus, as well as a positive heat of formation, it can be concluded that this phase is unstable.

The elastic moduli are given in Table 3.3. The $L1_0$ phase has the highest bulk modulus, shear modulus and Young's modulus out of all of the 50-50% composition phases, followed by the low-temperature $B19$ and then the $B33$ phase. $B2$ has the next highest bulk modulus, however both its shear and Young's moduli are lower than all but the $B3$ phase. All of the alloy phases have a bulk modulus that is lower than the bulk modulus for FCC Pt, showing a decrease in the bulk modulus when alloying Pt with Ti.

Chen *et al* [50] showed that it is possible to study the ductile/brittle properties of a metal using the simple shear to bulk modulus ratio, $R_{G/B}$. The ratio $R_{G/B}$ is also given in Table 3.3 for each of the phases. For a $R_{G/B}$ value less than 0.5, the metal is ductile, otherwise it is brittle in nature. Both FCC Pt and HCP Ti are ductile, as they have $R_{G/B}$ values of 0.27 and 0.38 respectively.

Table 3.3 shows that $R_{G/B}$ is less than 0.5 for all of the phases. Ignoring the $B3$ phase,

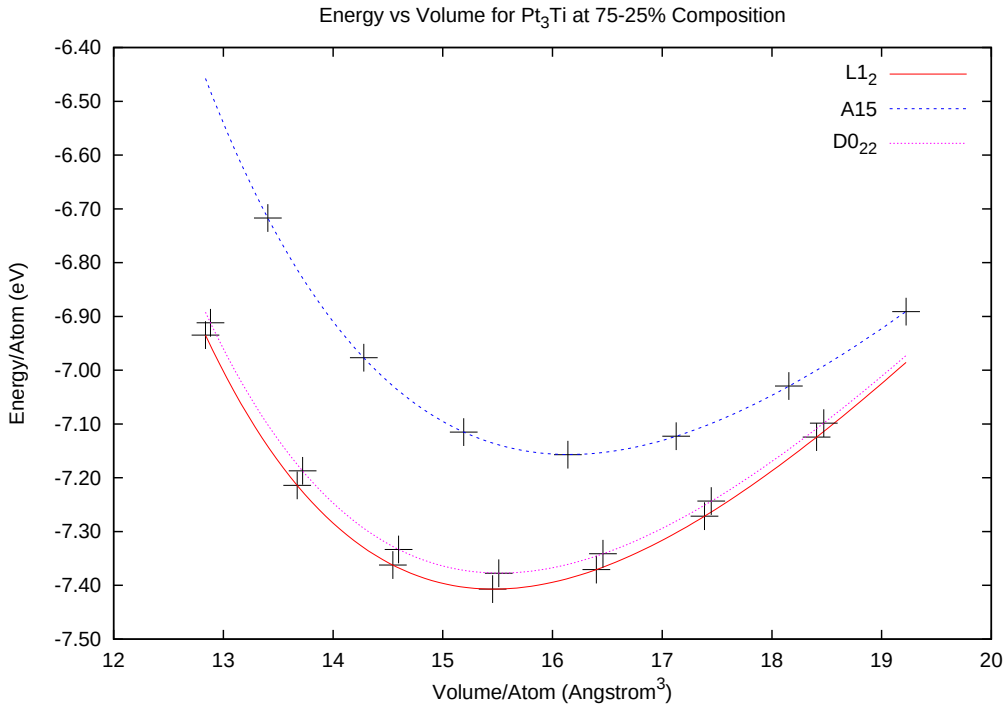

Figure 3.8:
Energy (per atom) versus volume (per atom) for the three phases of Pt_3Ti: $L1_2$ (prototype Cu_3Au), $A15$ (prototype Cr_3Si) and $D0_{22}$ (prototype Al_3Ti).

$B2$ is the most ductile, while $B19$ is the least ductile of the phases. Therefore, alloying of Pt with Ti at this concentration still preserves the ductile nature of the metals.

3.4 75-25% Composition

Three structures were considered for the 75%-25% concentration. The equilibrium structure for Pt_3Ti is the Cu_3Au $L1_2$, with an equilibrium lattice constant a_0 that is very close to bulk Pt [63]: the calculated values are 3.984 Å for Pt in FCC and 3.954 Å for Pt_3Ti $L1_2$ (see Table 3.1).

Pt_3Ti has also been reported in the disordered $D0_{22}$ phase, with prototype Al_3Ti [73]. A third phase was considered, the cubic $A15$ (prototype Cr_3Si) which is the equilibrium phase for $PtTi_3$ to see if this could be a competing structure at 75% Pt composition. The energy-volume curves for the three phases is shown in Figure 3.8.

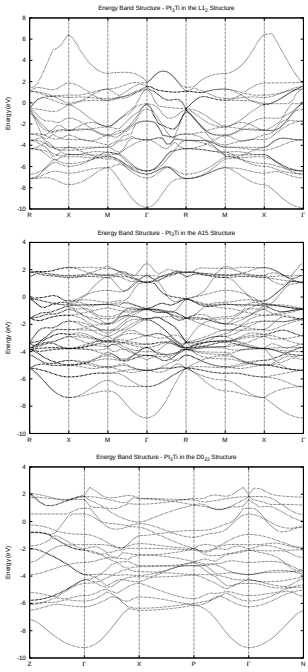

Figure 3.9:
The energy band structure for PtTi at 75-25% composition, from top to bottom: $L1_2$, $A15$ and $D0_{22}$. E_{F} is set at 0 eV.

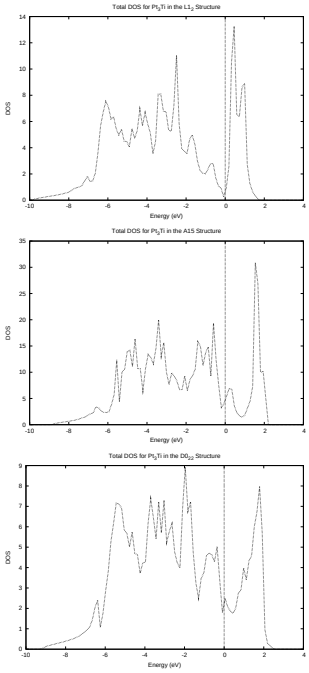

Figure 3.10:
The total DOS for PtTi at 75-25% composition, from top to bottom: $L1_2$, $A15$ and $D0_{22}$. E_{F} set at 0 eV.

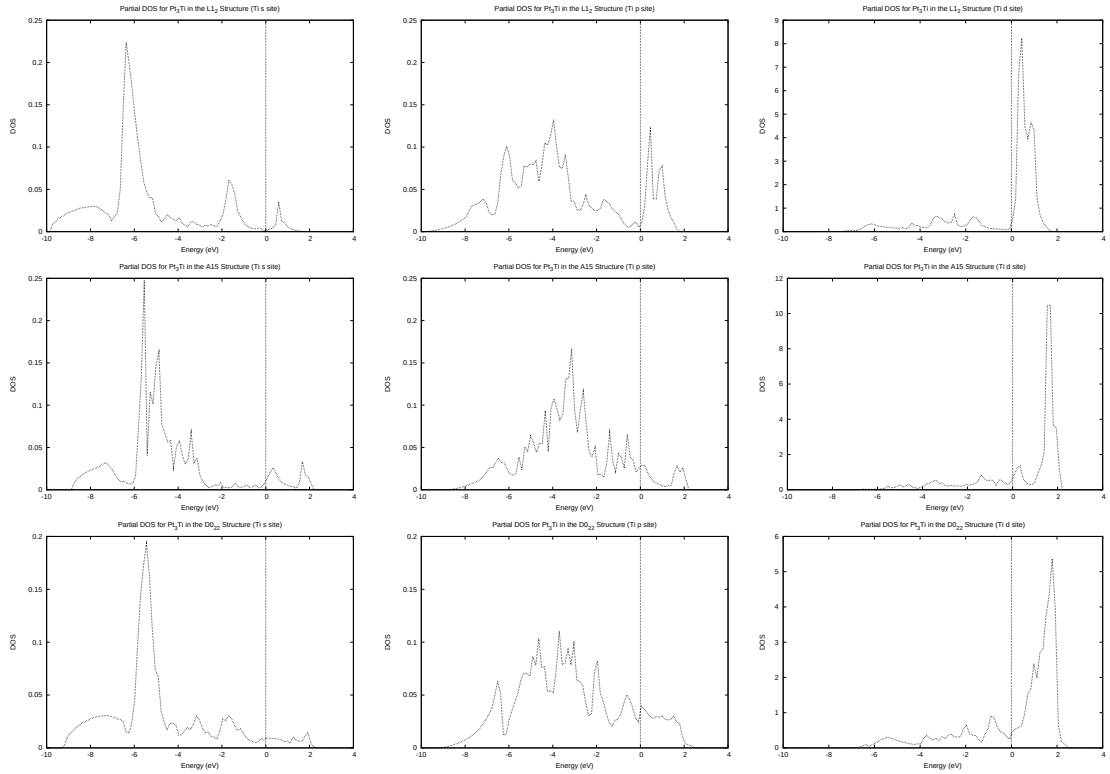

Figure 3.11:
Partial density of states for the Ti site at 75-25% composition. The left column is the partial density of states for the s states, the middle column the p states and the right column the d sites. The scale for the s and p sites is the same, but different for the d site. From top to bottom: $L1_2$, $A15$, $D0_{22}$ structures.

Figure 3.8 shows that the $A15$ phase is inaccessible from the equilibrium $L1_2$ via pressure only. The $D0_{22}$ phase is formed by first melting pure Pt and pure Ti, then quenching the alloy from 1100°C and annealing in a vacuum for short time periods at 900°C [73]. Pt_3Ti in the $A15$ phase has not been reported in the literature. While the elastic constants and moduli point to stability of the structure, it has a much lower heat of formation compared to both $L1_2$ and $D0_{22}$ (see Figure 3.1).

The energy band structure for Pt_3Ti (shown in Figure 3.9) in the $L1_2$ phase is in agreement with the LAPW electronic structure calculations of Chen *et al* [63]. It can be seen that more bands form when alloying Pt with Ti, compared to the band structure of bulk FCC Pt (not shown). There are also more bands in the $A15$ and $D0_{22}$ phases. All three phases continue to show metallic behaviour as no gap between the conduction and valence

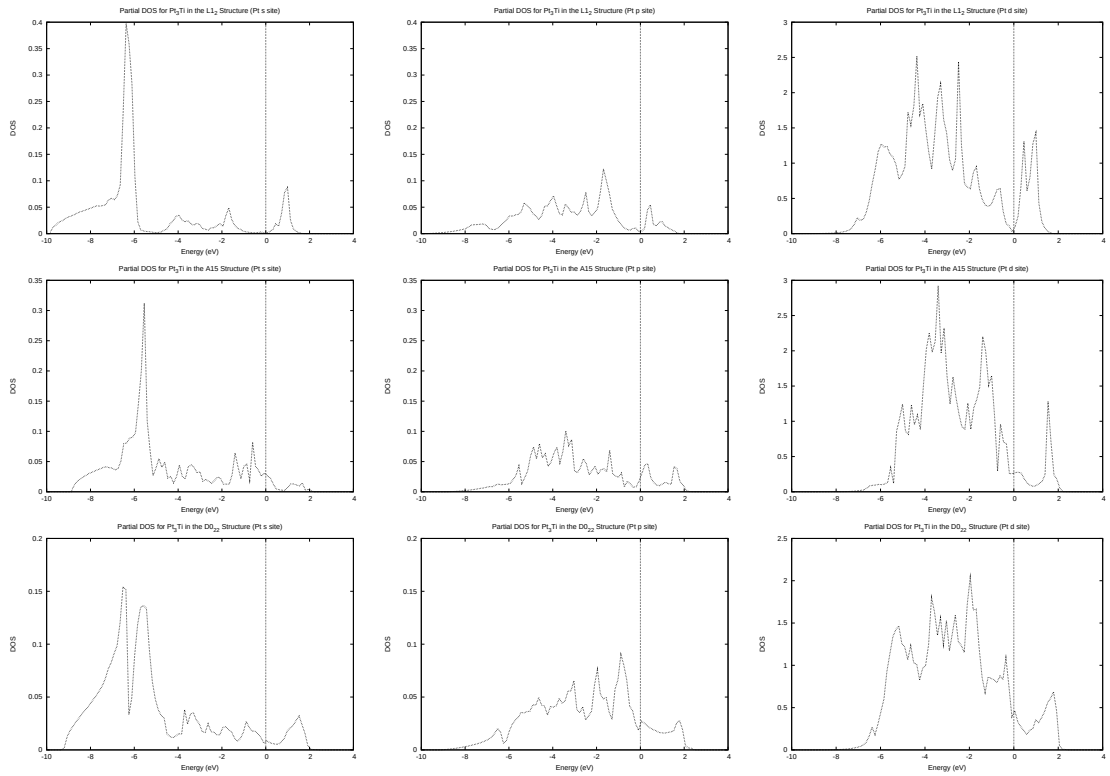

Figure 3.12:
Partial density of states for the Pt site at 75-25% composition. The left column is the partial density of states for the s states, the middle column the p states and the right column the d sites. The scale for the s and p sites is the same, but different for the d site. From top to bottom: $L1_2$, $A15$, $D0_{22}$ structures.

bands occur. The width of the conduction band is largest for the $L1_2$ phase.

The total and partial DOS for Pt_3Ti are shown in Figures 3.10, 3.11 and 3.12. Once more, it can be seen that the d-states dominate for the three phases, with the Pt d-states mainly lying below the Fermi level and the Ti d-states lying above the Fermi level. Ti site valence electrons are partly transferred to the Pt site [63].

The total DOS plots show a distinct electronic structure for the three Pt_3Ti alloys compared to the pure metal, due to the high level of hybridization [63]. The Fermi level for the $L1_2$ phase is located very close to a minimum in the DOS plot, indicating a structure that has a high heat of formation and one that is very stable. The heat of formation for the $L1_2$ phase is among the highest of the various Pt-Ti alloy structures. The Fermi levels for $A15$ and $D0_{22}$ are also located close to minima in a rising part of their respective

	C_{11}	C_{12}	C_{13}	C_{33}	C_{44}	C_{66}
$L1_2$	338.1	178.8			131.1	
$A15$	387.1	119.7			13.6	
$D0_{22}$	315.5	192.9	177.5	333.2	123.2	145.4

Table 3.4:
The elastic constants for Pt_3Ti alloys. All elastic constant values are in GPa.

total DOS plots. Thus, these two structures should also exhibit good stability. The $D0_{22}$ structure does have a high heat of formation, comparable to $L1_2$. The heat of formation for $A15$, however, is much lower.

The elastic constants for Pt_3Ti $L1_2$, $A15$ and $D0_{22}$ are given in Table 3.4. For mechanical stability, Equations 3.2 and 3.4 must hold. Table 3.4 shows that the requirements are met, giving three stable phases at this concentration.

Table 3.5 gives the elastic moduli for the 75-25% concentration. The bulk modulus for each phase is closer to the bulk modulus of FCC Pt. The bulk modulus is larger than the phases at 50-50% composition. The three phases each have a higher shear modulus than FCC Pt, while only $A15$ has a lower Young's modulus. All three phases are also ductile in nature, having an $R_{G/B}$ of less than 0.5. $L1_2$, however, has an $R_{G/B}$ value of 0.48, very close to being a brittle material.

3.5 25-75% Composition

The three structures that were considered for the 75% Pt concentration were also investigated for the 25-75% concentration. The $A15$ structure is the equilibrium structure for $PtTi_3$ [160], with a lattice constant that is larger than bulk Pt. The bigger lattice constant in $A15$ is due to it having an eight-atom unit cell. The calculated lattice constant for $A15$ is in good agreement with experimental values. The $L1_2$ phase has a lattice constant which is similar to Pt in FCC and Pt_3Ti $L1_2$. The $D0_{22}$ phase has lattice constants that are similar to those of Pt_3Ti $D0_{22}$ (see Table 3.1).

	Bulk Modulus	Shear Modulus	Young's Modulus	Poisson's Ratio	
	B	G	Y	ν	$R_{G/B}$
$L1_2$	231.9	110.5	286.1	0.29	0.48
$A15$	208.8	106.1	168.3	0.37	0.38
$D0_{22}$	228.9	68.3	275.8	0.30	0.30

Table 3.5:
Elastic moduli for Pt_3Ti alloys The elastic moduli given here are the Voight moduli and the units are in GPa, except for the Poisson ratio ν and the ratio $R_{G/B}$ which are unitless.

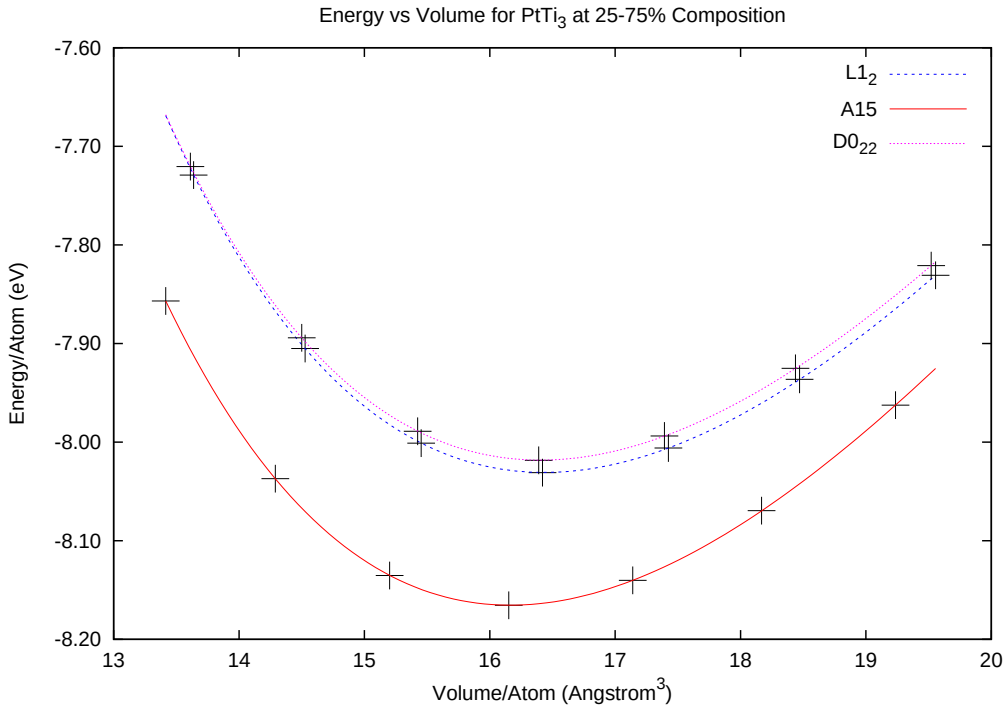

Figure 3.13:
Energy (per atom) versus volume (per atom) for the three phases of $PtTi_3$: $L1_2$, $A15$ and $D0_{22}$.

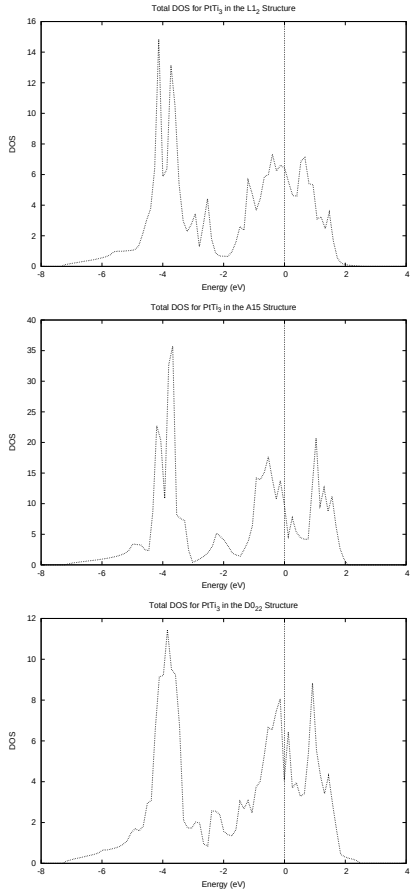

Figure 3.14:
The total DOS for PtTi at 25-75% composition, from top to bottom: $L1_2$, $A15$, and $D0_{22}$. E_F set at 0 eV.

The heats of formation for $PtTi_3$ show that the $A15$ phase has the highest binding of the three structures, and the energy-volume curve (Figure 3.13) also show that this is the most stable structure. As before, applying pressure on the equilibrium $A15$ will not result in accessing the $D0_{22}$ and $L1_2$ phases.

The total DOS (shown in Figure 3.14 at this concentration are different to the Pt_3Ti phases, as well as the PtTi phases, in that the Fermi level is not located near the gap that divides the lower energy Pt state peaks from the higher energy Ti peaks. The partial DOS (Figure 3.15 for the Ti site and Figure 3.16 for the Pt site) shows that while the Pt d-states lie below the Fermi level, the Ti d-states lie above the Fermi level with a significant contribution to the DOS about 1 eV below the Fermi level. Hence the Fermi level is

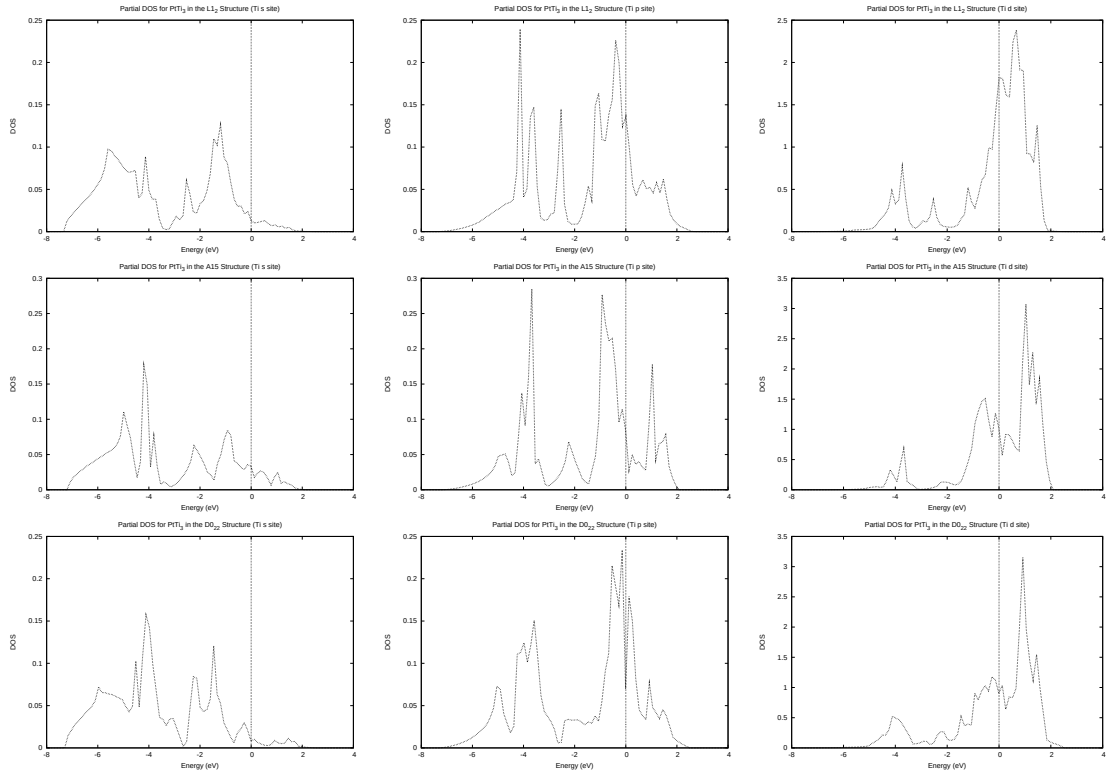

Figure 3.15:
Partial density of states for the Ti site at 25-75% composition. The left column is the partial density of states for the s states, the middle column the p states and the right column the d sites. The scale for the s and p sites is the same, but different for the d site. From top to bottom: $L1_2$, $A15$, $D0_{22}$ structures.

located within the higher energy peaks. This is seen in the three $PtTi_3$ phases (perhaps due to the higher concentration of Ti atoms in these phases?)

The partial DOS also shows that the Pt d-state peaks are much narrower than the corresponding Pt peaks at 75% Pt concentration (see Figure 3.12). The Ti d-state peaks, which were very narrow at 75% Pt concentration (Figure 3.11), are now wider at 25% Pt concentration.

The Fermi level is located near a minima (on a decreasing part) in the total DOS for the $A15$ phase, while it is located at a minima for the $D0_{22}$ phase and at a maxima for the $L1_2$ phase. The $A15$ and $D0_{22}$ phases should exhibit good stability, especially compared to $L1_2$; their heats of formation are similar to those of alloys studied at less than 50% Pt concentration.

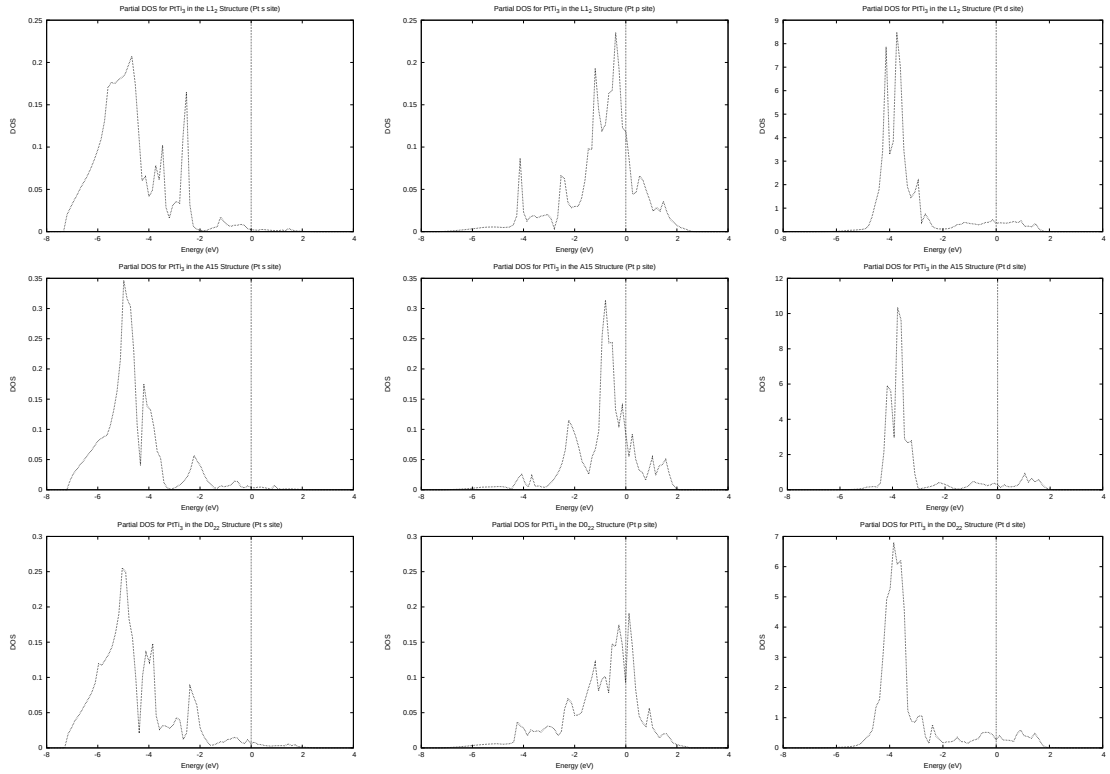

Figure 3.16:
Partial density of states for the Pt site at 25-75% composition. The left column is the partial density of states for the s states, the middle column the p states and the right column the d sites. The scale for the s and p sites is the same, but different for the d site. From top to bottom: $L1_2$, $A15$, $D0_{22}$ structures.

At this composition, the two cubic phases are found to be mechanically stable, as the elastic constants hold the requirements for stability (Equations 3.2 and 3.4). The $D0_{22}$ phase, however, is not mechanically stable, as $C_{11} = 137.3$ GPa $< C_{12} = 184.6$ GPa.

The bulk moduli for the three phases ($L1_2$: $B = 147.9$ GPa, $A15$: $B = 153.0$ GPa and $D0_{22}$: $B = 146.1$ GPa) are lower than the 50-50% and 75-25% compositions. Again, the three alloys behave in a ductile manner, as the $R_{G/B}$ ratios for each is less than 0.5.

3.6 66.7-33.3% Composition

Figure 3.17 shows the energy-volume curves for the four phases considered for this concentration. Two structures were considered from Watson *et al* [59] as phases involving

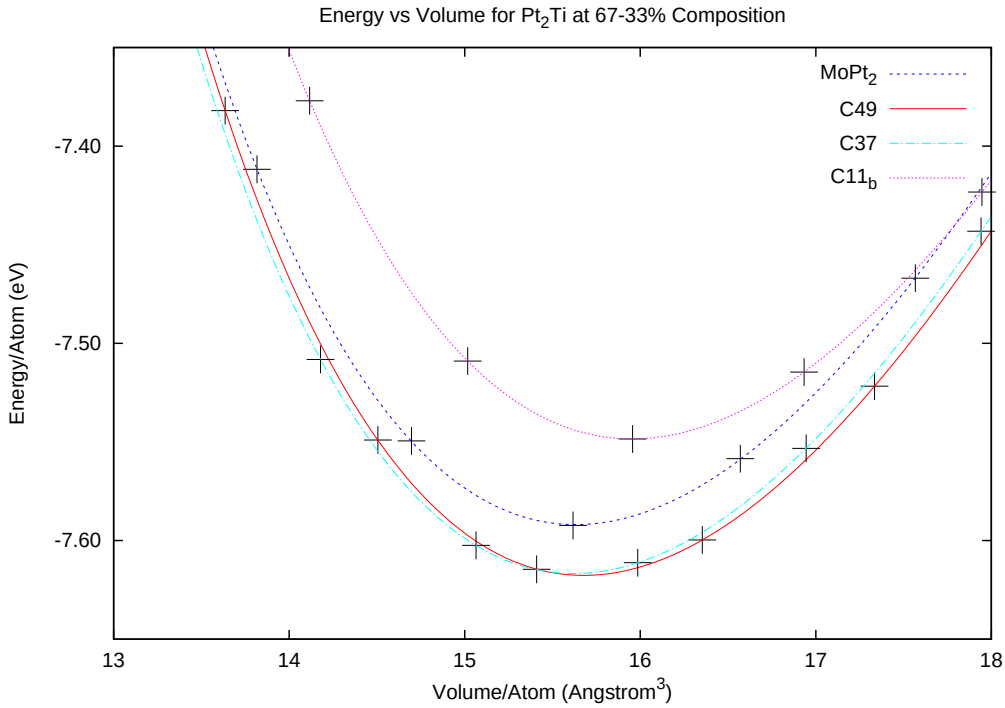

Figure 3.17:
Energy (per atom) versus volume (per atom) for the four phases of Pt_2Ti: $C37$ (prototype Co_2Si), $C49$ ($ZrSi_2$), $MoPt_2$ and $C11_b$ (prototype Mo_2Si).

Pt with a 66.7% concentraton. These are the body centred orthorhombic $MoPt_2$ phase and the body centred tetragonal $MoSi_2$ $C11_b$ phase. The other two are from Curtarolo *et al* [71] which are described as two-phase region above 900°C. These two phases are the orthorhombics $C37$ (prototype Co_2Si) and $C49$ (prototype $ZrSi_2$).

The two high-temperature phases ($C37$ and $C49$) are competing phases, while the $MoPt_2$ phase could be obtained via pressure. The $C11_b$ phase is inaccessible via pressure only. The $C49$ phase, which has the minimum equilibrium energy, also has the largest heat of formation energy.

The energy band structures for the Pt_2Ti phases are shown in Figure 3.18, indicating the metallic nature of all the phases with there being no band gaps present. The high-temperature $C37$ and $C49$ phases have many more energy bands than the other two phases. The width of the conduction bands for $C37$ and $C49$ is also larger.

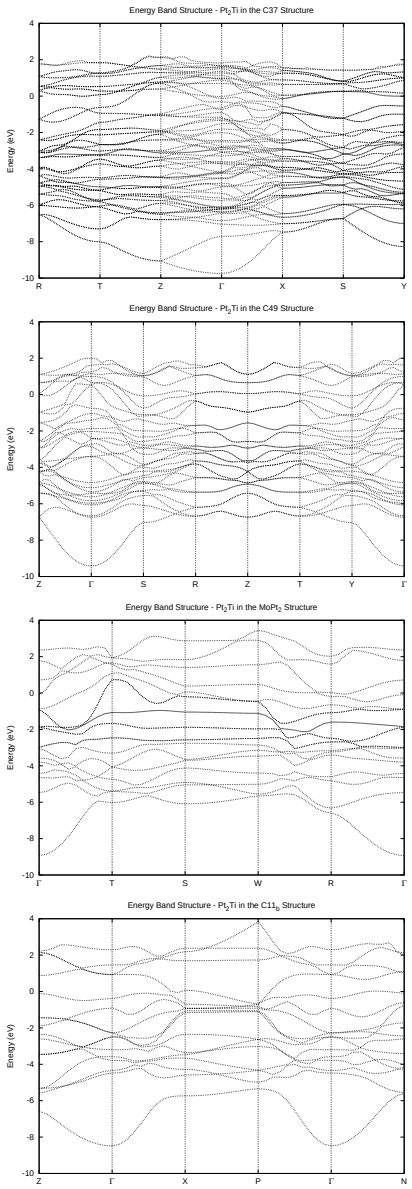

Figure 3.18:
The energy band structure for PtTi at 67-33% composition, from top to bottom: $C37$, $C49$, $MoPt_2$ and $C11_b$. E_F is set at 0 eV.

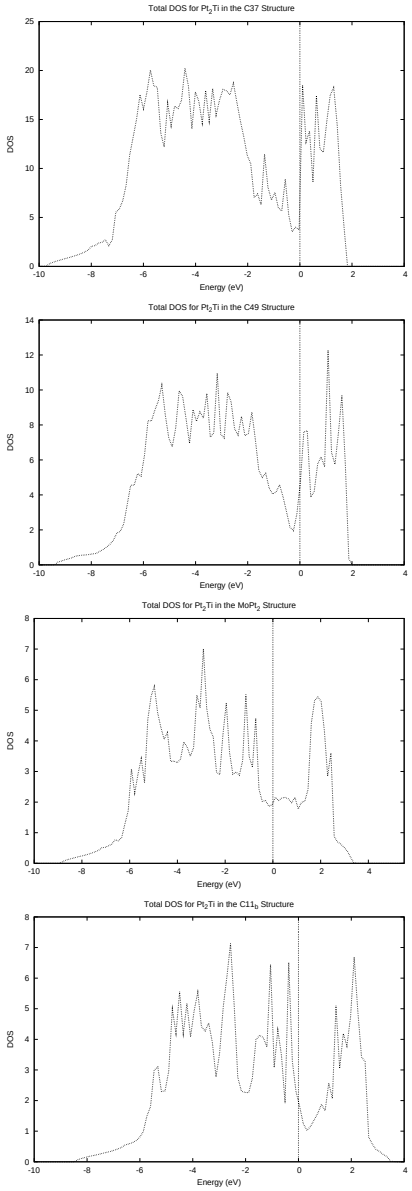

Figure 3.19:
Total DOS for PtTi at 67-33% composition, from top to bottom: $C37$, $C49$, $MoPt_2$ and $C11_b$. E_F is set at 0 eV.

The total DOS (Figure 3.19) show that the Fermi level lies in a dip separating two sets of peaks. The lower-energy peaks are once again due to the Pt d-states, which lie mostly below the Fermi level. There are significant contributions from these d-states above the Fermi level (see Figure 3.21). The Ti d-states form narrow peaks that are mostly found above the Fermi level (see Figure 3.20). The Fermi level lies at a minima for $C37$ and very

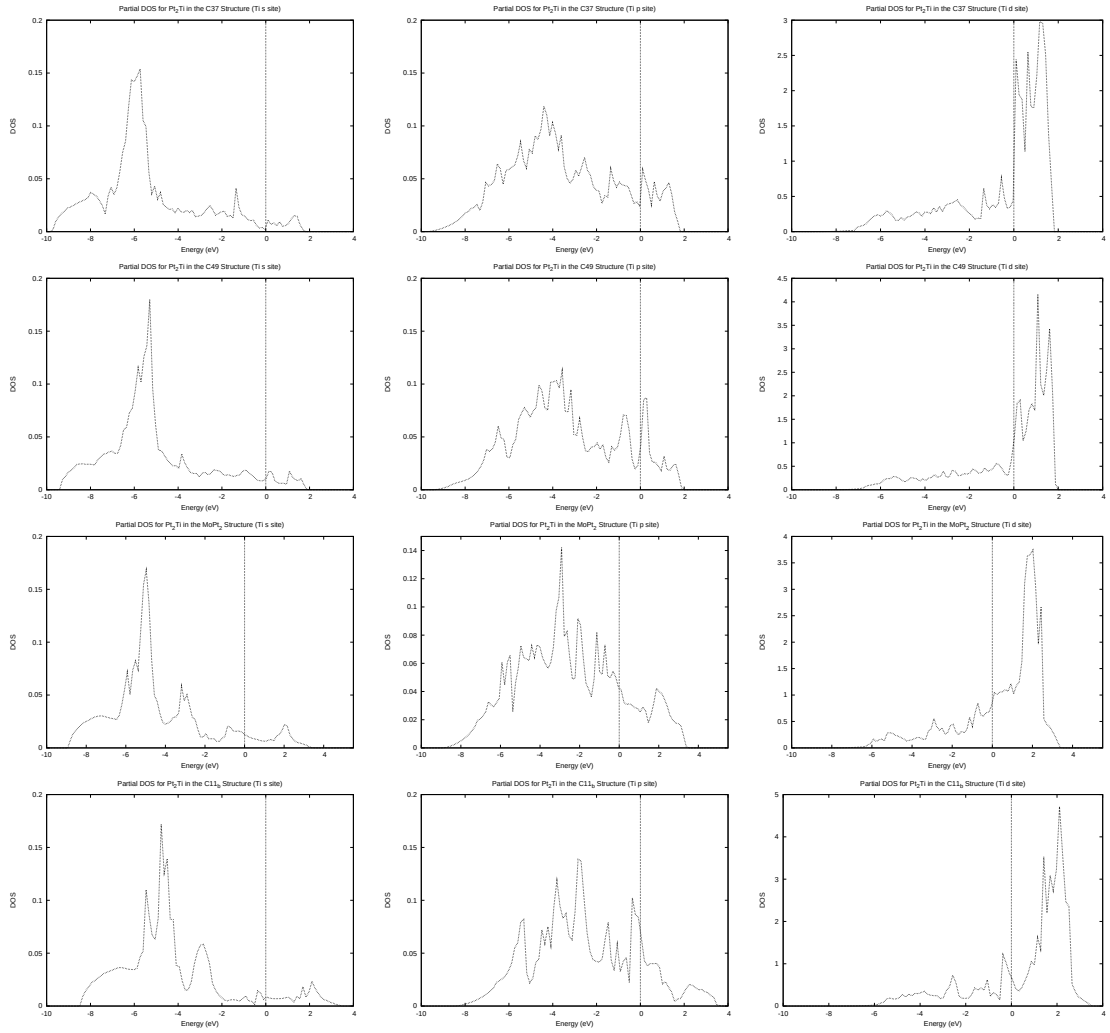

Figure 3.20:
Partial DOS for PtTi (Ti site) at 67-33% composition, from top to bottom: $C37$, $C49$, $MoPt_2$ and $C11_b$. E_F is set at 0 eV.

close to a minima for $C49$, on a rising part of the DOS. The Fermi level is also very close to a minima for $MoPt_2$. It is on a decreasing part of the DOS for $C11_b$, approaching a minima. All the structures have high heats of formation. The phases are arranged from highest to lowest binding as $C49$, $MoPt_2$, $C37$ and $C11_b$.

Table 3.6 gives the elastic constants for the PtTi phases at 67-33% composition. For the phases to be stable, the elastic constants are subject to the restrictions, which for orthorhombic crystals, are given by Equations 3.4, 3.5 and 3.6, namely

$$C_{11} + C_{33} - 2C_{13} > 0,$$

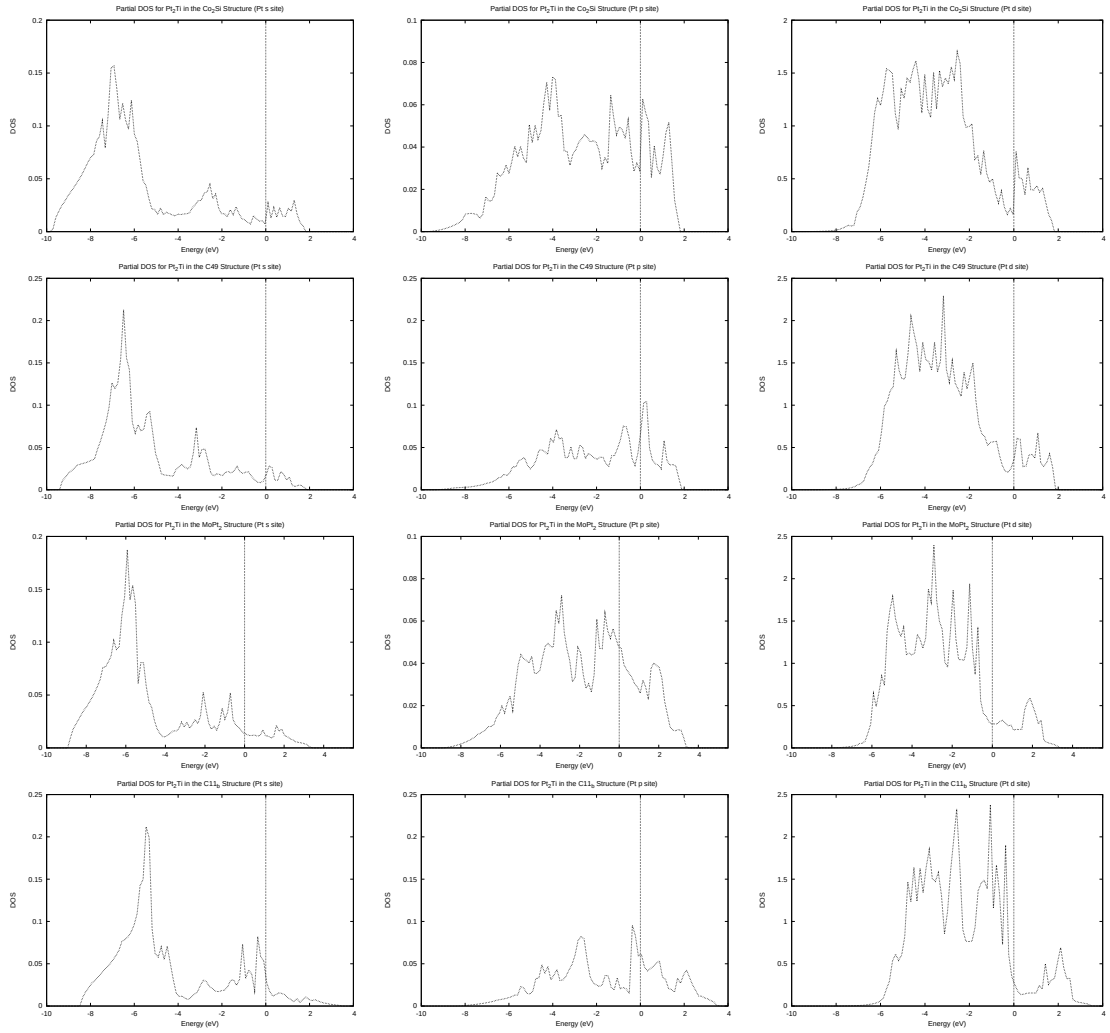

Figure 3.21:
Partial DOS for PtTi (Pt site) at 67-33% composition, from top to bottom: $C37$, $C49$, $MoPt_2$ and $C11_b$. E_F is set at 0 eV.

$$C_{11} + C_{22} - 2C_{12} > 0,$$

$$C_{22} + C_{33} - 2C_{23} > 0.$$

For the three orthorhombic phases, the relations hold, thereby confirming the stabilities of these phases. The stability of the tetragonal $C11_b$ phase is subject to the restrictions given by Equations 3.2 and 3.4. While Equation 3.4 is satisfied, it is the first restriction (Equation 3.2) where the crystal was found to not be mechanically stable, as $C_{11} < C_{12}$ for $C11_b$.

	C_{11}	C_{12}	C_{13}	C_{22}	C_{23}	C_{33}	C_{44}	C_{55}	C_{66}
$C37$	412.1	200.7	141.4	224.4	205.2	426.1	115.3	64.7	122.6
$C49$	307.1	166.4	223.7	285.6	163.7	316.2	103.0	154.1	99.6
$MoPt_2$	303.9	125.3	185.0	309.7	192.0	297.4	121.5	116.5	61.5
$C11_b$	199.7	227.5	170.1			268.1	81,2		112.7

Table 3.6:
The elastic constants for PtTi alloys at the 67-33% composition. All elastic constant values are in GPa.

The elastic moduli (Table 3.7) show that the bulk modulus for the $C49$ and $MoPt_2$ phases approaches that of bulk Pt. The bulk modulus of $C37$ is greater than that of FCC Pt (241.0 GPa), this being one of a small number of alloys that has a higher bulk modulus than the pure metal. The shear and Young's moduli for all the phases except $C11_b$ are larger than FCC Pt.

The calculated Reuss shear and Young's modulus and the Hill shear and Young's modulus for the $C11_b$ are negative (not shown). This is further evidence of the phase being unstable.

All of the phases at this compositon are ductile. The $R_{G/B}$ ratio is less than 0.5. However, for $C37$, $C49$ and $MoPt_2$ the ratio is above 0.4 approaching brittle behaviour (both FCC Pt and HCP Ti have $R_{G/B}$ ratios that are less than 0.4).

3.7 Other Compositions

The remaining structures in the Pt-Ti alloy system are as follows. The body centred tetragonal Pt_8Ti (with prototype V_4Zn_5) is an 18-atom unit structure. The Ni_4Mo phase is also a body centred tetragonal structure reported by Schryvers and Amelinckx [73]. The body centred orthorhombic Pt_5Ti_3 is a 24-atom unit cell that is part of the space group *Ibam*. It doesn't, however, have a Strukturbericht designation or a prototype structure [58]. This phase does have a high heat of formation, comparable to some of the phases at 50-50% composition. The hexagonal Pt_3Ti_2 and orthorhombic Pt_4Ti_5 (which was derived from the tetragonal Pt_8Ti by changing four Pt atoms for Ti ones) have small heats of

	Bulk Modulus	Shear Modulus	Young's Modulus	Poisson's Ratio	
	B	G	Y	ν	$R_{G/B}$
$C37$	251.9	102.2	270.1	0.32	0.41
$C49$	224.1	95.0	249.7	0.31	0.42
$MoPt_2$	212.8	87.2	230.1	0.32	0.41
$C11_b$	200.3	61.7	167.8	0.36	0.31

Table 3.7:
Elastic moduli for Pt_3Ti alloys The elastic moduli given here are the Voight moduli and the units are in GPa, except for the Poisson ratio ν and the ratio $R_{G/B}$ which are unitless.

formation compared to phases at similar percentage compositions. The $PtTi_2$ $C11_b$ phase, together with Pt_4Ti_5, were considered to investigate Ti-rich alloys within the Pt-Ti system.

Figure 3.22 shows the total DOS for the Pt_8Ti, Pt_4Ti and $C11_b$ phases. From these plots, it can be seen that the Fermi level does not lie in between two sets of peaks, as was evident for the other phases at different percentage compositions. The total DOS for Pt_4Ti is similar to the total DOS for a 75-25% Pt composition, in that the Fermi level lies within the lower energy Pt states. This is more evident in the Pt_8Ti phase. For $PtTi_2$ $C11_b$ phase, the Fermi level is located at a minima within the high energy Ti state peaks. The location of the Fermi level indicates stability and a high heat of formation, which $PtTi_2$ $C11_b$ does have, when compared to phases of similar percentage Pt composition. The Fermi level is located at maxima for both Pt_8Ti and Pt_4Ti.

The partial DOS (Figures 3.23 and 3.24) show that the d-states dominate as with the other Pt-Ti alloys. The Ti d-states which lie mainly above the Fermi level for Pt_8Ti and Pt_4Ti form very narrow peaks. The Ti d-states for $PtTi_2$ $C11_b$ form two narrow peaks, with one lying below the Fermi level. This is similar to the case for alloys at 25-75% Pt composition, where the Fermi level was located within the higher energy peaks with the Ti d-states lying mostly above the Fermi level, although some states were found to also lie below the Fermi level.

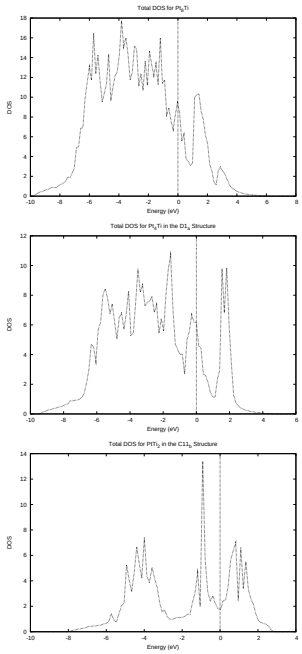

Figure 3.22:
Total DOS for different phases of PtTi, from top to bottom: Pt_8Ti, Pt_4Ti and $MoSi_2$ $C11_b$. E_F is set at 0 eV.

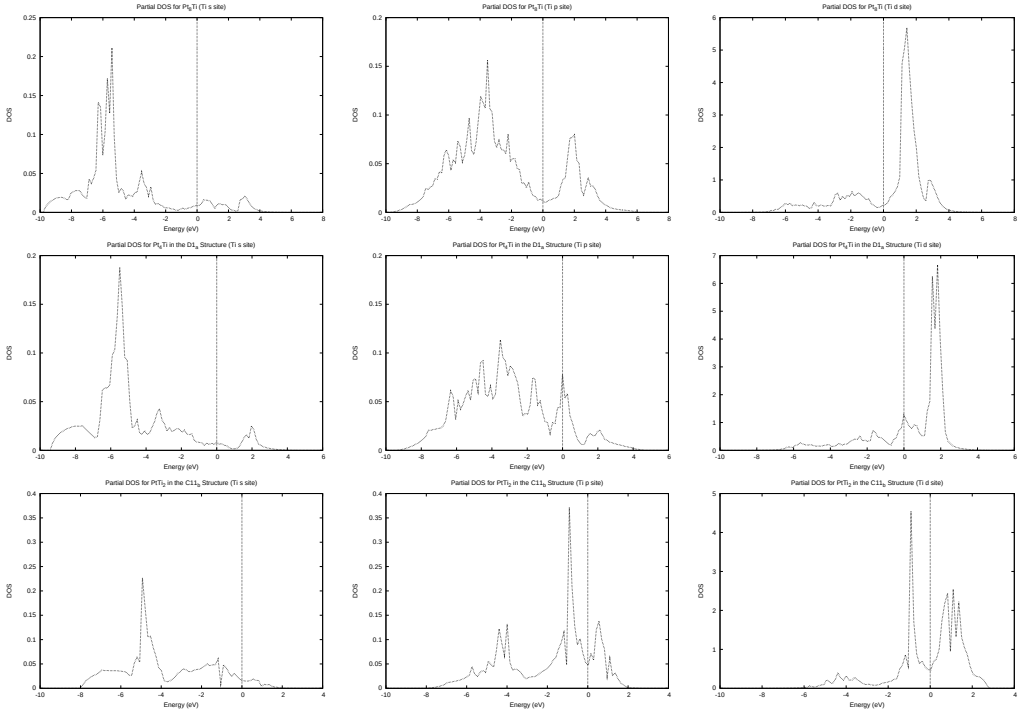

Figure 3.23:
Partial DOS (Ti site) for different phases of PtTi, from top to bottom: Pt_8Ti, Pt_4Ti and $MoSi_2$ $C11_b$. E_F is set at 0 eV.

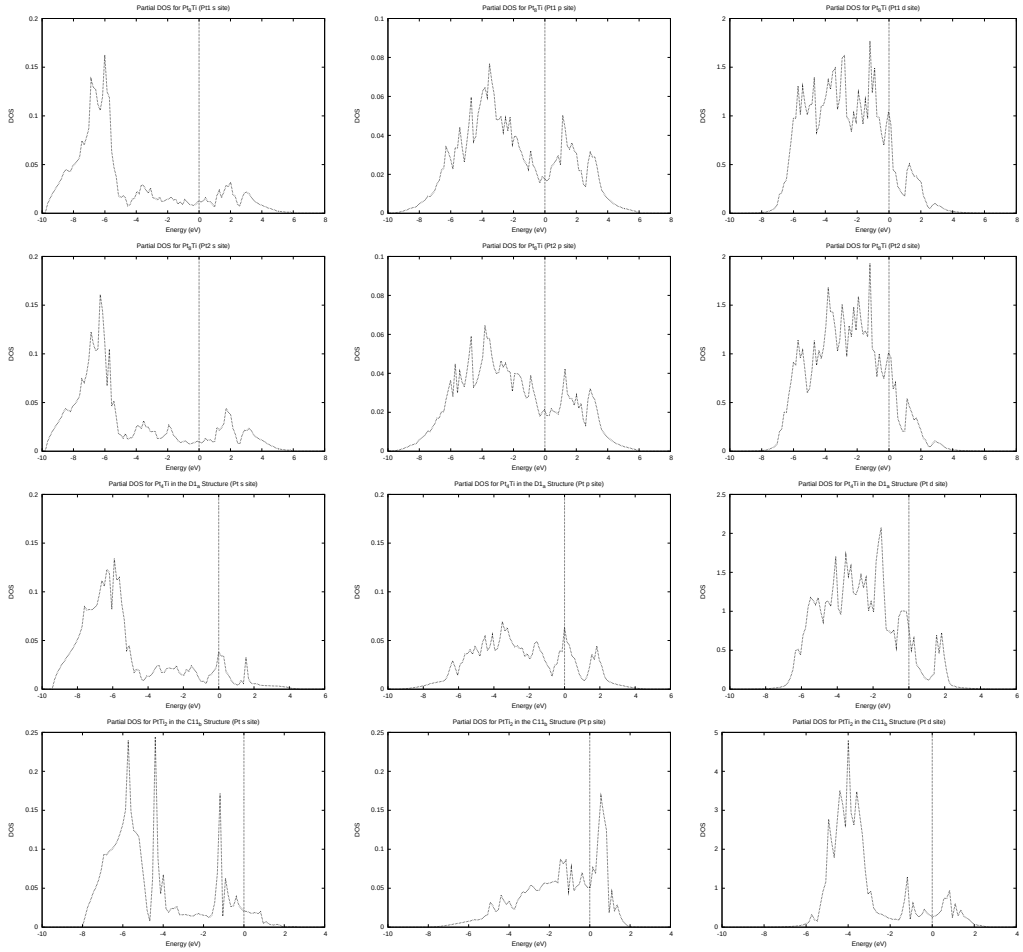

Figure 3.24:
Partial DOS (Pt site) for different phases of PtTi, from top to bottom: Pt_8Ti (the first Pt site), Pt_8Ti (the second Pt site), Pt_4Ti and $MoSi_2$ $C11_b$. E_F is set at 0 eV.

The Pt *d*-states form a broad set of peaks for Pt_8Ti and Pt_4Ti below the Fermi level. For $PtTi_2$ $C11_b$, the *d*-states are much narrower, and there are are fewer states above the Fermi level. For Pt_8Ti and Pt_4Ti, there is a significant amount of Pt *d*-states above the Fermi level.

The elastic moduli for these different phases are given in Table 3.8. Pt_8Ti has the highest bulk modulus of all of the PtTi alloys, marginally higher than Pt_2Ti $C37$. These are both higher than the bulk modulus for Pt in FCC. The bulk modulus of Pt_4Ti is also among the higher values for the alloy system. It is similar in value for the phases at 75-25% Pt

	Bulk Modulus	Shear Modulus	Young's Modulus	Poisson's Ratio	
	B	G	Y	ν	$R_{G/B}$
Pt_8Ti	252.6	99.2	263.1	0.33	0.39
Pt_4Ti	226.9	91.5	241.9	0.32	0.40
Pt_5Ti_3	212.6	86.0	227.3	0.32	0.40
$PtTi_2$	156.9	67.1	176.2	0.31	0.43

Table 3.8:
Elastic moduli for PtTi alloys at different percentage concentrations. The elastic moduli given here are the Voight moduli and the units are in GPa, except for the Poisson ratio ν and the ratio $R_{G/B}$ which are unitless.

composition.

As a measure of the strength of each phase, the bulk modulus can be compared as a function of percentage Pt composition in a structure. Taking an average of the bulk modulus at each percentage concentration, the alloys can be ordered from those with the highest bulk modulus as follows:

$$Pt_8Ti > \text{FCC Pt} > Pt_4Ti > Pt_3Ti > Pt_2Ti > Pt_5Ti_3 > PtTi > PtTi_2 > PtTi_3.$$

This shows, apart from the Pt_8Ti structure, that the value of the bulk modulus decreases on average with decreasing percentage Pt in an alloy. In other words, alloying Pt with Ti will result in a decrease in its bulk modulus, as opposed to adding strength to the metal.

The effect of alloying on the shear modulus does not follow the same pattern as the value of the bulk modulus. Generally metal alloys show an increase in the shear modulus compared to the pure metal. This is seen to some extent in the values of the shear modulus for the various phases considered in this study.

The Poisson ratio ν has been considered as a way to measure a material's ability to resist shear; a smaller value of ν may indicate more resistance by a material to shear [157]. The calculated Possion ratio for all of the phases show that all the values between 0.29 and 0.45, with FCC Pt and HCP Ti having Possion ratios of 0.38 and 0.33 respectively.

Phases with a Poisson ratio higher than 0.45 were found to have negative elastic moduli. The alloying of Pt with Ti shows that generally there may be an increase in the resistance to shear for the alloy.

The $R_{G/B}$ ratios for the various phases indicate that there is no change from the original ductile behaviour of the Pt and Ti metals. All $R_{G/B}$ ratios for the alloys are less than 0.5, thereby indicating that the alloys are also ductile in nature.

Chapter 4

The Ir-Ti System

4.1 Equilibrium Phases in the Ir-Ti System

For the Ir-Ti system, the same structures as in the previous for the Pt-Ti system (see Table 3.1) were considered. The data for the calculated crystal structures is given in Table 4.1, showing the lattice parameters for each of the phases considered in this study.

There is little experimental data available to compare with the calculated structural parameters for the various phases of the Ir-Ti alloy system. Ramakrishnan and Chandra [163] reported a lattice constant of 5.007 Å for $IrTi_3$ in the $A15$ structure. The calculated value of 5.027 Å is in good agreement with their experimental value. The experimental lattice constant of Ir_3Ti in the $L1_2$ phase is given as 3.843 Å by Chen *et al* [50]. The calculated lattice constant for that structure is 3.883 Å, a difference of 1.05%. The calculated lattice constant for IrTi $B2$ (3.122 Å) is also in excellent agreement with Schubert *et al* [164], who had given a value of 3.11 Å. For the $L1_0$ phase, Dwight and Beck [165] gave the lattice parameters as: $a_0 = 2.925$ Å and $c_0 = 3.446$ Å. The calculated values are given as 2.944 Å and 3.493 Årespectively, also in good agreement.

There is one extra structure in the Ir-Ti alloy system that was not considered for PtTi. The orthorhombic designated as αIrTi by Okamoto [58] is the low-temperature equilibrium structure for IrTi at 50% composition. It does not have a Pearson symbol or a *Strukturbericht* designation. It will be referred to either as αIrTi or IrTi-ortho (in graphs). The lattice constants for αIrTi given in Table 4.1 are in good agreement with the data

	% Ti	Space Group	Prototype	a_0	b_0	c_0
Ir	0	$Fm\bar{3}m$	Cu	3.880	a_0	a_0
Ir_8Ti	11.1	$I4/mmm$	V_4Zn_5	8.236	a_0	3.884
Ir_4Ti	20.0	$I4/m$	Ni_4Mo	6.131	a_0	3.901
Ir_3Ti	25.0	$Pm\bar{3}m$	Cu_3Au	3.883	a_0	a_0
	25.0	$I4/mmm$	Al_3Ti	3.885	a_0	7.803
	25.0	$Pm\bar{3}n$	Cr_3Si	4.974	a_0	a_0
Ir_2Ti	33.3	$Immm$	$MoPt_2$	2.791	8.456	3.815
	33.3	$Cmcm$	$ZrSi_2$	3.816	12.034	3.868
	33.3	$Pnma$	Co_2Si	5.438	3.937	8.223
	33.3	$I4/mmm$	$MoSi_2$	2.791	a_0	11.551
Ir_5Ti_3	37.5	$Ibam$	-	5.464	10.958	8.009
Ir_3Ti_2	40.0	$P\bar{3}m1$	Al_3Ni_2	4.233	a_0	5.262
IrTi	50.0		-	4.160	3.497	4.170
	50.0	$Pmma$	AuCd	4.494	2.925	4.638
	50.0	$P4/mmm$	CuAu	2.944	a_0	3.493
	50.0	$Pm\bar{3}m$	CsCl	3.122	a_0	a_0
	50.0	$Fm\bar{3}m$	NaCl	5.144	a_0	a_0
	50.0	$F\bar{4}3m$	ZnS	5.656	a_0	a_0
	50.0	$Cmcm$	CrB	2.942	9.791	4.348
	50.0	$P4/nmm$	γCuTi	3.436	a_0	5.466
Ir_4Ti_5	55.6	$I4/mmm$	V_4Zn_5	8.234	a_0	4.105
$IrTi_2$	66.7	$I4/mmm$	$MoSi_2$	3.094	a_0	9.737
$IrTi_3$	75.0	$Pm\bar{3}n$	Cr_3Si	5.027	a_0	a_0
	75.0	$Pm\bar{3}m$	Cu_3Au	4.012	a_0	a_0
	75.0	$I4/mmm$	Al_3Ti	3.756	a_0	9.094
Ti	100.0	$P6_3/mmc$	Mg	2.941	a_0	4.674

Table 4.1:
The crystal structure data for the Ir-Ti system. The 50% phase with no space group designation or prototype is known only as the orthorhombic αIrTi.

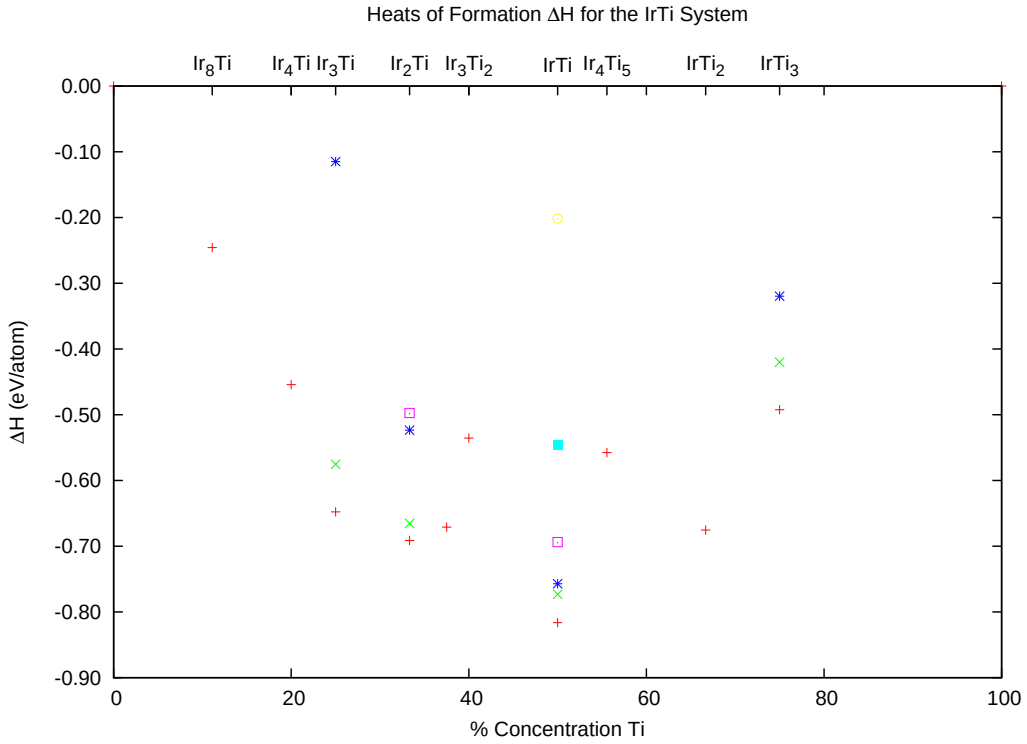

Figure 4.1:
The calculated heats of formation for the Ir-Ti system as a function of the atomic concentration of Ti, with increased binding plotted downwards.

provided by Chen and Franzen [166].

The structural data for all of the phases given in Table 4.1 was concluded to be accurate. The electronic structure and the elastic constants was calculated at these optimised lattice parameters, and the results are shown in the following sections.

4.2 Heats of Formation for the Ir-Ti System

The heats of formation for the Ir-Ti are shown in Figure 4.1. The shape of the curve of the most stable, equilibrium phases of Ir-Ti alloys at the different percentage compositions is very similar to the Pt-Ti system (see Figure 3.1). Four key differences with the Pt-Ti system are that, firstly, the heats of formation are lower than all of the corresponding Pt-Ti alloys. Secondly, where there are competing structures at one percentage composition, the gap between the phase with the highest heat of formation and the other phases is more

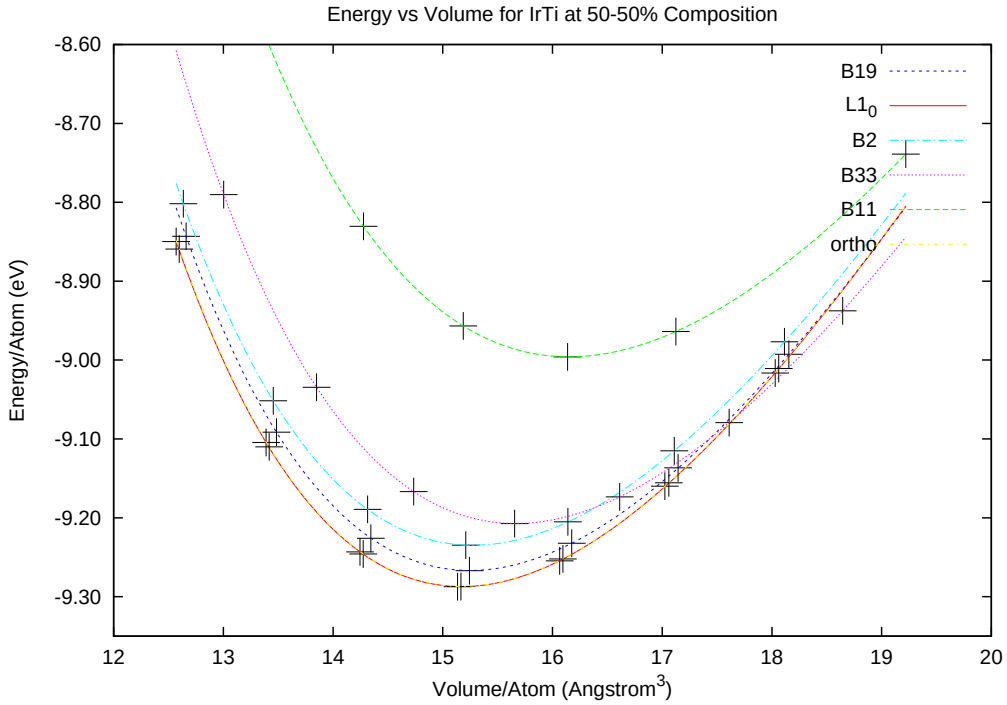

Figure 4.2:
Energy (per atom) versus volume (per atom) for the six phases of IrTi: αIrTi, $B19$ (prototype AuCd), $L1_0$ (prototype CuAu), $B2$ (prototype CsCl), $B33$ (prototype CrB) and $B11$ (prototype γCuTi).

pronounced. Thirdly, in the Pt-Ti system, the heats of formation for phases at 75, 66.7 and 62.5% Pt composition are comparable to phases at 50% composition. In the Ir-Ti system, the heats of formation for phases in those compositions are less comparable to one another, and all lower than the phases at 50% Ir composition. Lastly, the order of the heats of formations for competing structures at the same percentage composition is not the same in Pt-Ti and Ir-Ti.

4.3 50-50% Composition

The energy-volume curves for five of the seven phases at 50% Ir composition are shown in Figure 4.2. This shows that the ordering differs to the 50% Pt composition: the equilibrium structure at this composition in the Ir-Ti system is the orthorhombic αIrTi phase. This structure has a minimum energy very similar to that of the tetragonal $L1_0$ phase. This corresponds to the findings by Chen and Franzen [166]. The high-temperature phase

for IrTi is the $B2$phase - the same as for PtTi - the two intermediate phases are the above-mentioned orthorhombic as well as the $B19$ phase (which was the equilibrium structure for PtTi at 50%).

The $B33$ phase, which was an intermediate between the low and high temperature structures for 50% PtTi, has an equilibrium energy higher than the $B2$. $B11$ is still the least stable of these structures. From the equilibrium αIrTi can only access the other structures via heat, as pressure alone cannot create a transition from the intermediates to $B2$.

The energy band structures for αIrTi, $B19$, $L1_0$, $B2$ and $B33$ and the total DOS for these are shown in Figures 4.3 and 4.4 respectively. The total DOS for αIrTi, $B19$, $L1_0$ and $B2$ are very similar. Each DOS has low energy sets of peaks that are separated by the high energy peaks by a small dip in the DOS. This dip is narrower for the low temperature phase, as well as the two intermediates, showing that there is more stability of the low temperature αIrTi compared to $B2$. The Fermi level is located at maxima for αIrTi, $L1_0$and $B19$. It is on a flat part of the DOS for $B2$ and at a minimum for $B33$.

The partial DOS are shown in Figures 4.5 (Ti site) and 4.6 (Ir site). As with the Pt-Ti alloy system, the d-states dominate the DOS, with Ir d-states mainly below the Fermi level and mostly occupied. The Ti d-states are mostly above the Fermi level. One difference with the PtTi alloys (see Figures 4.5 and 3.6) is that the Ir d-states form broader peaks than Pt d-states for the 50% Pt phases. The Ti d-states still form a narrow set of peaks for IrTi. The contribution of Ir d-states above the Fermi level and the Ti d-states below the Fermi level is increased in comparison to PtTi alloys at this composition. This shows increased stability of the IrTi alloys over the PtTi structures, and that there is good stability among the alloys of this composition.

The elastic constants for the different IrTi phases at 50% composition are listed in Table 4.2. The mechanical stability restrictions given in the previous chapter are as follows. For cubic materials, Equations 3.2 and 3.3 are must hold. For tetragonal structures, Equations 3.2 and 3.4 are the two restrictions and for orthorhombic materials, Equations 3.4, 3.5 and 3.6 are the restrictions the elastic constants must adhere to.

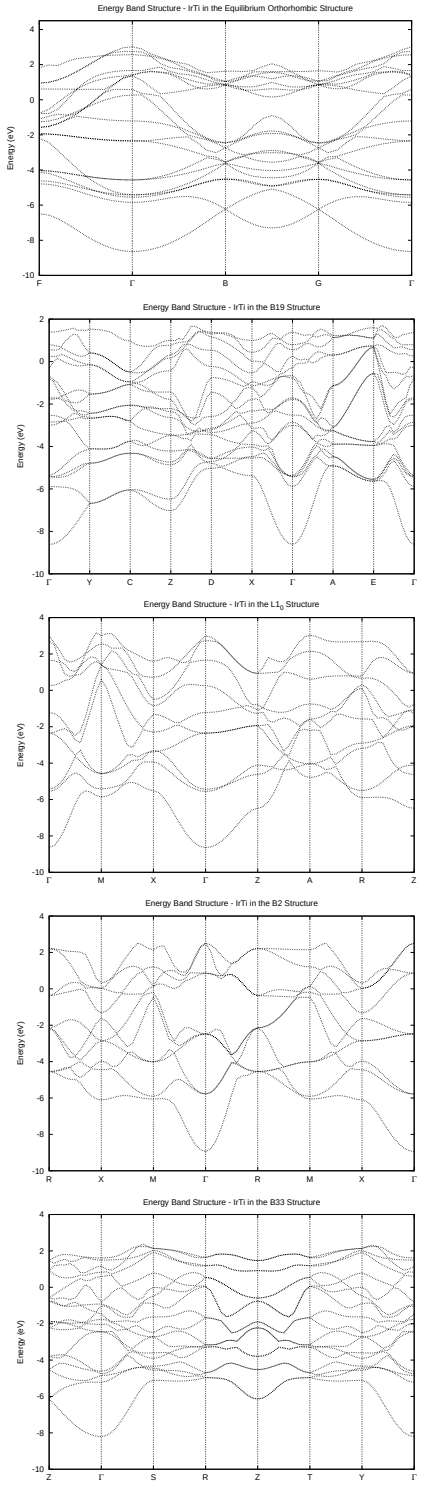

Figure 4.3:
The energy band structures along high symmetry lines for IrTi at 50-50% composition, from top to bottom: αIrTi, $B19$ (prototype AuCd), $L1_0$ (prototype CuAu), $B2$ (prototype CsCl) and $B33$ (prototype CrB). The Fermi level E_{F} is set at 0 eV.

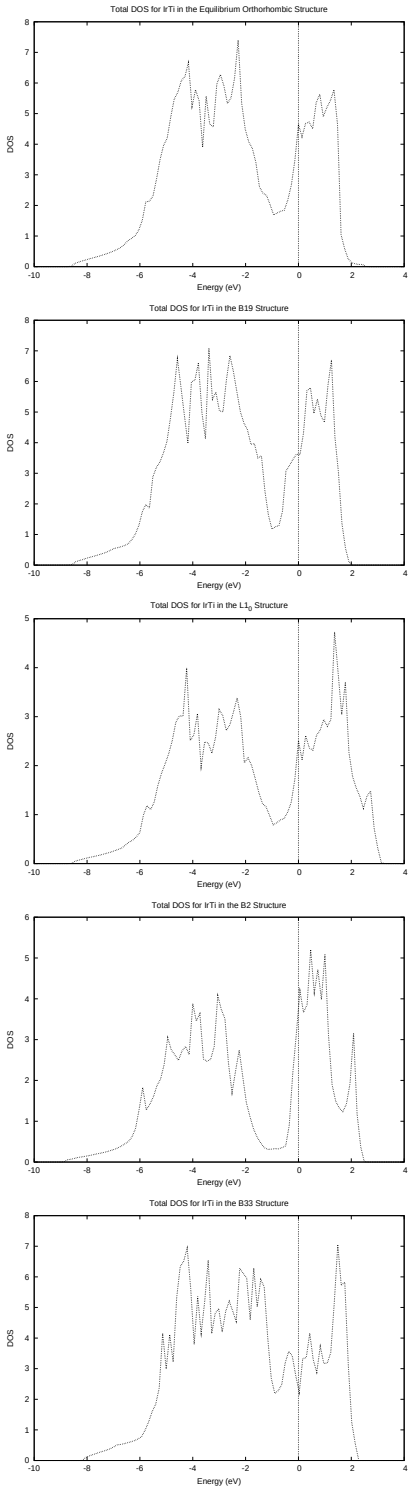

Figure 4.4:
The total density of states (DOS) IrTi at 50-50% composition, from top to bottom: αIrTi, $B19$, $L1_0$, $B2$ and $B33$. E_{F} is set at 0 eV.

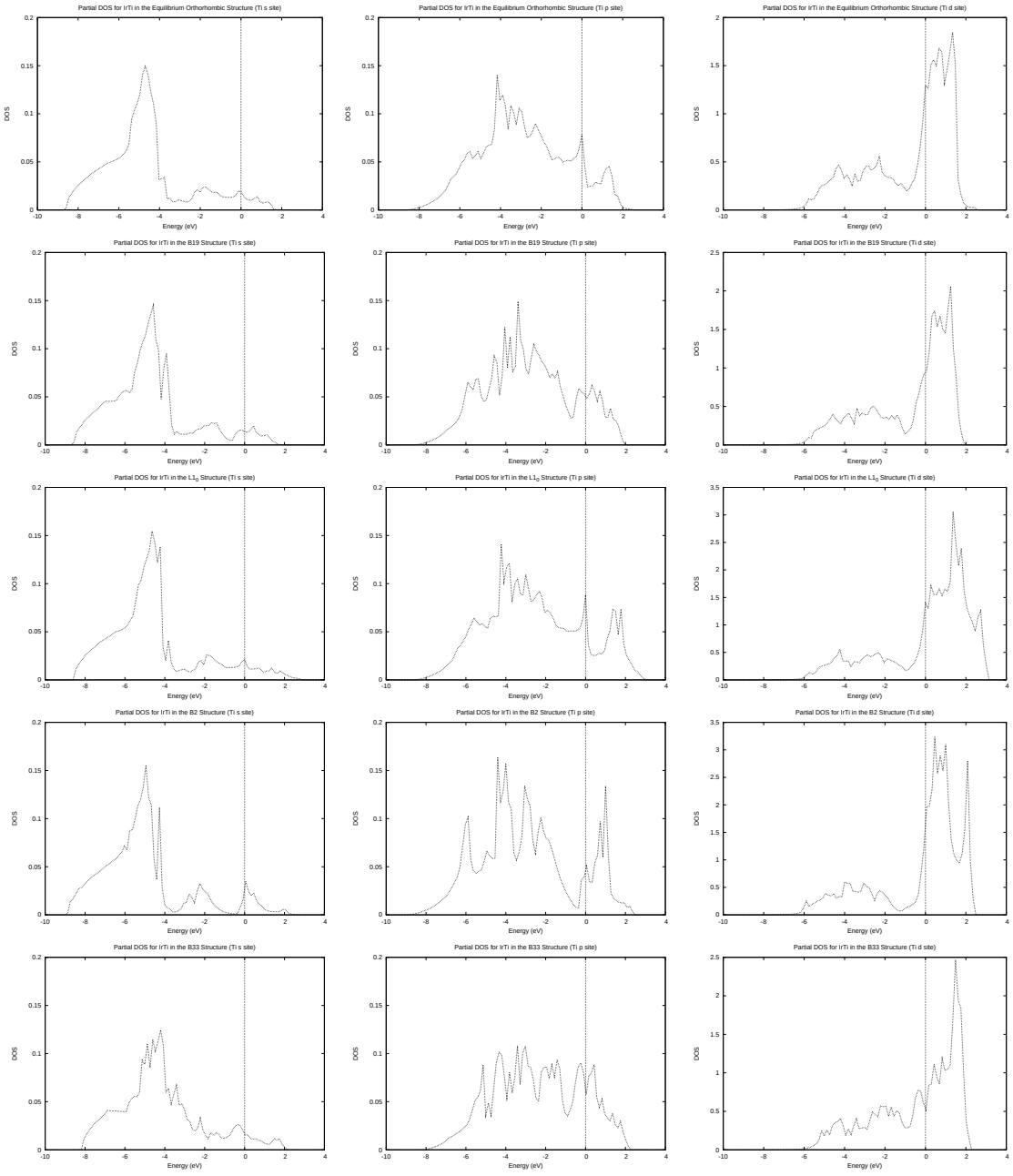

Figure 4.5:
Partial density of states for the Ti site at 50-50% composition. The left column is the partial density of states for the s states, the middle column the p states and the right column the d sites. The scale for the s and p sites is the same, but different for the d site. From top to bottom: αIrTi, $B19$, $L1_0$, $B2$ and $B33$ structures. E_{F} is set at 0 eV.

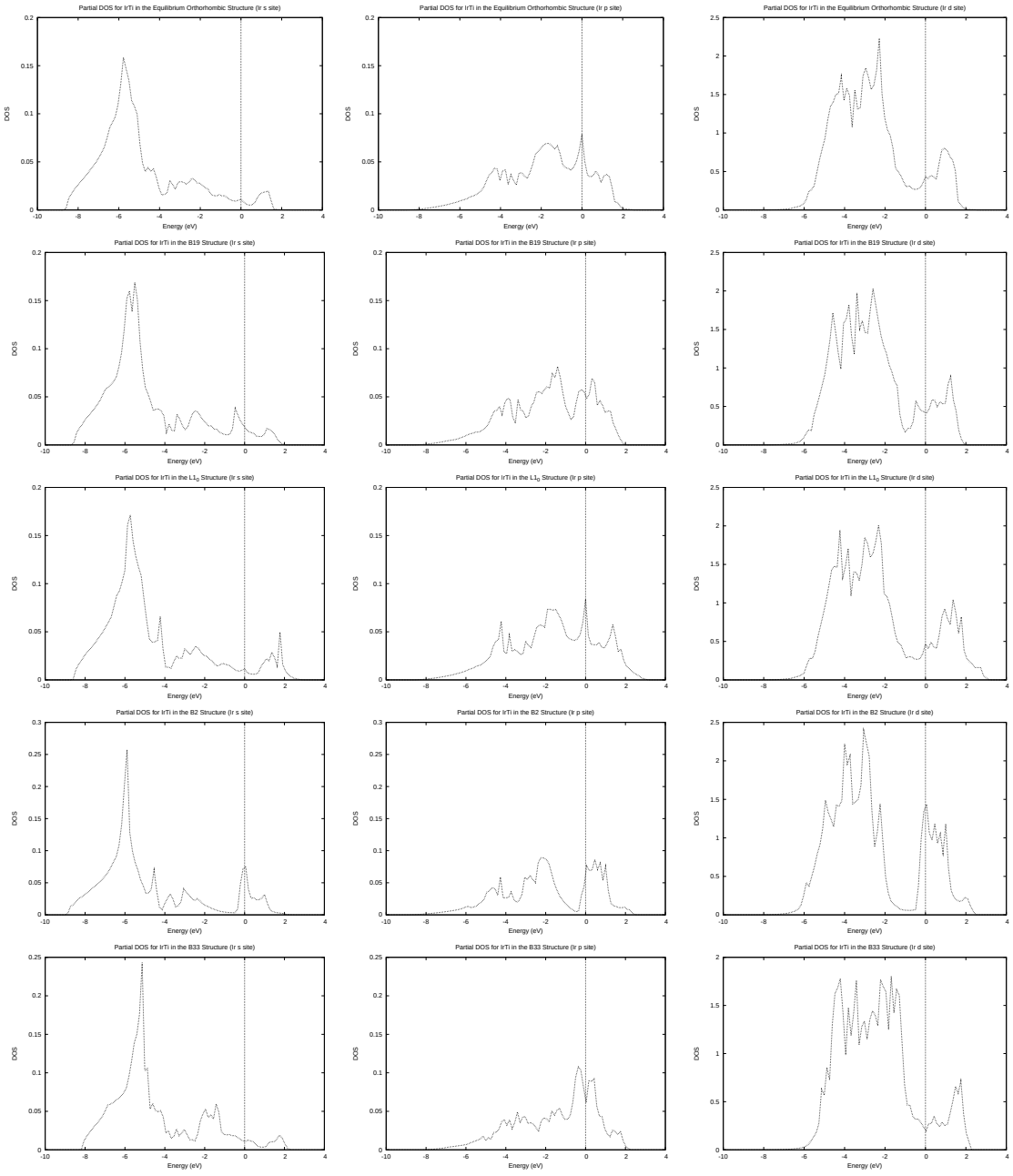

Figure 4.6:
Partial density of states for the Ir site at 50-50% composition. The left column is the partial density of states for the s states, the middle column the p states and the right column the d sites. The scale for the s and p sites is the same, but different for the d site. From top to bottom: $B19$, $L1_0$, $B2$, $B33$ and $B11$ structures. E_F is set at 0 eV.

	C_{11}	C_{12}	C_{13}	C_{22}	C_{23}	C_{33}	C_{44}	C_{55}	C_{66}
αIrTi	310.5	179.6	179.5	321.0	177.3	310.1	83.5	113.9	84.2
$B19$	343.5	147.1	174.9	380.6	144.3	311.9	68.1	-14.2	77.8
$L1_0$	355.4	159.1	170.8			331.1	40.5		56.8
$B2$	32.1	313.5					55.2		
$B11$	153.5	207.6	162.5			264.8	58.2		116.4
$B33$	311.1	107.0	144.2	347.2	197.6	342.7	70.3	76.9	-0.86
$B1$	293.1	106.9					1.7		
$B3$	104.2	108.5					-17.5		

Table 4.2:
The elastic constants for IrTi alloys at the 50-50% composition. All elastic constant values are in GPa. The $B1$ and $B3$ phases have also been included here.

The three cubic systems are $L1_0$, $B1$ and $B3$. Both $L1_0$ and $B3$ have elastic constants that do not satisfy Equation 3.2, while C_{44} for $B3$ is also negative. In the PtTi system, these were the same phases that did not show stability due to the elastic constants. $B1$ has a C_{44} elastic constant of only 1.7 GPa, showing that it is highly unlikely that this phase would be accessible for IrTi. $B2$ is the high temperature phase for this composition IrTi (in the same way as for the PtTi alloys).

The dispersion relations for IrTi $B2$ is shown in Figure 4.7. The dispersion relation is very similar to that for PtTi $B2$. The modes are unstable at R and M. There are branches where the modes are unstable and these correspond with PtTi $B2$. It is concluded that this phase is also, then, dynamically stabilized by anharmonic phonons. Hence there is an observed $B2$ phase for IrTi as well as for PtTi.

There are two tetragonal strucures at this composition, $L1_0$ and $B11$. $L1_0$ is mechanically stable, with its elastic constants satisfying Equations 3.2 and 3.3. $B11$ is not mechanically stable since C_{12} is bigger than C_{11}.

The three orthorhombic structures are αIrTi, $B19$ and $B33$. The elastic constants con-

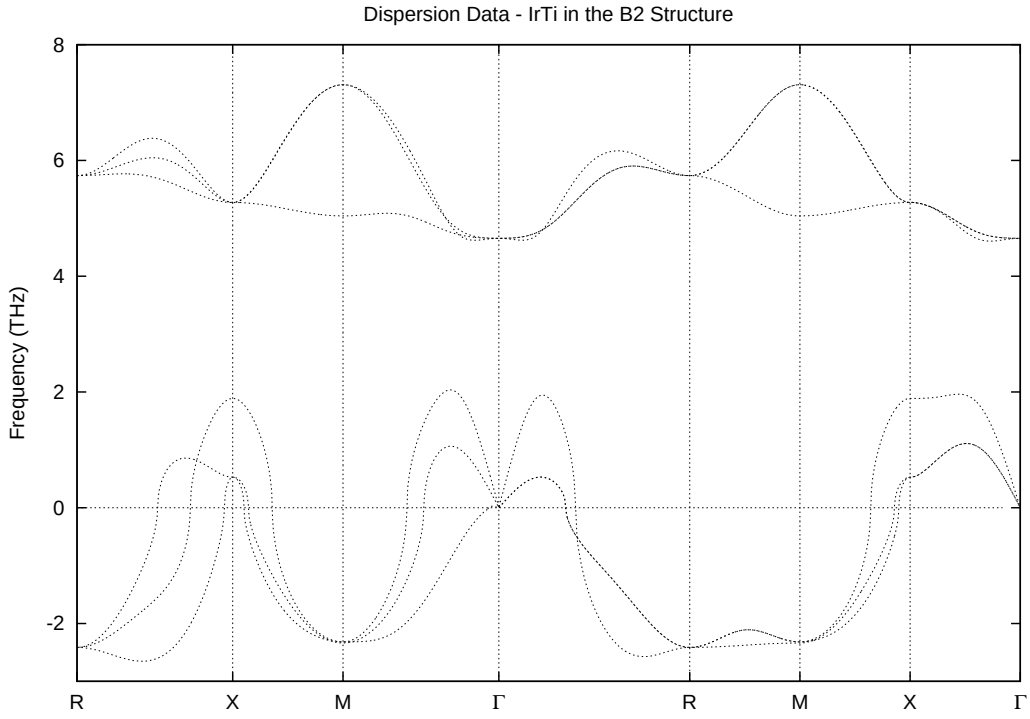

Figure 4.7:
The phonon dispersion for IrTi $B2$ along high symmetry lines. Imaginary frequencies are plotted as negative values.

firm the stability of the equilibrium structure, $C37$. $B19$ has elastic constants that satisfy the three requirements mentioned previously, except for one of the elastic constants, C_{44}, which is negative. $C11_b$ also has an elastic constant less than 0, that being C_{44}.

The elastic moduli for IrTi are given in Table 4.3. The negative values for the shear and Young's moduli come about from the requirement in Equation 3.2 not being fulfilled. The bulk moduli are smaller than for Ir in FCC. The shear and Young's moduli are also much lower than for Ir in FCC, and these values have a wide range starting from αIrTi which has the highest values.

The structures at this composition are all ductile, as $R_{G/B}$ for each of the structures is less than 0.5. Ir is a brittle material, with an $R_{G/B}$ ratio of 0,60. The alloys show ductile behaviour which corresponds with HCP Ti ($R_{G/B} = 0.38$). As the bulk modulus has been changing when Ir is alloyed with increasing Ti, the brittle bevahiour of an Ir-alloy

	Bulk Modulus	Shear Modulus	Young's Modulus	Poisson's Ratio	
	B	G	Y	ν	$R_{G/B}$
αIrTi	223.8	83.4	222.5	0.33	0.37
$B19$	218.8	64.3	175.8	0.37	0.29
$L1_0$	227.0	63.7	174.6	0.37	0.28
$B2$	219.7	-23.2	-72.1	0.56	-0.11
$B11$	181.9	49.2	135.3	0.38	0.27
$B33$	211.0	66.1	179.5	0.36	0.31
$B1$	168.9	38.3	106.8	0.40	0.23
$B3$	105.7	-10.9	-34.0	0.55	-0.10

Table 4.3:
Elastic moduli for IrTi alloys at the 50-50% composition. The elastic moduli given here are the Voight moduli and the units are in GPa, except for the Poisson ratio ν and the ratio $R_{G/B}$ which are unitless.

changes with a certain amount of Ti present.

The Poisson ratio ν also gives an indication of the ductile or brittle nature of a material. Since the value of ν is around 0.33 or higher, this is further confirmation that the alloys are brittle. The Poisson ratio may also indicate a resistance to shear. In the case of these alloys, ν is not considered small enough. These materials would be less likely to resist shear than Ir in FCC.

4.4 75-25% Composition

Figure 4.8 shows the energy-volume curve for the 75% Ir composition. The energy-volume relations show that the $L1_2$ phase the most stable of the three that are considered here. For the Pt_3Ti alloys, the minimum energy of the $L1_2$ and $D0_{22}$ phases is very similar, as were the heats of formation for the two phases. The $L1_2$ phase in the Ir-Ti system has a larger difference in both the minimum energy, as well as the heats of formation.

Once more, the higher-energy $A15$ is not accessible via pressure only from $L1_2$, nor is $D0_{22}$. This means a transition may only be achieved using high temperature or by the

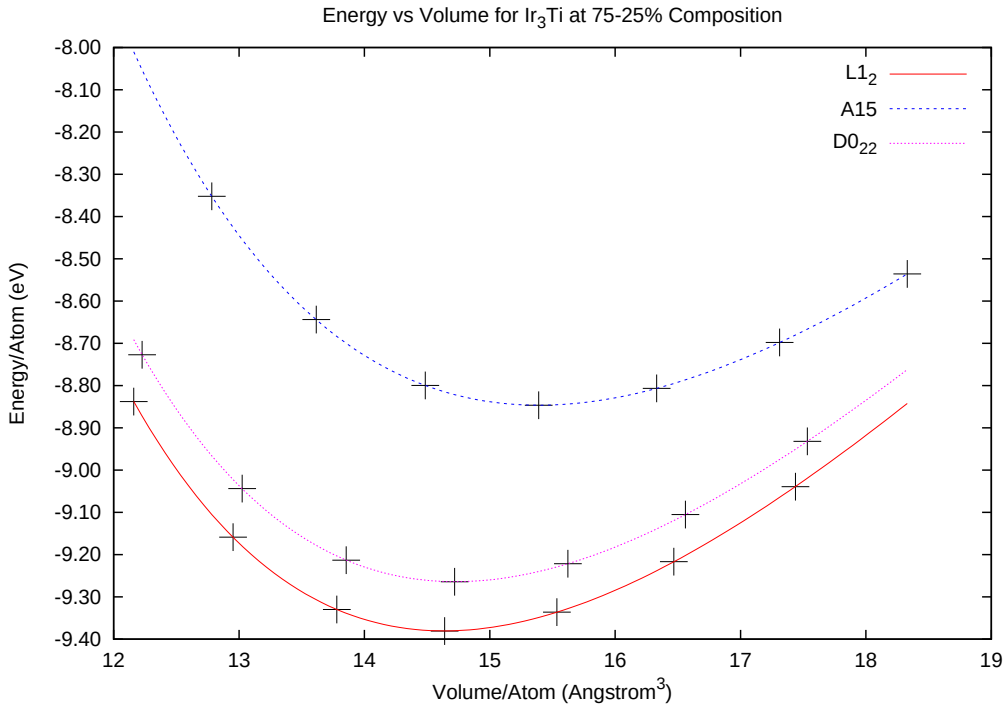

Figure 4.8:
Energy (per atom) versus volume (per atom) for the five phases of IrTi: $B19$ (prototype AuCd), $L1_0$ (prototype CuAu), $B2$ (prototype CsCl), $B33$ (prototype CrB) and $B11$ (prototype γCuTi).

method to obtain Pt_3Ti $D0_{22}$ described by Schryvers and Amelinckx [73].

The total DOS for the three phases is shown in Figure 4.9. The Fermi level is close to a minimum only for $D0_{22}$. For $A15$, the Fermi level is closer to a maximum, while being on the decreasing part of the DOS, approaching a minimum that forms a small gap between lower energy peaks below the Fermi level and a narrow set of peaks above the Fermi level. The total DOS is distinct for each of the structures.

The partial DOS for the Ti and Ir sites are shown in Figures 4.10 and 4.11 respectively. The d-states continue to dominate the DOS. Ir d-states form a broad set of peaks that lie mainly below the Fermi level, but with significant contribution to the DOS above the Fermi level. Ti d-states form very narrow peaks above the Fermi level. There is a little contribution below the Fermi level, except for $A15$, where the contribution is significant. Since there are Ir d-states above the Fermi level and some Ti states below, this indicates

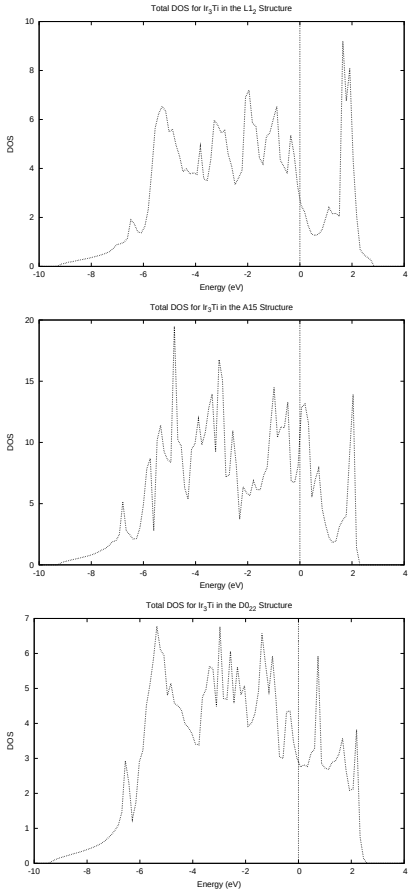

Figure 4.9:
The total DOS for IrTi at 75-25% composition, from top to bottom: $L1_2$, $A15$ and $D0_{22}$. E_{F} is set at 0 eV.

that there is some hybridisation as well as covalent bonding between orbitals on the sites [64]. When going from the higher temperature $D0_{22}$ to $L1_2$, there is a lowering of the total DOS at the Fermi level. This lowering of the DOS contributes to the stability of the $L1_2$ phase.

The elastic constants for Ir_3Ti (listed in Table 4.4) show the mechanical stability of $L1_2$ and $D0_{22}$, but that $A15$ is mechanically unstable. A cubic crystal requires $C_{44}$to be positive [154]; since $C_{44} = -1183.9$ GPa, this is not the case for $A15$.

The elastic moduli are listed in Table 4.5. The negative shear and Young's modulus for $A15$ confirm the instability of the structure. Its Poisson and $R_{G/B}$ ratio are unphysi-

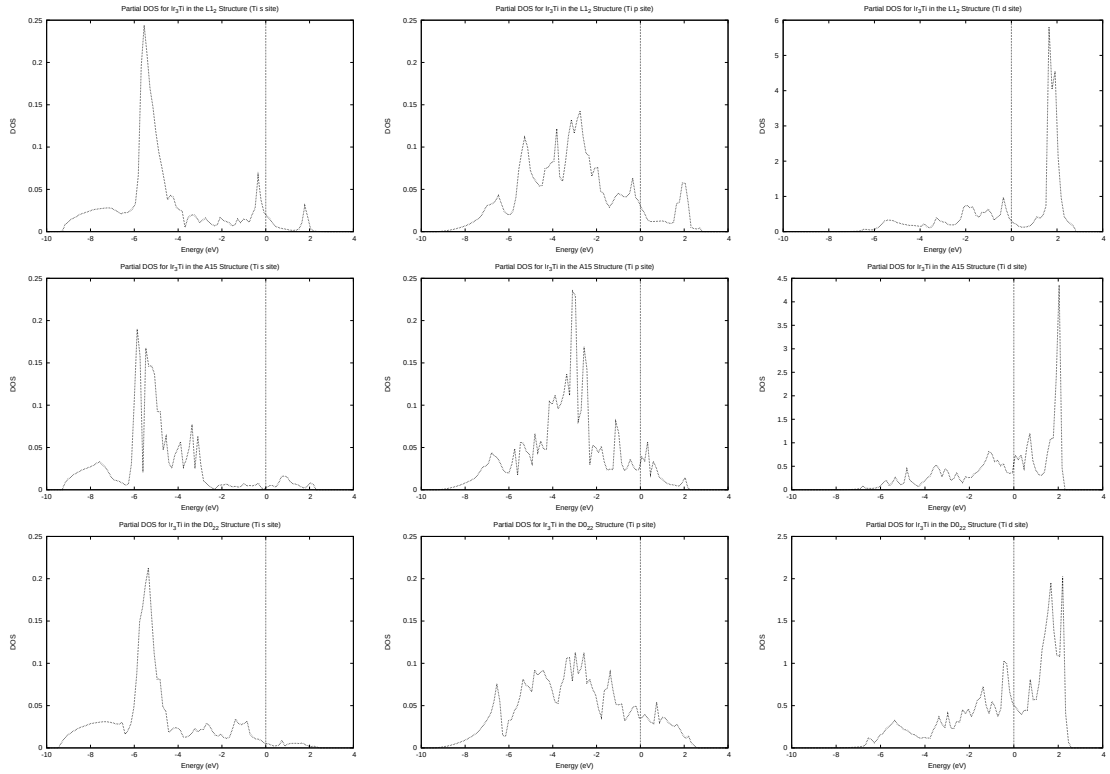

Figure 4.10:
Partial density of states for the Ti site at 75-25% composition. The left column is the partial density of states for the s states, the middle column the p states and the right column the d sites. The scale for the s and p sites is the same, but different for the d site. From top to bottom: $L1_2$, $A15$, $D0_{22}$ structures.

cal.

The bulk modulus, shear modulus and Young's modulus for Ir in FCC (337.8 GPa, 202.8 GPa and 506.9 GPa, respectively) are all larger than the corresponding values for both $L1_2$ and $D0_{22}$. The alloys have a Poisson and an $R_{G/B}$ ratio that are similar to FCC Ir (0.25 and 0.60). A small value of the Poisson's ratio may be indicative of a resistance to shear, which would be the case for both $L1_2$ and $D0_{22}$. These values are smaller than the Poisson ratios for Pt_3Ti $L1_2$ and $D0_{22}$. Since the $R_{G/B}$ ratios are both larger than 0.5, $L1_2$ and $D0_{22}$ are both brittle materials, as is Ir. A smaller Poisson's ratio ν corresponds to a larger $R_{G/B}$ [50], which leads to a material being brittle in nature. This again confirms the brittle nature of both $L1_2$ and $D0_{22}$, as their Poisson ratios (0.24 and 0.25 respectively) are smaller than 1/3.

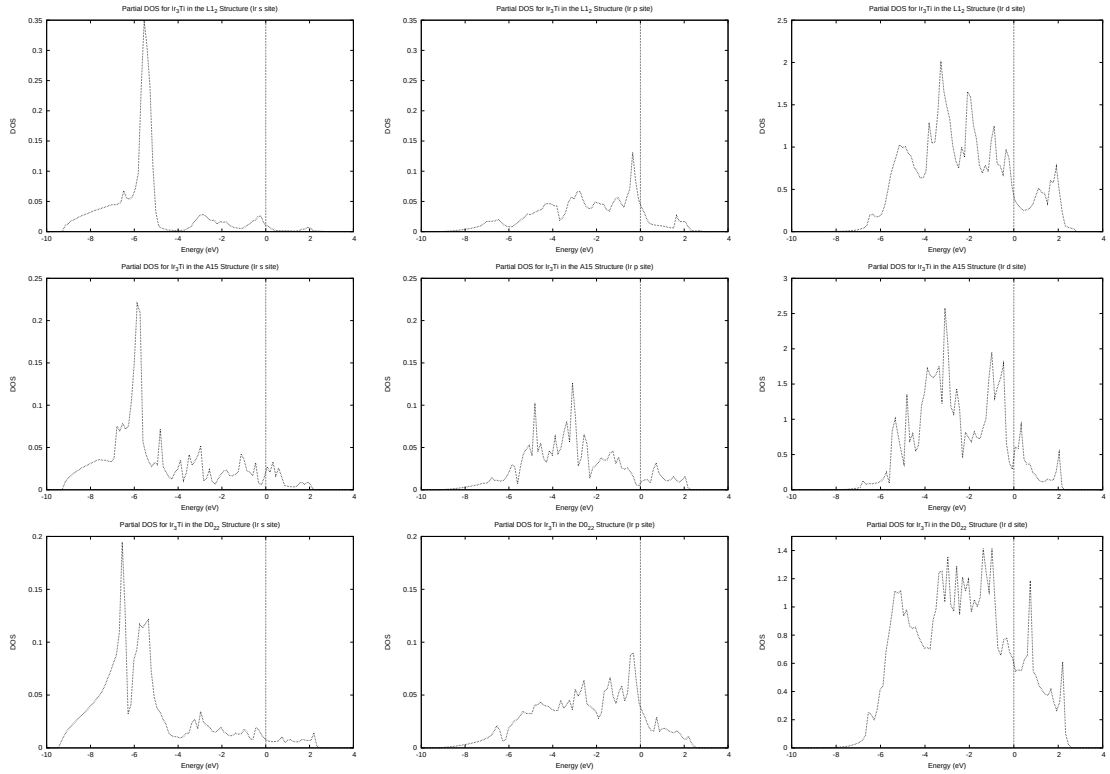

Figure 4.11:
Partial density of states for the Ir site at 75-25% composition. The left column is the partial density of states for the s states, the middle column the p states and the right column the d sites. The scale for the s and p sites is the same, but different for the d site. From top to bottom: $L1_2$, $A15$, $D0_{22}$ structures.

The Cauchy pressure [50] for $L1_2$ is $C_{12} - C_{44} = -8.7$ GPa. Negative Cauchy pressure indicates a directional bonded material. This confirms the conclusion from the partial DOS (Figures 4.10 and 4.11) of covalent bonding. It also shows once more the brittle nature, with directional bonding, of $L1_2$.

	C_{11}	C_{12}	C_{13}	C_{33}	C_{44}	C_{66}
$L1_2$	442.6	212.7			221.4	
$A15$	377.1	187.4			-1183.9	
$D0_{22}$	438.1	212.0	198.5	448.9	194.4	214.5

Table 4.4:
The elastic constants for Ir_3Ti alloys. All elastic constant values are in GPa.

	Bulk Modulus	Shear Modulus	Young's Modulus	Poisson's Ratio	
	B	G	Y	ν	$R_{G/B}$
$L1_2$	289.3	178.8	444.8	0.24	0.62
$A15$	250.6	-672.4	-19090.0	13.20	-2.68
$D0_{22}$	282.7	168.4	421.6	0.25	0.60

Table 4.5:
Elastic moduli for Ir_3Ti alloys The elastic moduli given here are the Voight moduli and the units are in GPa, except for the Poisson ratio ν and the ratio $R_{G/B}$ which are unitless.

4.5 25-75% Composition

For the 25% Ir composition, the same phases from the 75% composition were studied were studied. The energy-volume curves for $L1_2$, $A15$ and $D0_{22}$ are shown in Figure 4.12. As with $PtTi_3$, the equilibrium phase is $A15$. The ordering is the same as the heats of formation, with $A15$ being the most stable, followed by $D0_{22}$ and then $L1_2$.

The total DOS for $ItTi_3$ is shown in Figure 4.13. The total DOS is similar to the $PtTi_3$ alloys, in that the Fermi level no longer lies in the gap between two main sets of peaks, but within the set of higher energy peaks. For the equilibrium $A15$, the Fermi level is located at a maximum in the DOS; For $D0_{22}$, the Fermi level lies on a decreasing part of the DOS, close to a minimum.

The d-states still dominate the partial DOS, at both the Ir and Ti sites (Figures 4.14 and 4.15). The s-states contribute somewhat more than the p-states for both Ir and Ti. The Ir d-states form narrow peaks below the Fermi level and are all occupied. There is a small contribution above the Fermi level. The Ti d-states, on the other hand, form one broad set of peaks mostly above the Fermi level but also partially below. A smaller set of peaks is well below the Fermi level, overlapping the with Ir d-states. The presence of Ti d-states below the Fermi level, overlapping with Ir states, indicates good stability for the alloys at this composition.

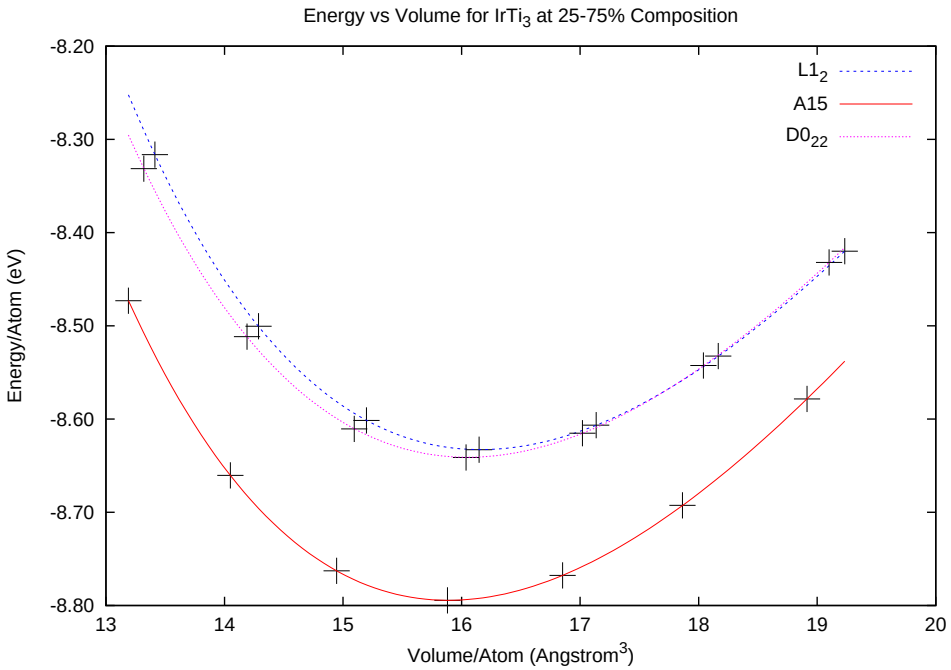

Figure 4.12:
Energy (per atom) versus volume (per atom) for the three phases of $IrTi_3$: $L1_2$, $A15$ and $D0_{22}$.

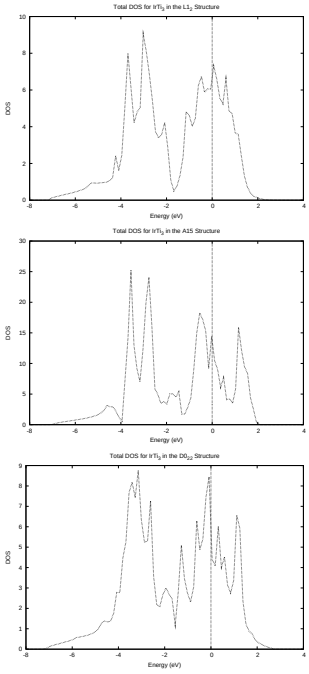

Figure 4.13:
The total DOS for IrTi at 25-75% composition, from top to bottom: $L1_2$, $A15$, and $D0_{22}$. E_F set at 0 eV.

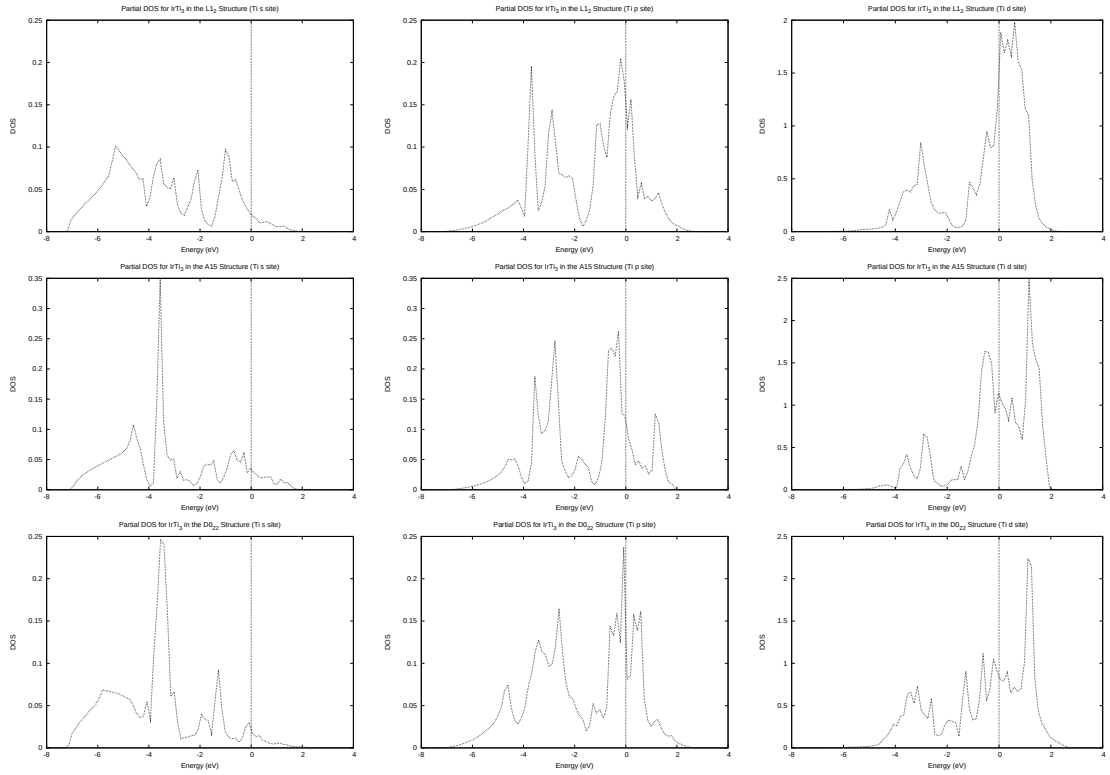

Figure 4.14:
Partial density of states for the Ti site at 25-75% composition. The left column is the partial density of states for the s states, the middle column the p states and the right column the d sites. The scale for the s and p sites is the same, but different for the d site. From top to bottom: $L1_2$, $A15$, $D0_{22}$ structures.

The elastic constants for the three phases is given in Table 4.6. $A15$ and $L1_2$ are both cubic materials, and hence the elastic constants are restricted by Equations 3.2 and 3.3, while $D0_{22}$ is a tetragonal, the restrictions being Equations 3.2 and 3.4.

For the two cubic phases, $L1_2$ is not mechanically stable since the elastic constants C_{11} and C_{12} do not satisfy Equation 3.2. C_{44} for $L1_2$ is also very small, being the smallest C_{44} for all of the cubic IrTi alloys. The same requirement (Equation 3.2) is not satisfied for the elastic constants of $D0_{22}$. This crystal is, hence, not mechanically stable. For $A15$, the elastic constants show that it is mechanically stable, and satisfies its position as the equilibrium structure for this composition.

Table 4.7 gives the elastic moduli for $IrTi_3$ $A15$, $D0_{22}$ and $L1_2$. These values further show

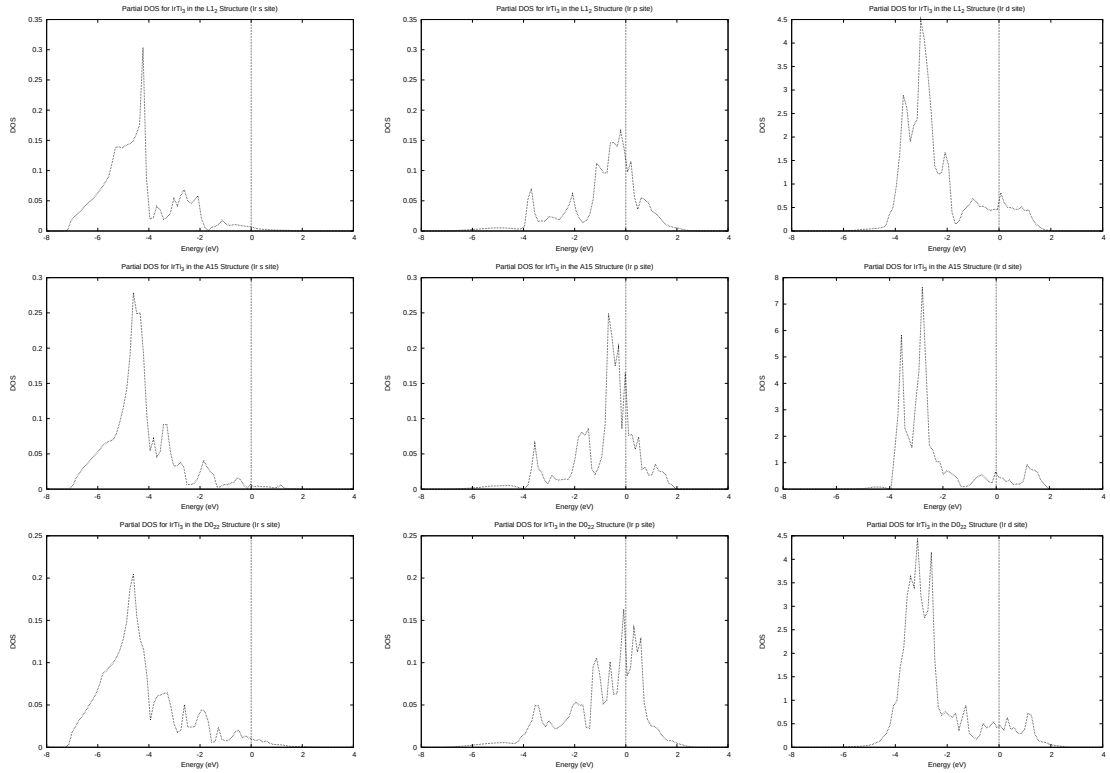

Figure 4.15:
Partial density of states for the Ir site at 25-75% composition. The left column is the partial density of states for the s states, the middle column the p states and the right column the d sites. The scale for the s and p sites is the same, but different for the d site. From top to bottom: $L1_2$, $A15$, $D0_{22}$ structures.

	C_{11}	C_{12}	C_{13}	C_{33}	C_{44}	C_{66}
$L1_2$	128.0	175.0			12.9	
$A15$	220.6	135.1			45.3	
$D0_{22}$	102.8	242.4	122.8	229.5	45.0	39.2

Table 4.6:
The elastic constants for $IrTi_3$ alloys. All elastic constant values are in GPa.

	Bulk Modulus	Shear Modulus	Young's Modulus	Poisson's Ratio	
	B	G	Y	ν	$R_{G/B}$
$L1_2$	159.3	-1.7	-5.1	0.56	-0.01
$A15$	163.6	44.2	121.8	0.38	0.27
$D0_{22}$	156.8	22.3	63.9	0.43	0.14

Table 4.7:
Elastic moduli for $IrTi_3$ alloys The elastic moduli given here are the Voight moduli and the units are in GPa, except for the Poisson ratio ν and the ratio $R_{G/B}$ which are unitless.

evidence that the $L1_2$ phase for this composition of IrTi is not accessible as it has negative shear and Young's moduli. For $D0_{22}$, the shear modulus of 22.3 GPa is the lowest among the IrTi alloys. $D0_{22}$ has a Possion's ratio of 0.43. All of the stable IrTi alloys have a Poisson ratio of less 0.40, so the value ν for $D0_{22}$ is not in keeping with the stable IrTi alloys. Its $R_{G/B}$ ratio is 0.14; this is also the lowest $R_{G/B}$ value for all of the stable IrTi alloys. It is then concluded that $D0_{22}$ is not an accessible structure for $IrTi_3$.

The Poisson ratio of $A15$ is higher than that for FCC Ir. It corresponds more with alloys that have 50% Ti composition, i.e. different to Ir-rich alloys, for example Ir_3Ti and Ir_8Ti. As its Poisson's ratio value of 0.38 is not small, the material may be less resistant to shear. The $R_{G/B}$ of 0.27 is less than 0.5, therefore indicating that $A15$ is ductile in nature. This corresponds with HCP Ti than with FCC Ir, showing that the Ti-rich alloy is more similar to Ti rather than Ir. From Table 4.6, the Cauchy pressure $C_{12} - C_{44}$ is positive for $A15$. This confirms the ductile nature of the structure and shows that the alloy is metallically bonded.

4.6 66.7-33.3% Composition

Four phases were considered for the 66.7% Ir composition, those being the same four that were studied for the Pt_2Ti alloys: $C37$, $C49$, $MoPt_2$ and $C11_b$. The energy-volume curves for these competing structures are shown in Figure 4.16.

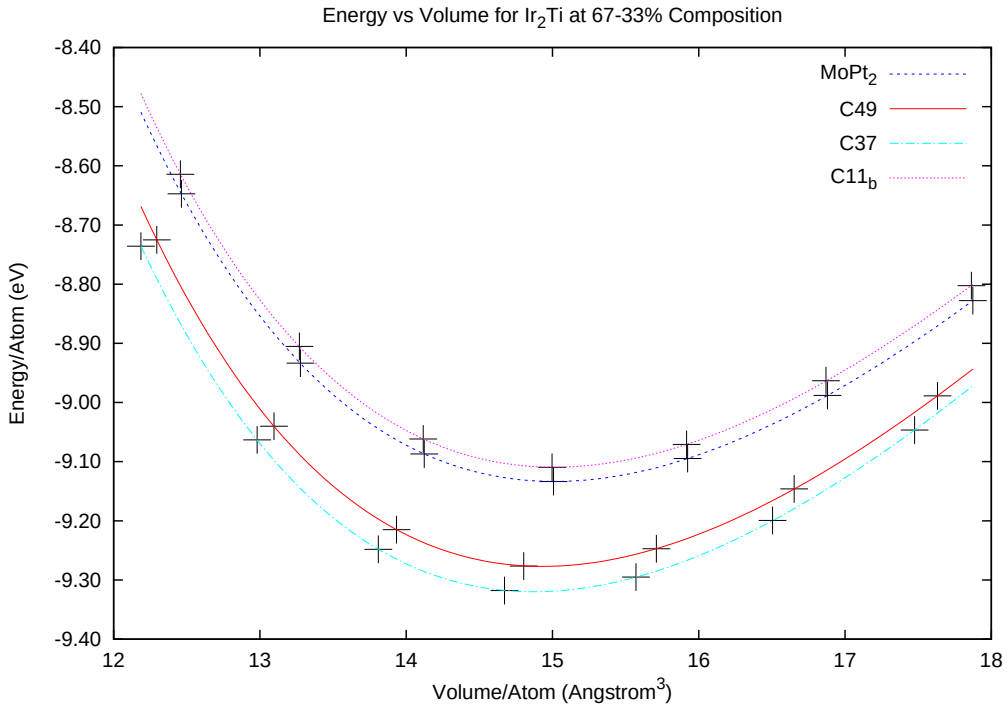

Figure 4.16:
Energy (per atom) versus volume (per atom) for the four phases of Ir_2Ti: $C37$(prototype Co_2Si), $C49$($ZrSi_2$), $MoPt_2$ and $C11_b$ (prototype Mos_2Si).

Comparing Figure 4.16 and Figure 3.17 for Pt_2Ti, the order of the minimum energies is the same. The four phases are arranged as follows from least to highest energy: $C37$, $C49$, $MoPt_2$ and $C11_b$. The four structures are arranged in the same order when considering the heats of formation (see Figure 4.1). For PtTi at 66.7% Pt composition, the low-temperature $C37$ and the high-temperature $C49$ both had very similar minimum energies. The difference is more defined for IrTi, showing that the $C37$ is the equilibrium structure at this composition. The energy-volume curves for the $MoPt_2$ and $C11_b$ are very close to one another, whereas for PtTi the $MoPt_2$ was clearly more stable than $C11_b$.

The energy band structures for the four phases are given in Figure 4.17 and the total DOS in Figure 4.18. The energy band structure confirms the metallic nature of the alloys, in keeping with all the IrTi alloys studied so far.

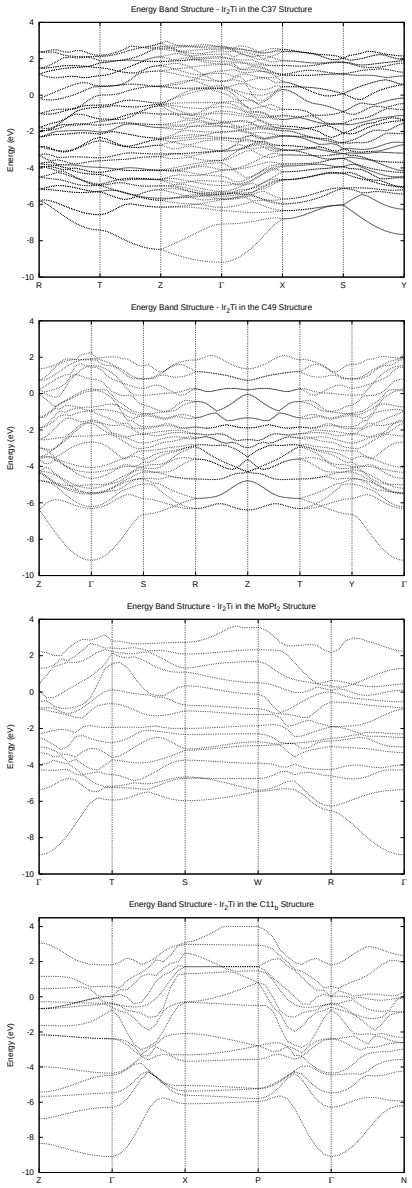

Figure 4.17:
The energy band structure for IrTi at 67-33% composition, from top to bottom: $C37$, $C49$, $MoPt_2$ and $C11_b$. E_F is set at 0 eV.

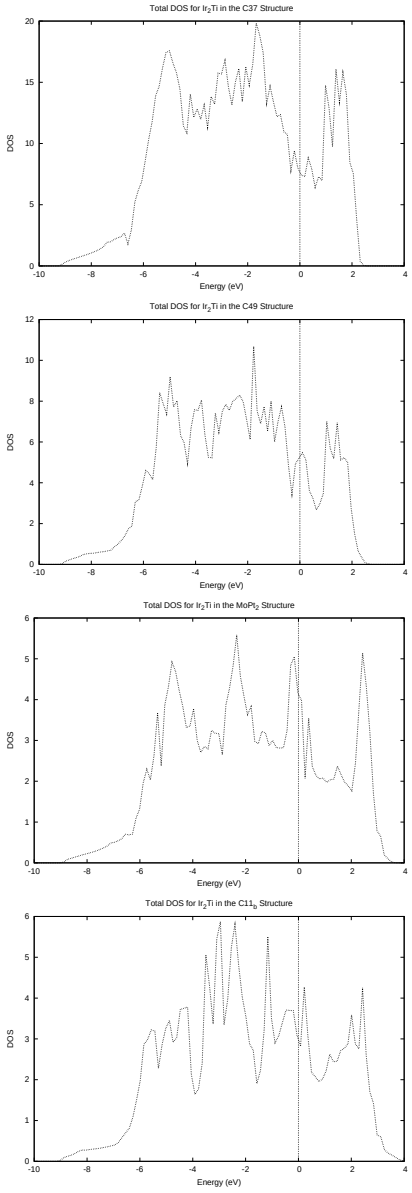

Figure 4.18:
Total DOS for IrTi at 67-33% composition, from top to bottom: $C37$, $C49$, $MoPt_2$ and $C11_b$. E_F is set at 0 eV.

	C_{11}	C_{12}	C_{13}	C_{22}	C_{23}	C_{33}	C_{44}	C_{55}	C_{66}
$C37$	491.9	195.5	142.2	399.7	223.7	454.1	187.8	99.4	183.2
$C49$	391.7	188.4	228.6	400.1	198.1	391.7	172.1	185.2	111.8
$MoPt_2$	414.7	138.7	199.5	395.4	217.0	364.2	137.7	119.1	82.4
$C11_b$	413.7	134.0	207.1			383.1	80.3		46.5

Table 4.8:
The elastic constants for IrTi alloys at the 67-33% composition. All elastic constant values are in GPa.

The total DOS (Figure 4.18) shows similarities between the low and high-temperature phases. The DOS for $MoPt_2$ and $C11_b$ are also similar. One important feature is that the DOS for all of these phases, there is no set of low and high energy peaks, separated by some dip in the DOS, as has been the case for the majority of the different phases so far. When comparing the low and high temperature structures, the Fermi level lies very close to a maximum for the high temperature $C49$, but very close to a minimum for $C37$. This shows a greater stability for $C37$ with respect to $C49$. For the other two structures, the Fermi level is located on the decreasing part of the DOS for $MoPt_2$ and close to a minimum for $C11_b$.

There is also a depletion of the DOS at the Fermi level when going from $C49$ to the more stable $C37$. This lowering of the DOS leads to more stability for $C37$ relative to $C37$.

The partial DOS for Ir_2Ti are shown in Figures 4.19 for the Ti site and 4.20 for the Ir site. The d-states still dominate the contributions. The Ir d-state, which lie mainly below the Fermi level also have significant contribution above the Fermi level. These overlap with Ti d-states, which form narrow peaks above the Fermi level, with some contribution to the total DOS below E_{F}. This shows that there is good stability for these four structures.

The elastic constants listed in Table 4.8 show that the three orthorhombic structures are mechanically stable, as they satisfy the restrictions given in Equations 3.4, 3.5 and 3.6. The tetragonal $C11_b$ also satisfies its requirements for mechanical stability (Equations 3.2

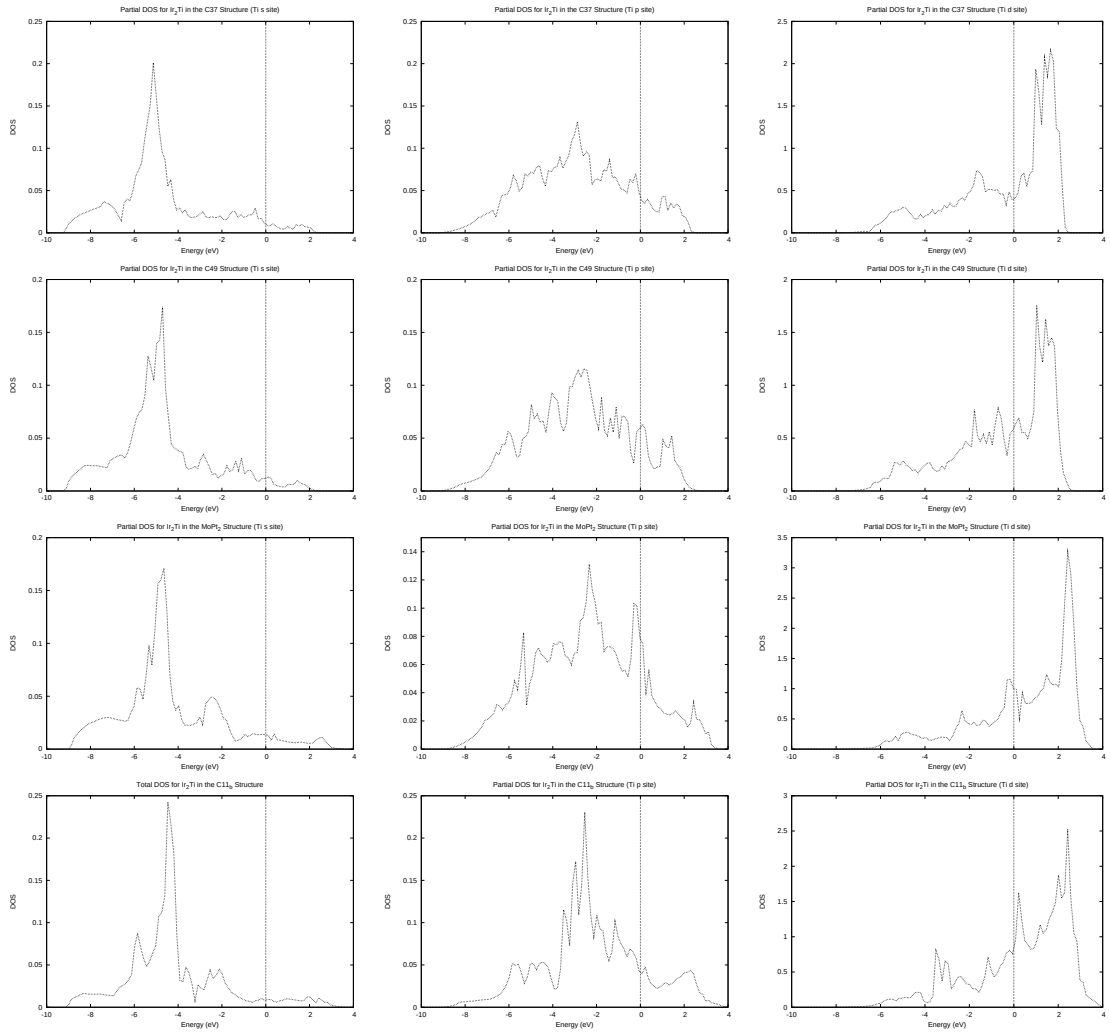

Figure 4.19:
Partial DOS for IrTi (Ti site) at 67-33% composition, from top to bottom: $C37$, $C49$, $MoPt_2$ and $C11_b$. E_F is set at 0 eV.

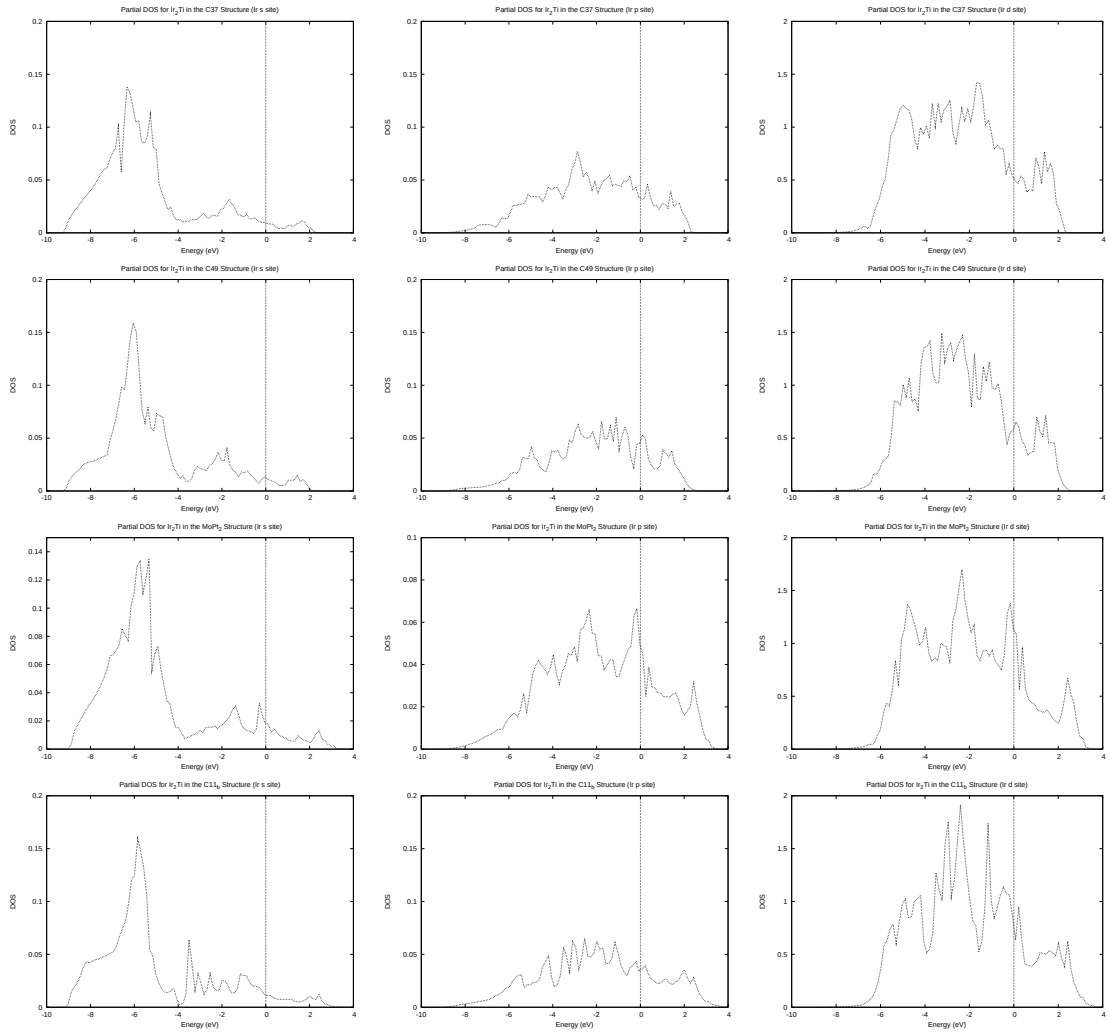

Figure 4.20:
Partial DOS for IrTi (Ir site) at 67-33% composition, from top to bottom: $C37$, $C49$, $MoPt_2$ and $C11_b$. E_F is set at 0 eV.

	Bulk Modulus	Shear Modulus	Young's Modulus	Poisson's Ratio	
	B	G	Y	ν	$R_{G/B}$
$C37$	274.3	146.4	372.8	0.27	0.53
$C49$	268.3	131.8	339.7	0.29	0.49
$MoPt_2$	253.9	109.1	286.4	0.31	0.43
$C11_b$	274.3	146.4	372.8	0.35	0.33

Table 4.9:
Elastic moduli for Ir_3Ti alloys The elastic moduli given here are the Voight moduli and the units are in GPa, except for the Poisson ratio ν and the ratio $R_{G/B}$ which are unitless.

and 3.4). For the PtTi alloys at this composition, the $C11_b$ phase was not mechanically stable.

The elastic moduli are given in Table 4.9. The bulk modulus for each of the four phases is less than for Ir in FCC. The trend has continued that the bulk modulus is lowered when Ir is alloyed with increasing amounts of Ti. The shear modulus G is also lower compared to FCC Ir. The Ir_2Ti alloys have a shear modulus lower than the two stable Ir_3Ti alloys but higher values than the $IrTi_3$ phases. This trend also occurs for the bulk modulus and for the Young's modulus.

The Poisson ratios for the four phases lie between 0.27 and 0.35. This range has values that are larger than the two stable Ir_3Ti phases ($L1_2$ and $D0_{22}$) but smaller than the phases at 50% and 25% Ir composition. These Poisson ratios that the alloys are less resistant to shear than Ir_3Ti, but more so than IrTi and $IrTi_3$ alloys.

The Poisson ratios also show that three of the four phases are considered brittle, with ν values of less than a third. The phase that does not show this is $C11_b$. The Poisson ratio for the other three phases show that these do approach ductile as the values are close to 1/3. The Poisson ratio for $C11_b$ is also close the threshold value of 1/3 where materials are said to be ductile.

The $R_{G/B}$ ratios show that only $C37$ should be considered a brittle material, as it is the only phase with an $R_{G/B}$ ratio of greater than 0.5. The other phases have $R_{G/B}$ values of less than 0.5, indicating ductile materials. The Ir_3Ti alloys have been shown to be brittle materials, like FCC Ir, while the $IrTi_3$ alloys display ductile materials, like HCP Ti. The IrTi alloys at 50% composition also show their ductile behaviour.

The values for the Poisson ratios are close to the threshold between ductile and brittle behaviour, while the $R_{G/B}$ ratios also close to the the value that separates ductile and brittle materials. Ir in FCC is known to be a brittle material; the Poisson and $R_{G/B}$ ratios confirm this. Ti in HCP is a ductile material. The 66.7% Ir composition may be percentage when, by allowing with more Ti, the alloys will begin to show the properties of Ti.

4.7 Other Compositions

Four other structures are presented here for different percentage compositions: Ir_8Ti, Ir_4Ti, Ir_5Ti_3 and $IrTi_2$. The total DOS for Ir_8Ti, Ir_4Ti and $IrTi_2$ are shown in Figure 4.21.

Only the total DOS for $IrTi_2$ $C11_b$shows two sets of peaks separated by a dip in the DOS. The Fermi level for this phase lies within the high energy peaks, close to a minimum in the DOS. For Ir_4Ti, the Fermi level lies at a minimum, showing stability for any phases close to its Ir percentage composition.

The partial DOS (Figures 4.22 and 4.23) shows the d-states being very active in terms of the stability shown by the four phases. For Ir_8Ti, the Ti d-states form very narrow peaks above the Fermi level, with very little contribution below E_F. This shows that Ir_8Ti is not as stable as other strucures. The heats of formation also showed a small value for Ir_8Ti. The Ir d-states do have some significance in the total DOS as there is Ir contributions above E_F. This would increase the stability in comparison to other IrTi alloys of similar composition. This is similar for Ir_4Ti, where Ir d-states contribution is small (though larger than that of Ir_8Ti) showing that it also has a place among alloys of similar percentage composition.

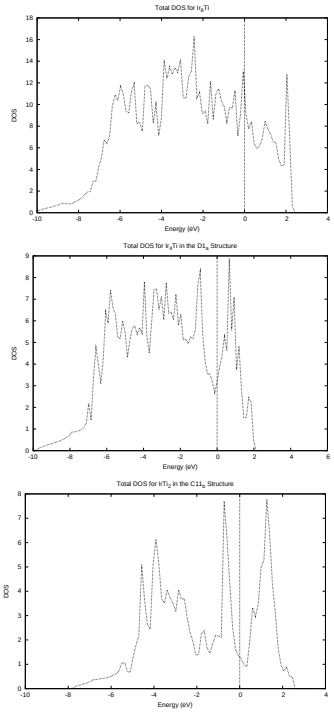

Figure 4.21:
Total DOS for different phases of IrTi, from top to bottom: Ir_8Ti, Ir_4Ti and $MoSi_2$ $C11_b$. E_F set at 0 eV.

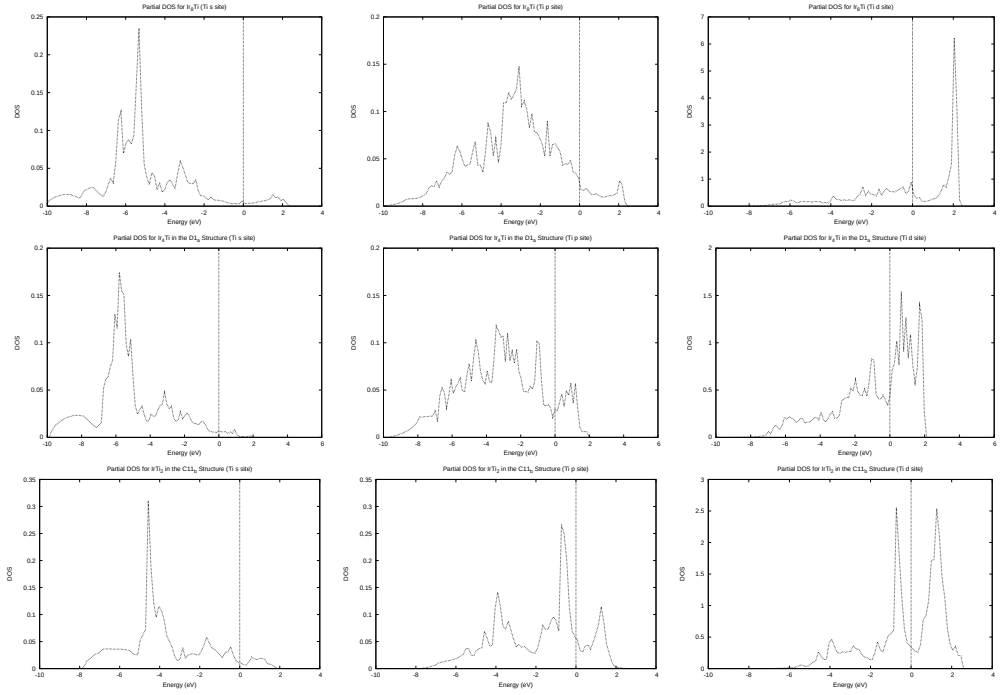

Figure 4.22:
Partial DOS (Ti site) for different phases of IrTi, from top to bottom: Ir_8Ti, Ir_4Ti and $MoSi_2$ $C11_b$. E_F is set at 0 eV.

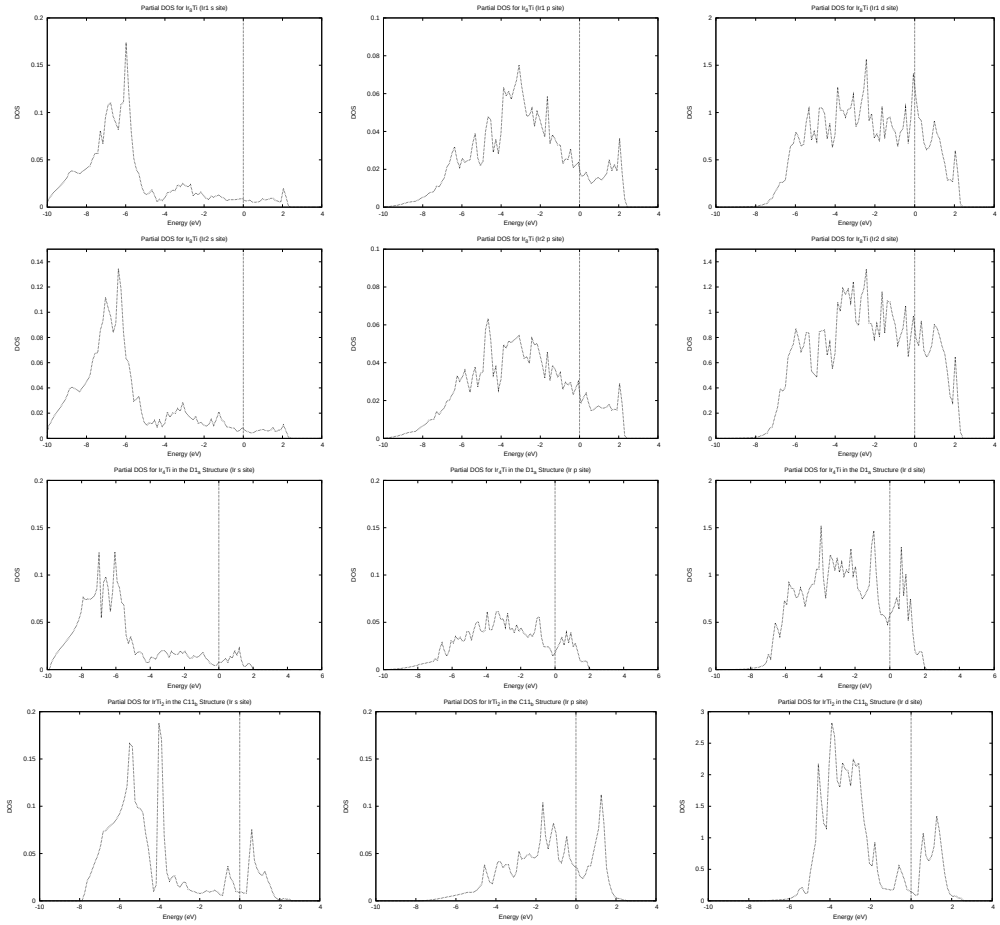

Figure 4.23:
Partial DOS (Ir site) for different phases of IrTi, from top to bottom: Ir_8Ti (the first Ir site), Ir_8Ti (the second Ir site), Ir_4Ti and $MoSi_2$ $C11_b$. E_F is at 0 eV.

The elastic moduli for Ir_8Ti, Ir_4Ti, Ir_5Ti_3 and $IrTi_2$ $C11_b$ are given in Table 4.10. The bulk modulus for Ir_8Ti is the highest of all of the IrTi alloys, though it is smaller than Ir in FCC. Similarly, its shear modulus is less than that of Ir in FCC but larger than the other IrTi alloys. This shows that alloying of Ir with Ti lowers both the bulk and the shear modulus.

Two of the four structures in Table 4.10 have $R_{G/B}$ ratios that are greater than 0.5, thereby making them brittle materials. These two are the Ir-rich Ir_8Ti and Ir_4Ti, which follow the same behaviour as FCC Ir (as well as the Ir_3Ti alloys). Since one of the Ir_2Ti alloys is brittle ($C37$) while the others indicate more ductile behaviour, and since the

	Bulk Modulus	Shear Modulus	Young's Modulus	Poisson's Ratio	
	B	G	Y	ν	$R_{G/B}$
Ir_8Ti	307.7	185.7	463.8	0.25	0.60
Ir_4Ti	292.1	172.5	432.5	0.25	0.59
Ir_5Ti_3	245.6	101.3	267.2	0.32	0.41
$IrTi_2$	175.6	86.2	222.3	0.29	0.49

Table 4.10:
Elastic moduli for IrTi alloys at different percentage concentrations. The elastic moduli given here are the Voight moduli and the units are in GPa, except for the Poisson ratio ν and the ratio $R_{G/B}$ which are unitless.

Ir_5Ti_3 structure demonstrates a ductile nature, the 66.7% to 62.5% Ir composition is the percentage where alloys of Ir with Ti start to resemble the Ti metal over the brittle FCC Ir.

The Poisson ratios for Ir_8Ti and Ir_4Ti also shows that these material resemble Ir in FCC, in that the values are low, indicating that these may be resistant to shear. The other two structures have Poisson's ratio that are larger, and hence they would not be as resistance to shear as Ir_8Ti and Ir_4Ti.

The Poisson ratios confirm the ductile nature of Ir_8Ti and Ir_4Ti, while those for Ir_5Ti_3 and $IrTi_3$ $C11_b$ show the materials tending towards ductile behaviour.

From the elastic constants for all of the different phases in the Ir-Ti system, it can be seen that the elastic moduli decrease in value with increasing percentage Ti in the alloy. Ir in FCC has the highest bulk, shear and Young's moduli compared to all of the IrTi alloys. The ordering of the alloy is

FCC Ir > Ir_8Ti > Ir_4Ti > Ir_3Ti > Ir_2Ti > Ir_5Ti_3 > IrTi > $IrTi_2$ > $IrTi_3$ > HCP Ti.

Ir-rich alloys to a certain concentration kept the same behaviour as Ir in the bulk. FCC Ir is a brittle material while Ti (in the HCP structure) is known to be ductile. Ir-alloys up 66.7% Ir composition all retained a brittle behaviour like Ir, whereas the rest of the alloys bevahed like Ti.

For FCC Ir, the Cauchy pressure is negative, indicating directional characteristic to the bonding. For Ir the bonding is not very directional due to a very small negative value for $C_{12} - C_{44}$. For other cubic materials, such as Ir_3Ti $L1_2$, this value is also negative. However, for the Ti-rich $IrTi_3$ $A15$, the Cauchy pressure is positive. This change may also have to do with an increasing amount of Ti, which causes an alloy to form metallic bonds.

Chapter 5

Conclusions

First principles density functional (DFT) calculations were carried out using the VASP code in order to study a wide of range of stoichiometries for both the Pt-Ti and Ir-Ti alloy systems. For each phase of PtTi and IrTi, the energy band structure, total density of states (DOS) and partial DOS were calculated. The elastic constants were also computed. This information was used to understand the stability of each alloy phase.

The equilibrium structure for a given percentage composition was found. Competing structures were also investigated where possible. The lattice constants equilibrium phases, as well as other phases within the Pt-Ti and Ir-Ti systems were found to be in good agreement with available experimental and theoretical work found in the literature.

The equilibrium phases for each percentage concentration was found to be the same for Pt-Ti and Ir-Ti, except in the case of 50% composition. At 50-50% composition, the equilibrium for PtTi is the $B19$ structure, which is an orthorhombic phase. For the Ir-Ti system at that percentage composition, the equilibrium phase is an orthrohombic structure that has no Pearson symbol or *Strukturebesicht* designation. This structure has a minimum energy that is very close to that of $L1_0$, the intermediate structures for IrTi. The other intermediate phase, $B19$, was concluded to be inaccessible due to an elastic constant that is negative (see Table 4.2). For PtTi, the two intermediate phases are $L1_0$ and $B33$.

The high temperature ($B2$) phase for both PtTi and IrTi, is statically unstable due to

negative elastic moduli. These observed phases can be dynamically stabilised an-harmonic phonons. This shows that the high temperature phase cannot be accessed from the $B19$ (PtTi) or the αIrTi via pressure only, but rather using increased heat. The temperature increase can renormalise the soft modes, as well as stable modes, giving rise to structures such as $B2$and possibly others such as $B1$ and $B33$.

In the 75% composition, the equilibrium phase is the $L1_2$structure. The $D0_{22}$ phase is another structure that is accessible to the system at this concentration. However, with the majority of the structures here, the transition would not be done using pressure i.e. $A15$ is another structure that is possibly accessible via heat for the Pt-Ti system but not for Ir-Ti. A large negative elastic constant leads to negative shear and Young's moduli.

Two structures were found for Pt-Ti at 25% Pt composition, namely $A15$ and $D0_{22}$. $L1_2$ has a very small C_{44} elastic constant. The difference between C_{11} and C_{12} is barely positive, leading to some elastic moduli being very small.. For $IrTi_3$, $C_{11} < C_{12}$. The elastic moduli are negative and the structure is considered not accessible for Ir-Ti at this composition.

Of the four phases considered for the 66.7% Pt/Ir composition, only $C11_b$ for Pt_2Ti was considered inaccessible due to negative elastic moduli.

The energy band structure and total DOS for all of the phases showed that both the Pt-Ti and Ir-Ti alloys are all metallic. There are no alloys that exhibit a band gap. The partial DOS showed that the DOS was dominated by Pt/Ir d-states and Ti d-states, with Pt/Ir states mostly occupied and mostly below the Fermi level. The Ti d-states form high energy peaks that lie mostly above the Fermi level. The s and p-states do not play a significant role in the bonding of the systems, apart from donating electrons to the Ti d-bands.

There were examples of significant contributions of Ti d-states below the Fermi level, as well as Pt/Ir states above the Fermi level leading to increased stability in the structure. The majority of the phases for both Pt-Ti and Ir-Ti showed good stability due to the broadening of the Pt/Ir and Ti bands, which indicates stronger participation of the

d-states in the bonding of the structure, increasing stability.

All of the Pt-Ti alloys were all found to be ductile in nature, in the same way that both Pt and Ti are ductile, Since the two constituent atoms form ductile metals in their bulk state, it is expected that alloying them together will produce metals that maintain the same nature,

Ir, on the other hand, is a brittle material in its bulk FCC form. Alloying a brittle metal with a ductile one, it was seen that Ir-rich alloys remained brittle with the majority of the constituent atoms. Ti-rich alloys were found to be ductile. The point that determines which behaviour an alloy will follow was found to be 66.7% Ir composition. Above this percentage, Ir alloys behave in the same was as FCC Ir. However, below this amount for Ir, and the alloy will behave like a ductile material.

It was also found that by alloying either Pt or Ir with Ti, the bulk modulus B would decrease with increasing amount of Ti. Ir has a very high bulk modulus for a metal, however none of the Ir-Ti alloys was found to have a bulk modulus higher than the Ir metal. Likewise for Pt, even though the bulk modulus of Pt is not large, the bulk modulus decreases from the bulk metal roughly determined by the amount of Ti in the system, until reaching Ti in the HCP structure which has the lowest bulk modulus.

For the Ir-Ti system, the trend also followed for the bulk, shear and Young's modulus. FCC Ir has the largest values, followed by Ir_8Ti, etc, decreasing as the percentage Ti in the alloy increases.

Bibliography

[1] Stan Vepřek. The search for novel, superhad materials. *J. Vac. Sci. Technol. A*, 17:2401–2420, 1999. 1, 2, 3, 4

[2] N.V. Novikov. Synthesis of superhard materials. *Journal of Materials Processing Technology*, 161:169–172, April 2005. 1, 3

[3] M. Hebbache, L. Stuparević, and D. Živković. A new superhard material: Osmium diboride OsB_2. *Solid State Communications*, 139:227–231, 2006. 1, 6

[4] M. Hebbache. The search for superhard materials: Doped boron. *EPL*, 87:16001, 2009. 1

[5] Richard B. Kaner, John J. Gilman, and Sarah H. Tolbert. Designing superhard materials. *Science*, 308:1268–1269, May 2005. 1, 2, 3, 7, 12

[6] L.S. Dubrovinsky, N.A. Dubrovinskaia, V. Swamy, J. Muscat, N.M. Harrison, R. Ahuja, B. Holm, and B. Johansson. Materials science: The hardeste known oxide. *Nature*, 410:653–654, 2001. 1, 4, 6

[7] Jean-Michel Léger and Julian Haines. The search for superhard materials. *Endeavour*, 21:121–124, 1997. 2, 3, 4, 5

[8] K.R. Rao. Elemental osmium: The latest superhard material. *Current Science*, 82:1198–1201, 2002. 2, 11

[9] M. Hebbache. Shear modulus and hardness of crystals: Density functional calculations. *Solid State Communications*, 113:427–432, 2000. 2, 13

[10] A.P. Gerk. The effect of work-hardening upon the hardness of solids: Minimum hardness. *Journal of Material Science*, 12:735–738, 1977. 2

[11] Sanwu Wang, R. Gudipati, A.S. Rao, T.J. Bostelmann, and Y.G. Shen. First-principles calculations for the elastic properties of nanostructured superhard TiN/Si_xN_y superlattices. *Applied Physics Letters*, 91:081916, 2007. 2

[12] M. Mattesini and S.F. Matar. Density-functional theory investigation of hardness, stability and electron-energy-loss spectra of carbon nitrides with $C_{11}N_4$ stoichiometry. *Phys. Rev. B*, 65:075110, 2002. 3, 61

[13] Chang-Zen Fan, Song-Yang Zen, Li-Xin Li, Zai-Ji Zhan, Ri-Ping Liu, Wen-Kui Wand, Ping Zhang, and Yu-Gui Yao. Potential superhard osmium dinitride with flourite and pyrite structure: First-principles calculations. *Phys. Rev. B*, 74:125118, 2006. 4, 9, 12, 13, 36, 47

[14] M. Keunecke, K. Yamamoto, and K. Bewilogua. Mechanical and tribological properties of cBN films on silicon and tungsten carbide substrates. *Thin Solid Films*, 398-399:142–149, 2001. 4, 13

[15] Karl E. Spear and John P. Dismukes. *Synthetic Diamond: Emerging CVD Science and Technology*. Wiley, 1994. 4, 13

[16] Jiaqian Qin, Duanwei He, Jianghua Wang, Leiming Fang, Li Lei, Yongjun Li, Juan Hu, Zili Kou, and Yan Bi. Is rhenium diboride a superhard material? *Advanced Materials*, 20:4780–4783, 2008. 4

[17] Chung-Qiang Zhuang, Xue Jiang, Ji-Jun Zhao, and Xin Jiang. Structures and elastic properties of crystalline and amorphous BC_2N solids. *J. At. Mol. Sci.*, 1:126–133, 2010. 4

[18] X. Jiang, J. Philip, W.J. Zhang, P. Hess, and S. Matsumoto. Hardness and young's modulus of high-quality cubic boron nitride films grown by chemical vapor deposition. *J. Appl. Phys.*, 93:1515–1519, 2003. 4

[19] Z. Li and R.C. Bradt. The single-crystal elastic constants of cubic (3c) SiC to 1000°C. *Journal of Materials Science*, 22:2557–2559, 1987. 4

[20] Amy Y. Liu, Renata M. Wentzcovitch, and Marvin L. Cohen. Structural and electronic properties of WC. *Phys. Rev. B.*, 38:9483–9489, November 1988. 4, 5

[21] I.R. Shein, D.V. Suetin, and A.L. Ivanovskii. Elastic properties of carbide, nitride and boride ceramics with WC-type structures. *Technical Physics Letters*, 34:841–844, 2008. 4

[22] Bijaya B. Karki, Lars Stixrude, and Jason Crain. Ab initio elasticity of three high-pressure polymorphs of silica. *Geophysical Research Letters*, 24:3269–3272, 1997. 4

[23] Jian-Zhi Zhao, Guang-Tao Wang, and Yong-Cheng Liang. Mechanical properties and electronic structures of cotunnite TiO_2. *Chin. Phys. Lett.*, 25:4356–4359, 2008. 4, 5, 6

[24] Z.Y. Chen, H.J. Xiang, Jinlong Xang, J.G. Hou, and Qingshi Zhu. Structural and electronic properties of OsB_2: A hard metallic material. *Phys. Rev. B*, 74:012102, 2006. 4, 6

[25] Xianfeng Hao, Yuanhui Xu, Zhijian Wu, Defeng Zhou, Xiaojuan Liu, and Jian Meng. Elastic anisotropy of OsB_2 and RuB_2 from first-principles study. *Journal of Alloys and Compounds*, 453:413–417, 2008. 4, 6

[26] Julong He, Licong Guo, Dongli Yu, Riping Liu, Yongjun Tian, and Hui-Tian Wang. Hardness of cubic spinel Si_3N_4. *Appl. Phys. Lett.*, 85:5571–5573, 2004. 4

[27] Cenk Kocer, Naoto Hirosaki, and Shigenobu Ogata. *Ab Initio* calculation of the ideal tensile and shear strength of cubic silicon nitride. *Phys. Rev. B*, 67:035210, 2003. 4, 7

[28] A.R. Oganov and A.O. Lyakhov. Towards the theory of hardness of materials. *Int. J. of Refractory Metals and Hard Materials*, 32(3):143–147, 2010. 3

[29] Q. Li, H. Wang, and Y.U. Ma. Predicting new superhard phases. *Int. J. of Refractory Metals and Hard Materials*, 32(3):192–204, 2010. 3

[30] V.L Solozhenko, V.V. Chernyshev, G.V. Fetisov, V.B. Rybakov, and I.A. Petrusha. Structure analysis of the cubic boron nitride crystals. *J. Phys. Chem. Solids*, 51:1011–1012, 1990. 3

[31] E. Knittle, R.B. Kaner, R. Jeanloz, and M.L. Cohen. High-pressure synthesis, characterization and equation of state of cubic C-BN solid solutions. *Phys. Rev. B*, 51:12149–12156, 1995. 4

[32] S.F. Moustafa, Z. Abbel-Hamid, Osama G. Baheig, and A. Hussein. Synthesis of WC hard materials using coated powders. *Advanced Power Technology*, pages 1–6, 2010. 4

[33] Hwan-Cheol Kim, Dong-Young Oh, and In-Jin Shon. Synthesis of WC and dense WC-$x$vol.%Co hard materials by high frequency induction heated combustion method. *International Journal of Refractory Metals and Hard Materials*, 22:41–49, 2004. 4

[34] P.T.B. Shaffer. A review of the structure of silicon carbide. *Acta Cryst.*, B25:477–488, 1969. 5

[35] Magnus Willander, Milan Friesel, Qamar-Ul Wahab, and Boris Straumal. Silicon carbide and diamond for high temperature device applications. *Journal of Material Science: Materials in Electronics*, 17:1–25, 2006. 5

[36] Shotaro Morozumi. Joining of silicon carbide. *Journal of Nuclear Materials*, 169:270–272, 1989. 5

[37] S. Ulrich, T. Theel, J. Schwan, and H. Ehrhardt. Magnetron-sputtered superhard materials. *Surface and Coating Technology*, 97:45–59, 1999. 5

[38] Chien-Min Sung and Michael Sung. Carbon nitride and other speculative superhard materials. *Materials Chemistry and Physics*, 43:1–18, 1996. 5, 7

[39] Andreas Zerr, Ralf Riedel, Toshimori Sekine, J. Edward Lowther, Wai-Yim Ching, and Isao Tanaka. Recent advances in new hard high-pressure nitrides. *Advanced Materials*, 18:2933–2948, 2006. 5, 7

[40] Serge Desgreniers and Ken Lagarec. High-density ZrO_2 and HfO_2: Crystalline structures and equations of state. *Phys. Rev. B*, 59:8467–8472, 1999. 5

[41] J.E. Lowther. Compressibility of highly coordinated metal oxynitrides: LDA calculations. *Phys. Rev. B*, 72:172105, 2005. 6

[42] J.S. Tse, D.D. Klug, K. Uehara, and Z.Q. Li. Elastic properties of potential superhard phases of RuO_2. *Phys. Rev. B*, 61:10029–10034, 2000. 6

[43] Jie Wang and Yun-Jiang Wang. Mechanical and electronic properties of 5d transition metal diborides MB_2 (M = Re, W, Os, Ru). *J. Appl. Phys.*, 105:083539, 2009. 6, 12

[44] H. Holleck. Material selection for hard coating. *J. Vac. Sci. Technol. A*, 4:2661–2669, 1986. 6

[45] J.V. Rau and A. Latini. New hard and superhard materials: $RhB_{1.1}$ and $IrB_{1.35}$. *Chemistry of Materials*, 21, April 2009. 6

[46] J.E. Lowther. Influence of nitrogen stoichiometry on properties of low-compressibility advanced nitrides. *Physica B*, 358:72–76, 2005. 7

[47] F. de Brito Mota, J.F. Justo, and A. Fazzio. Structural properties of amorphous silicon nitride. *Phys. Rev. B*, 58:8323–8328, 1998. 7

[48] W.Y. Ching, Yong-Nian Xu, and Lizhi Ouyang. Electronic and dielectric properties of insulating Zr_3N_4. *Phys. Rev. B*, 66:235106, 2002. 7

[49] Sharon Grussendorff, Nithaya Chetty, and H. Dreysse. Theoretical studies of iridium under pressure. *J. Phys.: Condens. Matter*, 15:4127–4134, 2003. 7

[50] Kuiying Chen, L.R. Zhao, and John S. Tse. *Ab Initio* study of elastic properties of Ir and Ir_3X compounds. *J. Appl. Phys.*, 93:2414–2417, March 2003. 7, 10, 13, 36, 43, 45, 46, 47, 63, 84, 98, 99

[51] Jürgen Merker, David Lupton, Michael Töpfer, and Harald Knake. High temperature mechanical properties of the platinum group metals. *Platinum Metals Rev.*, 45:74–82, 2001. 7, 13

[52] P.J. Meschter and W.L. Worrell. An investigation of high-temperature thermodynamic properties in the Pt-Ti system. *Metallurgical Transactions A*, 7:299–305, February 1976. 7

[53] M. Wenderoth, R. Völkl, T. Yokokawa, Y. Yamabe-Mitarai, and H. Harada. High temperature strength of Pt-base superalloys with different γ' volume fractions. *Scripta Materiala*, 54:275–279, 2006. 7

[54] Rainer Völkl, Dietmar Freund, Andreas Behrends, and Bernd Fischer. Platinum base alloys for high temperature space applications. In P.J. Winkler, editor, *Materials for Transportation Technology*. Wiley-VCH, 1999. 8

[55] P.J. Hill, T. Biggs, P. Ellis, J. Hohls, S. Taylor, and I.M. Wolff. An assesment of ternary precipitaion-strengthened Pt alloys for ultra-high temperature applications. *Materials Science and Engineering*, A301:167–179, 2001. 8

[56] F. Mücklich, N. Ilić, and K. Woll. RuAl and its alloys, Part II: Mechanical properties, environmental resistance and applications. *Intermetallics*, 16:593–608, 2008. 8

[57] G.N. Derry and P.N. Ross. Valence and core state modifications in Pt_3Ti. *Solid State Communications*, 52:151–154, 1984. 8

[58] H. Okamoto. Pt-Ti (platinum-titanium). *Journal of Phase Equilibri and Diffusion*, 30:217–218, 2009. 8, 10, 51, 78, 84

[59] R.E. Watson, J.W. Davenport, and Weinert M. Linear augmented slater-type orbital study of Pt-5*d*-transition-metal alloying. *Phys. Rev. B*, 36:6396–6410, 1997. 8, 11, 54, 72

[60] G.W. Fernando, R.E. Watson, and M. Weinert. Heats of formation of transition metal alloys: Full-potential and the PtTi system. *Phys. Rev. B*, 45:8233–8238, April 1992. 8, 9, 10, 51, 53, 54, 55

[61] Xiangyang Huang, Karin M. Rabe, and Graeme J. Ackland. First-principles study of the structural energetics of PdTi and PtTi. *Phys. Rev. B*, 67:024101, 2003. 8, 51, 52, 55, 56, 62

[62] C. Wolverton, G. Ceder, D. de Fontaine, and H. Dreyssé. *Ab Initio* determination of structural stability in fcc-based transition-metal alloys. *Phys. Rev. B*, 48:726–747, 1993. 8, 11

[63] W. Chen, E. Chulkov, and J. Paul. Band structure calculations of Pt and Pt_3Ti. *Physica Scripta.*, 54:392–396, 1996. 8, 9, 64, 66, 67

[64] Y.Y. Ye, C.T. Chan, and K.M. Ho. Structural and electronic properties of the martensitic alloys TiNi, TiPd and TiPt. *Phys. Rev. B*, 56:3678–3689, 1997. 8, 9, 51, 52, 54, 55, 56, 97

[65] O.K. Anderson. Linear methods in band theory. *Phys. Rev. B*, 12:3060–3083, 1975. 8

[66] A.R. Denton and N.W. Ashcroft. Vegard's law. *Phys. Rev. A*, 43:3161–3164, 1991. 8

[67] R. Yu and X.F. Zhang. Platinum nitride with flourite structure. *Applied Physics Letters*, 86:121913, March 2005. 9

[68] E. Menéndez-Proupin and Anil K. Singh. *Ab Initio* calculations of elastic properties of compressed Pt. *Phys. Rev. B*, 76:054117, 2007. 9

[69] Michael J. Mehl and Dimitrios Papaconstantopoulos. Applications of a tight-binding total-energy method for transition and noble metals: Elastic constants, vacancies and surfaces of monatomic metals. *Phys. Rev. B*, 54:4519–4530, 1996. 9, 11, 12, 13, 36, 47, 49, 52

[70] Joanne L. Murray. The Ir-Ti (iridium-titanium) system. *Journal of Phase Equilibria*, 3:205–211, 1982. 10, 12

[71] S. Curtarolo D. Morgan and G. Ceder. Accuracy of *ab initio* methods in predicting the crystal structures of metals: Review of 80 binary alloys. *Calphad*, 29:163–211, 2005. 10, 51, 73

[72] V. Raghavan. Al-Pt-Ti (aluminium-platinum-titanium). *Journal of Phase Equilibria and Diffusion*, 26:188–189, 2005. 10

[73] D. Schryvers and S. Amelinckx. New phases in the platinum-titanium and their formation mechanism studied by electron diffraction and high resolution electron microscopy. *Acta Metall.*, 34:1245–1255, 1986. 11, 64, 66, 78, 96

[74] Donald C. Harris and Louis J. Cabri. Nomeclature of platinum-group-element alloys: Review and revision. *Canadian Mineralogist*, 29:231–237, 1991. 11

[75] L.B. Hunt. A history of iridium. *Platinum Metals Rev.*, 31:32–41, 1987. 11, 13

[76] E.K. Ohriner. Processing of iridium and iridium alloys. *Platinum Metals Rev.*, 52:186–197, 2008. 11

[77] H. Okamoto. Ir-Ti (iridium-titanium). *Journal of Phase Equilibria*, 13:329, 1992. 11

[78] Hyunchae Cynn, John E. Klepeis, Choong-Shik Yoo, and David A. Young. Osmium has the lowest experimentally determined compressibility. *Phys. Rev. Lett.*, 88:135701, 2002. 11

[79] P.B. Mirkarimi, K.F. McCarty, and D.L. Medlin. Review of advances in cubic boron nitride film synthesis. *Mater. Sci. Eng. R*, 21:47–100, 1997. 12

[80] M. Weller and H. Ledbetter. Temperature-dependent young's modulus of an SiC_w/Al_2O_3 composite. *Journal of Materials Science*, 30:834–836, 1995. 12

[81] T. Górecki. The relations between the shear modulus, the young's modulus and the bulk modulus for polycrystalline metallic elements. *Material Science and Engineering*, 43:225–230, 1980. 13

[82] M.C. Payne, M.P. Teter, C.D. Allen, T.A. Arias, and J.D. Joannopoulos. Iterative minimization techniques for *ab initio* total-energy calculations: Molecular dynamics and conjugate gradients. *Rev. Mod. Phys.*, 64:1045–1097, 1992. 14, 22, 24

[83] N.W. Aschroft and N.D. Mermin. *Solid State Physics*. WB Saunders, 1976. 14, 41

[84] J.C. Slater. The theory of complex spectra. *Phys. Rev.*, 34:1293–129, 1929. 15

[85] P. Hohenberg and W. Kohn. Inhomogeneous electron gas. *Phys. Rev.*, 136:B864–B871, 1964. 16, 17

[86] R.M. Martin. *Electronic Structure: Basic Theory and Practical Methods*. Cambridge University Press, 2004. 17, 18, 20, 21, 22, 23, 26, 27

[87] P. Hohenberg and W. Kohn. Self-consistent equations including exchange and correlation effects. *Phys. Rev.*, 140:A1133–A1138, 1965. 17

[88] D.M. Ceperley and B. Alder. Ground state of the electron gas by a stochastic method. *Phys. Rev. Lett.*, 45:566–569, 1980. 20

[89] Stewart Clark. *Complex Structures in Tetrahedrally Bonded Semiconductors*. PhD thesis, University of Edinburgh, 1994. 20

[90] D.C. Langreth and J.P. Perdew. Theory of nonuniform electronic systems: I. analysis of the gradient approximation and a generalization that works. *Phys. Rev. B*, 21:5469–5493, 1980. 20

[91] A.D. Becke. Density-functional exchange-energy approximation with correct asymptotic behaviour. *Phys. Rev. A*, 38:3098–3100, 1988. 20

[92] J.P. Perdew and Y. Wang. Accurate and simple analytic representation of the electron gas correlation energy. *Phys. Rev. B*, 45:13244–13249, 1992. 20

[93] J.P. Perdew, K. Burke, and M. Ernzerhof. Generalized gradient approximation made simple. *Phys. Rev. Lett.*, 77:3865–3868, 1996. 20

[94] J.C. Slater and G.F. Koster. Simplified lcao method for the periodic potential problem. *Phys. Rev.*, 94:1498–1524, 1954. 20

[95] Klaus Koepernik and Helmut Eschrig. Full-potential nonorthogonal local-orbit minimum-basis band structure scheme. *Phys. Rev. B*, 59:1743–1757, 1999. 20

[96] José M. Soler, Emilio Artacho, Julian D. Gale, Alberto García, Javier Junquera, Pablo Ordejón, and Daniel Sánchez-Portal. The SIESTA method for *ab initio* order-N materials simulation. *J. Phys.: Condens. Matter*, 14:2745–2779, 2002. 20

[97] J.C. Slater. Wave functions in a periodic potential. *Phys. Rev.*, 51:846–851, 1937. 21, 26

[98] Korringa J. On the calculation of the energy of a bloch wave in a metal. *Physica*, 13:392, 1947. 21

[99] W. Kohn and N. Rostocker. Solution of the schrodinger equation in periodic lattices with an application to metallic lithium. *Phys. Rev.*, 94:1111, 1954. 21

[100] Jorge Kohanoff. *Electronic Structure Calculations for Solids and Molecules*. Cambridge University Press, 2006. 21

[101] O.K. Andersen. Linear methods in band theory. *Phys. Rev. B*, 12:3060–3083, 1975. 21

[102] S. Cottenier. Density functional theory and the family of (L)APW-methods: A step-by-step introduction. ISBN 90-807215-1-4, 2002. To be found at http://www.wien2k.at/reg-user/textbooks. 21

[103] H. Skriver. *The LMTO Method*. Springer, New York, 1984. 21

[104] R. Car and M. Parrinello. Unified approach for molecular dynamics and density functional theory. *Phys. Rev. Lett.*, 55:2471–2474, 1985. 21

[105] C. Lanczos. An iteration method for the solution of the eigenvalue problem of linear differential and integral operators. *J. Res. Nat. Bur. Standards*, 45:255, 1950. 21

[106] E.R. Davidson. The iterative calculation of a few of the lowest eigenvalues and correspoding eigenvectors of large real-symmetric matrices. *J. Comp. Phys.*, 17:87, 1975. 21

[107] P. Pulay. Convergence acceleration of iterative sequences: The case of scf iteration. *Chem. Phys. Lett.*, 73:393–397, 1980. 21, 30

[108] Philip Peter Rushton. *Towards a Non-Local Density Functional Description of Exchange and Correlation*. PhD thesis, University of Durham, 2002. 22

[109] Paul Robert Tulip. *Dielectric and Lattice Dynamical Properties of Molecular Crystals via Density Functional Perturbation Theory: Implementation within a First Principles Code*. PhD thesis, University of Durham, 2004. 22

[110] Charles Kittel. *Introduction to Solid State Physics*. Wiley, New York, 1996. 22

[111] D.J Chadi and M.L. Cohen. Special points in the brillouin zone. *Phys. Rev. B*, 8:5747–5753, 1973. 23

[112] H.J Monkhorst and J.D. Pack. Special points for brillouin zone integrations. *J. Phys. B*, 13:5188–5192, 1976. 23

[113] H. Hellmann. A new approximation method in the problem of many electrons. *J. Chem. Phys.*, 3:61, 1935. 24

[114] J.C. Phillips. Energy-band interpolation scheme based on a pseudopotential. *Phys. Rev.*, 112:685–695, 1958. 24

[115] M.T. Yin and M.L. Cohen. The theory of *ab initio* pseudopotential calculations. *Phys. Rev. B*, 25:7403–7412, 1982. 24

[116] L. Kleinman and D.M. Bylander. Efficacious form for model pseudopotentials. *Phys. Rev. Lett.*, 48:1425–1428, 1979. 25

[117] C. Herring. A new method for calculating wave functions in crystals. *Phys. Rev.*, 57:1169–1177, 1940. 27

[118] C. Herring and A.W. Gill. The theoretical constitution of metallic beryllium. *Phys. Rev.*, 58:132–162, 1940. 27

[119] J.C. Phillips and L. Kleinman. New method for calculating wave functions in crystals and molecules. *Phys. Rev.*, 116:287–294, 1959. 27

[120] E. Antoncik. Approximate formulation of the orthogonalized plane-wave method. *J. Phys. Chem. Solids*, 10:314–320, 1959. 27

[121] D. Vanderbilt. Soft self-consistent pseudopotentials in a generalized eigenvalue formalism. *Phys. Rev. B.*, 41:7892–7895, 1990. 27, 30

[122] P.E. Blochl. Projector augmented-wave method. *Phys. Rev. B.*, 50:17953–17979, 1994. 28, 30, 33

[123] G. Kresse and D. Joubert. From ultrasoft pseudopotentials to the projector augmented-wave method. *Phys. Rev. B*, 59:1758–1775, 1999. 28, 30, 33

[124] G. Kresse and J. Furthmüller. Efficient iterative schemes for *ab initio* total-energy calculations using a plane-wave basis set. *Phys. Rev. B*, 54:11169–11186, 1996. 30, 33

[125] G. Kresse and J. Furthmüller. Efficiency of *ab-initio* total energy calculations for metals and semiconductors using a plane-wave basis set. *Comput. Mat. Sci.*, 6:15–50, 1996. 30, 33

[126] D.D. Johnson. Modified broyden's method for accelerating convergence in self-consistent calculations. *Phys. Rev. B*, 38:12087–12813, 1988. 30

[127] P. Blaha, K. Schwarz, G.K.H. Madsen, D. Kvasnicka, and J. Luitz. An augmented plane wave plus local orbitals program for calculating crystal properties. ISBN 3-9501031-1-2, 2001. 30

[128] Jürgen Hafner. *Ab Initio* simulations of materials using VASP: Density-functional theory and beyond. *Journal of Computational Chemistry*, 29:2044–2078, 2008. 30

[129] G. Kresse and J. Furthmüller. VASP the guide, 2005. This document can be retrieved from http://cms.mpi.univie.ac.at/VASP. 30, 32

[130] M.P. Teter, M.C. Payne, and D.C. Allan. Solution of schrodinger's equation for large systems. *Phys. Rev. B*, 40:12255–12263, 1989. 31

[131] D.M Bylander, L. Kleinman, and S. Lee. Self-consistent calculations of the energy bands and bonding properties of B_12C_3. *Phys. Rev. B*, 1394-1403 42. 31

[132] H.F. Diercksen and S. Wilson, editors. *Methods in Computational Molecular Physics*, pages 95–113. D. Riedel Publishing, 1983. 31

[133] Torbjörn Björkman and Oscar Gråsäs. Adaptive smearing for brillouin zone integration. *International Journal of Quantum Chemistry*, 111:1025–1030, 2010. 32

[134] O. Jepson and O.K. Andersen. The electronic structure of H.C.P. ytterbium. *Solid State Communications*, 88:871–875, 1993. 32

[135] P.E. Blöchl, O. Jepson, and O.K. Andersen. Improved tetrahedron method for brillouin-zone integrations. *Phys. Rev. B*, 49:16223–16233, 1994. 32

[136] N.D. Mermin. Thermal properties of the inhomogeneous electron gas. *Phys. Rev.*, 137:A1441–A1443, 1965. 32

[137] K.-M. Ho, C.L. Fu, B.N. Harmon, W. Weber, and D.R. Hamann. Vibrational frequencies and structural properties of transition metals via total-energy calculations. *Phys. Rev. Lett.*, 49:673–676, 1982. 32

[138] M. Methfessel and A.T. Paxton. High-precision sampling for brillouin-zone integration in metals. *Phys. Rev. B*, 40:3616–3621, 1989. 32

[139] J. P. Perdew and A. Zunger. Self-interaction correction to density-functional approximations for many-electron systems. *Phys. Rev. B*, 23:5048–5079, 1981. 32

[140] J.P. Perdew, J.A. Chevary, S.H. Vosko, K.A. Jackson, M.R. Pederson, D.J. Singh, and C. Fiolhais. Atoms, molecules, solids, and surfaces: Applications of the generalized gradient approximation for exchange and correlation. *Phys. Rev. B*, 46:6671–6687, 1992. 32

[141] J.P. Perdew, J.A. Chevary, S.H. Vosko, K.A. Jackson, M.R. Pederson, D.J. Singh, and C. Fiolhais. Erratum: Atoms, molecules, solids, and surfaces: Applications of the generalized gradient approximation for exchange and correlation. *Phys. Rev. B*, 48:4978, 1993. 32

[142] John P. Perdew, Stefan Kurth, and Aleš Zupan Peter Blaha. Accurate density functional with correct formal properties: A step beyond the generalized gradient approximation. *Phys. Rev. Lett.*, 82:2544–2547, 1999. 33

[143] John P. Perdew, Stefan Kurth, and Aleš Zupan Peter Blaha. Erratum: Accurate density functional with correct formal properties: A step beyond the generalized gradient approximation. *Phys. Rev. Lett.*, 82:5179, 1999. 33

[144] Axel D. Becke. Density-functional thermochemistry. iii. the role of exact exchange. *J. Chem. Phys.*, 98:5648–5652, 1993. 33

[145] P.J. Stevens, F.J. Devlin, C.F. Chablowski, and M.J. Frisch. Ab initio calculation of vibrational absorption and circular dichroism spectra using density functional force fields. *J. Phys. Chem.*, 98:11623–11627, 1994. 33

[146] J. P. Perdew, K. Burke, and M. Ernzerhof. Generalized gradient approximation made simple. *Phys. Rev. Lett.*, 77:3865–3868, 1996. 33

[147] J. P. Perdew, K. Burke, and M. Ernzerhof. Erratum: Generalized gradient approximation made simple. *Phys. Rev. Lett.*, 78:1396, 1997. 33

[148] J. Heyd, G.E. Scuseria, and M. Ernzerhof. Hybrid functionals based on a screened coulomb potential. *J. Chem. Phys.*, 118:8207–8215, 2003. 33

[149] J. Heyd, G.E. Scuseria, and M. Ernzerhof. Hybrid functionals based on a screened coulomb potential. *J. Chem. Phys.*, 124:219906, 2006. 33

[150] Jürgen Hafner. Materials simulations using VASP - a quantum perspective to materials science. *Computer Physics Communications*, 177:6–13, 2007. 33

[151] G. Kresse and J. Hafner. *Ab Initio* molecular dynamics for liquid metals. *Phys. Rev. B*, 47:558–561, 1993. 33

[152] G. Kresse and J. Hafner. *Ab Initio* molecular-dynamics simulation of the liquid-metal-amorphous-semiconductor transition in germaniu4m. *Phys. Rev. B*, 49:14251–14269, 1994. 33

[153] Francis Birch. Finite strain isotherm and velocities for single-crystal and polycrystalline NaCl at high pressures and 300k. *J. Geophys. Res.*, 83:1257–1268, 1978. 34, 35

[154] M.J. Mehl, B.M. Klein, and D.A. Papaconstantopoulos. *First Principles Calculations of Elastic Properties of Metals.* John Wiley, 1993. 35, 36, 38, 39, 42, 44, 45, 61, 97

[155] C.Z. Fan, L.L. Sun, Y.X. Wang, R.P.Liu, S.Y. Zeng, and W.K. Wang. First-principles study on the structural, elastic and electronic properties of platinum carbide. *Physica B: Condensed Matter*, 381:147–178, 2006. 36

[156] R.M. Wood. The lattice constants of high purity alpha titanium. *Proceedings of the Physical Society*, 80:783, 1962. 36

[157] J.E. Lowther. Theoretical study of potential high-pressure phases of TaON and a quartenary $ZrTaO_3N$. *Phys. Rev. B*, 73:134110, 2006. 42, 45, 46, 82

[158] P. Pietrokowsky. Novel ordered phase, Pt_8Ti. *Nature*, 206:291, 1965. 51, 52

[159] Andreas Ehrlich, Uwe Weiß, Walter Hoyer, and Thomas Geßner. Microstructural changes of Pt/Ti bilayer during annealing in different atmospheres - an XRD. *Thin Solid Films*, 300:122–130, 1997. 52

[160] P. Duwez and C.B. Jordan. The crystal structure of Ti_3Au and Ti_3Pt. *Acta. Cryst.*, 5:213–214, 1952. 52, 68

[161] Kaushik Bhattacharya, Sergio Conti, Giovanni Zanzotto, and Johannes Zimmer. Crystal symmetry and the reversibility of martensitic transformations. *Nature*, 428:55–59, 2004. 53

[162] T. Biggs, M.B. Cortie, M.J. Witcomb, and L.A. Cornish. Platinum alloys for shape memory applications. *Platinum Metals Rev.*, 47:142–156, 2003. 53

[163] S. Ramakrishnan and G. Chandra. Relativistic studies on low-T_c $A15$ compounds. *Phys. Rev. B*, 38:9245–9247, 1988. 84

[164] K. Schubert, H.G. Meissner, A. Raman, and W. Rossteutscher. Einige strukturdaten metallischer phasen (ix). *Naturwissenschaften*, 12:287–287, 1964. 84

[165] A.E. Dwight and P.A. Beck. Occurence CsCl-type phases and of related distorted structures in alloys of transition metals. *Transactions of the Metallurigical Society of Aime*, 245:389–390, 1969. 84

[166] B. Chen and H.F.Franzen. Phase transition in Ir Ti+x. *Journal of the Less Common Metals*, 158:L11–L16, 1990. 86, 87